A BRILLOUIN SPECTROSCOPIC STUDY OF THE I-II PHASE TRANSITION IN CH_4

ROBIN KELLY

A Brillouin Spectroscopic Study of the I-II Phase Transition in CH_4

BY

ROBIN KELLY, B. SC. (HONS).

A THESIS SUBMITTED TO THE SCHOOL OF GRADUATE STUDIES IN PARTIAL FULFILMENT OF THE REQUIREMENTS FOR THE DEGREE OF MASTER OF SCIENCE

DEPARTMENT OF PHYSICS

MEMORIAL UNIVERSITY OF NEWFOUNDLAND

DECEMBER, 1992

ST. JOHN'S NEWFOUNDLAND

ISBN 0-315-86619-5

Abstract

The effects of rotation-translation (RT) coupling in solid methane (CH_4), especially near the I-II phase transition, have been investigated using the technique of high resolution Brillouin spectroscopy. Large single crystals of methane were grown in a liquid helium cryostat and were successfully cooled down to 15.5 K using a novel cooling technique. Laue X-ray diffraction photographs were taken to determine crystal quality and the orientation of the crystal axes. Radiation from an argon laser was incident along the axis of the cell, while the scattered radiation was analyzed at 90° by a Brillouin spectrometer.

The temperature dependence of the adiabatic elastic constants, the elasto optic coefficients, the bulk moduli and shear moduli have been determined in the temperature range 15.5 K < T < 90.4 K. The elastic constants all show acoustic anomalies at the transition temperature of 20.4 K. A theoretical analysis has shown that these anomalies are consistent with a decrease in RT coupling from the high temperature phase I to the low temperature phase II. Through an analysis of acoustic velocities in high symmetry directions, CH_4 -II has shown a strong similarity to the rare gas solids, especially argon at low temperatures.

Acknowledgements

First and foremost, I would like to express my thanks and lasting gratitude to my supervisors Dr. H. Kiefte and Dr. M. J. Clouter for their support, guidance, and above all their "patience" throughout this project. The past three years have not only been educational but they have also been a lot of fun. I would further like to thank Dr. Kiefte for the several reviewings of this thesis.

The initial stage of this investigation was a collaborative effort between myself and my good friend Vahid Askarpour. I will always be grateful for the time he spent teaching me the many experimental techniques used throughout this investigation.

I would also like to thank Mr. R. Bradley for making several photographic prints, Mr. R. Guest for his drafting of several figures, Mr. M. Ryan and Mr. W. Kieley for their work in the machine shop, and to Mr. W. Holly for taking the time to ensure I had an ample supply of cryogenic liquid. I would also like to thank the Physics department secretaries Mrs. J. Simmons, Miss E. Crocker and Mrs. B. Burke, and also the department administrator Mrs. J. Barron for the many tasks they have performed for me over the past three years. My thanks also go out to my good friends Rick Goulding, Todd Andrews, Chandran Haridas, Bogdan Mroz, and Orlando Vazquez for their many helpful discussions.

Finally, I would like to express my everlasting gratitude to my parents Robina and Leonard Kelly for their constant encouragement and support. This thesis is dedicated to them.

Table of Contents

Page

Abstract ii

Acknowledgements iii

Table of Contents iv

List of Tables vii

List of Figures x

Chapter 1 Introduction ***1***

1.1 ORDER DISORDER PHASE TRANSITIONS IN MOLECULAR CRYSTALS 1

Order Parameters 3

Acoustic Studies Near Phase Transitions 5

1.2 METHANE: A LITERATURE REVIEW 8

Chapter 2 Theoretical Background ***15***

2.1 THEORY OF ELASTICITY IN CUBIC CRYSTALS 15

2.2 ELASTIC WAVES IN CUBIC CRYSTALS 18

2.3 BRILLOUIN SCATTERING IN CUBIC CRYSTALS 19

page

2.4 Dynamical Theory of Rotation-Translation Coupling in Solid Methane 24

Chapter 3 Experimental Setup **35**

3.1 Optical Configuration 35

The Fabry-Perot Interferometer 38

The Data Acquisition System (DAS-I) 40

3.2 The Liquid Helium Cryostat 40

The Cell Assembly 44

3.3 Temperature Control and Diode Calibrations 46

GaAs and Silicon Diode Calibrations 46

Chapter 4 Experimental Procedures and Data Analysis **49**

4.1 Crystal Growth and Cooling 49

Cooling Procedure 51

4.2 Crystal Orientation Procedure 53

4.3 Optical Alignment 59

4.4 Brillouin Spectra Analysis 60

4.5 Determination of Elastic Constants and Pockel's Coefficients 62

Chapter 5 Experimental Results and Discussion **64**

5.1 Results for CH_4-I and CH_4-II 64

5.2 RT Coupling and the O-D Phase Transition in CH_4 79

Experimental Comparisons 82

page

5.3 METHANE, AND THE RARE GAS SOLIDS 87

5.4 CONCLUDING REMARKS 89

Bibliography ***90***

List of Tables

		Page
Table 1.1:	Phase transition temperatures for methane and its deuterated isotopes.	9
Table 2.1:	Elastic constant data for the rare gas solids (see Wonneberger et al.[49] and references therein), methane and heavy methane[63].	25
Table 2.2:	Table of high symmetry phonon data. Given are the directions, polarizations and mode stiffness.	34
Table 5.1:	Brillouin scattering data for CH_4-I at 72.8 K.	66
Table 5.2:	Brillouin scattering data for CH_4-I at 50.9 K.	67
Table 5.3:	Brillouin scattering data for CH_4-I at 38.5 K.	68
Table 5.4:	Brillouin scattering data for CH_4-I at 30.0 K.	68
Table 5.5:	Brillouin scattering data for CH_4-I at 25.0 K.	69
Table 5.6:	Brillouin scattering data for CH_4-I at 23.0 K.	69

Page

Table 5.7: Brillouin scattering data for CH_4-I at 21.5 K. 70

Table 5.8: Brillouin scattering data for CH_4-I at 20.5 K. 70

Table 5.9: Brillouin scattering data for CH_4-II at 19.5 K. 71

Table 5.10: Brillouin scattering data for CH_4-II at 17.5 K. 71

Table 5.11: Brillouin scattering data for CH_4-II at 15.5 K. 71

Table 5.12: Temperature dependent elastic constant data for single crystals of CH_4-I and CH_4-II. 73

Table 5.13: Temperature dependence of the Pockel's coefficients for CH_4-I and CH_4-II single crystals. 74

Table 5.14: Comparison of the theoretical (using coupled and uncoupled potentials) and the experimental elastic constants near the triple point. 79

82

Table 5.15: Temperature dependence of the ratios of acoustic velocities in high symmetry directions for CH_4-I and CH_4-II.

Table 5.16: Comparison of various experimental and theoretical values of the elastic constants in methane. 83

Page

Table 5.17: Elastic data for CH_4, CD_4, and the rare gas solids. The theoretical values for low temperature argon are derived from a Lennard-Jones potential[133][134]. 88

List of Figures

		Page
Figure 1.1:	Phase diagram of CH_4 in the temperature region 0 K < T < 90 K.	10
Figure 1.2:	Structure of CH_4-II showing the octahedral symmetry (space group Fm3c) with a disordered molecule at the symmetry centre. The ordered molecules have different orientations each with site symmetry $\bar{4}2m$.	12
Figure 2.1:	Schematic diagram of the Brillouin scattering geometry.	22
Figure 3.1:	Schematic diagram of the optical apparatus.	37
Figure 3.2:	Diagram of the liquid helium cryostat (not to scale).	42
Figure 3.3:	Schematic diagram of the cell assembly (not to scale).	45
Figure 3.4:	Temperature calibration curve of the silicon diode in the region 10 K < T < 90.6 K.	48

Figure 4.1. Diagram showing the Euler angles (θ,ϕ,χ) used to transform from the laboratory reference frame to the crystal reference frame. The vectors $\vec{k}$, $\vec{k}_0$, and $\vec{q}$ which define the scattering geometry are also shown.[11] 54

Figure 4.2: Schematic diagram of the X-ray diffraction geometry. (x,y,z) is the laboratory coordinate frame. The X-rays were incident along the y-axis, R is the reflecting plane with normal $\hat{n}$, P is the Laue spot with coordinates (x',z'), and 2θ is the angle of diffraction. 55

Figure 4.3: Sample Laue diffraction photograph of crystal #7. Below the photo is a schematic diagram of the Laue spots showing the Miller indices of the Bragg planes causing the interference. The best fit Euler angles are also given. 58

Figure 4.4: Stick diagram of a typical CH_4 spectrum showing the various frequency shifts. The R_i are the central Rayleigh components, the L_i, T_i^s, and T_i^f are the longitudinal, slow transverse, and fast transverse components, respectively. The SFR_i are the free spectral ranges, the ΔL_i, ΔT_i^s, and ΔT_i^f are the frequency shifts of the L_i, T_i^s, and T_i^f components. 61

Figure 5.1: Brillouin spectrum of crystal #7 recorded at T = 17.5 K. Only two components are visible, the longitudinal L and the slow transverse T belonging to the central Rayleigh component R. 65

Figure 5.2: Temperature dependence of the elastic constant C_{11} in CH_4 single crystals. 75

Figure 5.3: Temperature dependence of the elastic constant C_{12} for CH_4 single crystals. 75

Figure 5.4: Temperature dependence of the elastic constant C_{44} for CH_4 single crystals. 76

Figure 5.5: Magnification of C_{11} near the O-D phase transition in CH_4. 76

Figure 5.6: Magnification of C_{12} near the O-D phase transition in CH_4. 77

Figure 5.7: Magnification of C_{44} near the O-D phase transition in CH_4. 77

Figure 5.8: Temperature dependence of the elastic moduli for single crystals of CH_4. The triple point data at 90.4 K were compiled by Rand et al.[63]. 78

Page

Figure 5.9: Comparison of the temperature dependence of the elastic moduli of solid CH_4 using both single and polycrystal data. 85

Figure 5.10: Comparison of the temperature dependence of the elastic moduli of solid CD_4 using both single and polycrystal data. 86

Chapter 1:

Introduction

1.1 Order-Disorder Phase Transitions In Molecular Crystals.

The main emphasis of this thesis is a study of the order-disorder (O-D) phase transition in CH_4 using the technique of high resolution Brillouin Spectroscopy. This transition (at 20.4 K) from the high temperature phase I to the low temperature phase II has been of much interest and confusion in the past, even with respect to its order. A very brief review of O-D phase transitions in molecular solids will now be given .

Every crystalline solid is characterized by a periodic, three dimensional array of atoms in a lattice. The atoms (or molecules) are, however, not generally fixed in position or orientation with respect to the other atoms in the lattice. There are, consequently, two types of order associated with an O-D phase transition: (1) positional order, in which molecules are hindered in their ability to move from site to site in the lattice and (2) orientational order, where there is a decrease in the number of orientations the molecules can occupy. When discussing molecular solids, each phase of the crystal is characterised by the amount of order or disorder inherent within that phase. In the case of methane, the rotations of 6 of the 8 molecules in the unit cell are frozen out in CH_4-II, while all 8 molecules have rotational freedom in CH_4-I. The I-II phase transition in

methane is an example of a pure order-disorder transition in which the fcc lattice configuration remains the same in both phase I and phase II. In other transitions the increase in order is usually also accompanied by a structural change (an example being the phase II - phase III tetragonal distortion in CD_4). A typical O-D transition then can be purely orientational, positional, or a mixture of both.

Most phase transitions, regardless of form, are classified on the basis of their thermodynamic properties and changes during the transition [1]. In a typical O-D transition the Gibbs free energy (G) varies continuously, whereas many other thermodynamic properties such as entropy (S), volume (V), and heat capacity (C_P), undergo discontinuous changes during the transition. The phase transition is classified according to how these quantities are related to the derivatives of the free energy. With the free energy given by $G = H - TS$ (H being the enthalpy), and $dG = VdP - SdT$, the following relationships exist between the first and second derivatives

$$\left(\frac{\partial G}{\partial P}\right)_T = V \quad , \quad \left(\frac{\partial G}{\partial T}\right)_P = -S$$

$$\left(\frac{\partial^2 G}{\partial P^2}\right)_T = \left(\frac{\partial V}{\partial P}\right)_T = -V\beta \quad , \quad \left(\frac{\partial^2 G}{\partial P \partial T}\right) = \left(\frac{\partial V}{\partial T}\right)_P = V\alpha \qquad (1.1)$$

$$\left(\frac{\partial^2 G}{\partial T^2}\right)_P = -\frac{C_P}{T} \quad .$$

Here C_P, α, and β, are the heat capacity, volume thermal expansivity, and isothermal compressibility respectively. A transition is called first order if there is a discontinuity in the first derivative of the free energy (i.e. in volume and entropy), and second order if there is a discontinuity in the second derivatives (i.e. in heat capacity, $V\alpha$, or $V\beta$). A second order transition in which the heat capacity goes to infinity as the transition temperature is approached is given a special name, a λ - transition. Clusius [2] noticed such an anomaly in the I - II transition in CH_4.

Order Parameters

The literature on the theory of phase transitions is vast. The many different crystal symmetries and chemical compositions have greatly hindered the development of a general theory which encompasses all molecular species. However in most molecular crystals, the passage of the solid through phase transitions is accompanied by changes in symmetry. In the higher temperature phases a molecule can occupy more than one lattice site, and hence there is a non-zero probability that it can be found at any site in the lattice; this defines a disordered state. In the lower temperature phases, each molecule occupies its own site with a probability of unity, while the probability of it being at any other site is zero; this is an ordered state. The transition to molecular disorder is accomplished by the translational or rotational motion of the molecules in the lattice. Consider the case of CuZn[3] which, in the ordered phase, has a simple cubic lattice (Cu atom at the centre, Zn atoms at the corners of the conventional cell). When the solid enters the disordered phase, the molecule gains rotational freedom until both the Cu and Zn atoms can occupy any lattice site with equal probability. This increased rotation introduces a new lattice vector and transforms the symmetry of the crystal lattice to body centred cubic. On the other hand, in the high temperature cubic phase of $BaTiO_3$ (Ba atoms at the corners, O atoms at the face centres, Ti atoms at the cube centre), when the solid is cooled through the transition the titanium and oxygen move relative to the barium atoms along the edges of the cube. The result is an ordered phase of tetragonal symmetry.

In the 1930's Landau[3] introduced a quantitative analysis of the symmetry changes which accompany phase transitions. He introduced the concept of an order parameter η, which is a physical quantity that takes non-zero values (positive or negative) in the unsymmetrical ordered phase, varies continuously to zero at the transition temperature T_c and remains zero in the disordered phase. In the case of CuZn the order

parameter can be written in terms of the lattice site probabilities via

$$\eta = \frac{(W_{Cu} - W_{Zn})}{(W_{Cu} + W_{Zn})} \tag{1.2}$$

where W_{Cu} and W_{Zn} are the probabilities of finding a Cu or a Zn atom respectively, at a given lattice site. Following Landau's theory [1,3], in the region near the phase transition the free energy $G(P,T,\eta)$ is expanded in terms of the order parameter η. From this expansion, along with certain symmetry arguments, it can be shown that for a second order transition there is a discontinuity in all second derivative quantities such as specific heat, compressibility and volume expansivity. The first derivative quantities, such as entropy, remain continuous. First order transitions are described by discontinuities in entropy and volume accompanied by a continuous variation in the heat capacity.

In the discussion so far the order parameter has been a molecular displacement, either translational or rotational. The symmetry of the crystal, however, can be reduced by the ordering of other physical parameters. Ferroelectric transitions are characterized by the introduction of a spontaneous polarization $\vec{p}$, while ferroelastics are named because the transition causes an induced strain $\vec{e}$. Other transitions may cause the freezing out of specific phonon coordinates in high symmetry directions. Large density fluctuations near second order phase transitions are common and in turn produce anomalies in the dielectric constant and the index of refraction. In light scattering experiments these anomalies cause the Rayleigh intensity to increase drastically. For the specific case of Brillouin scattering, changes in the intensity of different phonon modes, the appearance or disappearance of a transverse mode, or sudden changes in the phonon frequencies may be noticed. A much more detailed discussion of possible acoustic anomalies is given below.

Acoustic Studies Near Phase Transitions

Acoustic studies of molecular crystals, either from Brillouin scattering or ultrasonic measurements, yield important information about O-D phase transitions. Acoustic measurements are used to determine the elastic properties of the crystal by measuring the elastic response function (Hooke's Law $\sigma_{ij} = \sum C_{ijkl} e_{kl}$, see chapter 2). The elastic constants, as well as phonon velocity plots, are useful and accurate tools in determining the location of the transition temperature, T_c. They can also be used to determine the phase diagrams and the order of the transition. Of great interest are the ferroelastic transitions where the strain is the order parameter; here the anomalies in the phonon acoustic modes are very pronounced and the transition is easily detected. However in a greater number of molecular crystals, including the current work on methane, the strain is not the order parameter. In a vast majority of these cases Brillouin scattering can still be used because of the strong coupling which exists between the strain and the order parameter. The resulting anomalies may not be as strong as in the ferroelastic case, but they still warrant theoretical consideration to determine the various coupling parameters.

For a second order transition, the theoretical analysis[4] of the elastic constant observations can be derived from Landau's theory where the free energy density is expanded in terms of the order parameter η:

$$G(P,T,\eta) = G_0(P,T) + \frac{1}{2}a(P,T)\eta^2 + \frac{1}{4}b(P,T)\eta^4 + \cdots \quad . \qquad (1.3)$$

Keeping only the lowest order term in $G(P,T,\eta)$, and then performing a first order expansion of $a(P,T)$ in the vicinity of T_c gives

$$a(P,T) = \alpha(P)(T - T_C) \quad . \qquad (1.4)$$

There are, however, two other contributions to the free energy. There is the strain energy

contribution $\frac{1}{2}C_0e^2$ and the coupling of the strain to the order parameter which introduces an interaction term given by

$$G_{int} = Fe\eta + He\eta^2 + \cdots + \quad . \tag{1.5}$$

The discussion here is kept simple by choosing to work with a crystal strain in one dimension. The results for the three dimensional case are the same, except for mathematical simplicity. This argument may be applied to the three dimensional case by applying the appropriate coordinate frame rotation.

For bilinear coupling between the order parameter and strain only the first term of the interaction is dominant (i.e. $G_{int} = Fe\eta$). These forces of interaction are proportional only to the strain, and since there are no other forces, implies

$$\left(\frac{\partial G}{\partial \eta}\right) = \left(\frac{\partial G}{\partial \eta}\right)_0 + \left(\frac{\partial\left(\frac{\partial G}{\partial \eta}\right)}{\partial \eta}\right)_e \delta\eta + \cdots = 0 \quad . \tag{1.6}$$

Now the combined expression for $G(P,T,\eta)$ is given by

$$G(P,T,\eta) = G_0(P,T) + \frac{1}{2}\alpha(P)(T - T_C)\eta^2 + \frac{1}{2}C_0e^2 + Fe\eta + \cdots \tag{1.7}$$

which, upon substitution into (1.6) gives

$$\frac{\partial G}{\partial \eta} = Fe + \left(\frac{\partial^2 G}{\partial \eta^2}\right)_{\eta=0} \delta\eta = 0 \quad . \tag{1.8}$$

This gives an expression for the order parameter fluctuation:

$$\delta\eta = -\chi_\eta Fe \tag{1.9}$$

where χ_η is the order parameter susceptibility defined by

$$\frac{1}{\chi_\eta} = \left(\frac{\partial^2 G}{\partial \eta^2}\right)_{\eta=0} \quad . \tag{1.10}$$

The order parameter susceptibility measures the response of the order parameter to the variations in the applied strain. Application of Hooke's Law in the ordered phase gives

$$\sigma = \frac{\partial G}{\partial e} - C_T e \quad . \tag{1.11}$$

Performing a the Taylor expansion of $\frac{\partial G}{\partial e}$ gives

$$\frac{\partial G}{\partial e} = \left(\frac{\partial G}{\partial e}\right)_{\eta=0} + \left(\frac{\partial\left(\frac{\partial G}{\partial e}\right)}{\partial \eta}\right)_{\substack{e \\ \eta=0}} \delta\eta = C_0 e + F\delta\eta \quad , \tag{1.12}$$

which, upon substitution of (1.9) gives

$$\sigma = \left(C_0 - F^2\chi_\eta\right)e \quad . \tag{1.13}$$

This expression shows that the effect of order parameter - strain coupling is to cause a reduction in the elastic constants from the disordered to the ordered phase. The relationship is given by

$$\begin{aligned} C_T &= C_0 - F^2\chi_\eta \\ &= C_0\left(\frac{T - T_C - \frac{F^2}{aC_0}}{T - T_C}\right) \quad , \end{aligned} \tag{1.14}$$

where the final expression employs equations (1.10) and (1.7).

Thus in the bilinear coupling regime, the elastic constants probe directly the order parameter susceptibility. This in turn provides some understanding of the molecular dynamics governing the transition. It is important to note, however, that the elastic coupling is very much dependent on the type of order parameter. In many cases the coupling may not be bilinear but quadratic or cubic in nature. In this instance the

elastic anomalies may not be as pronounced as in the foregoing discussion. In many cases the transition can be noticed more easily by looking at specific combinations of the elastic constants. Some specific examples include the O_h - T_d transition in NH_4Cl [5] at T=243 K, where the more pronounced anomaly occurs in $C_{11}+2C_{12}$. For the O_h - D_{4h} transition in NH_4Br [6] at T=234 K, the anomaly is given by $C_{11}-C_{12}$. In these cases the strain couples to orientation of the NH_4 tetrahedron. For the transitions in $SrTiO_3$ (O_h-D_{4h} at T=105 K) [7-10] and $BaTiO_3$ (O_h - C_{4v} at T=401 K) [11], the order parameters are the octahedral rotation and electric polarization respectively. Within this discussion, the ferroelastics comprise an important class of materials where the strain is the ordering quantity. In these cases measurements of the elastic constants help to determine the soft acoustic phonons, and hence determine the specific planes and directions in which this mode softening occurs. An example of this type is the O_h-D_{2h} transition in KCN at T=168 K. The ordering strain is $e_t = e_4, e_5, e_6$, and the corresponding elastic anomaly is seen in C_{44}. Brillouin scattering experiments can clearly be a valuable probe in studying these types of phase transitions.

1.2 Methane: A Literature Review

The study of molecular solids is a vast and ever growing subject. In recent times, however, no molecule has attracted more attention than methane, i.e. CH_4, or the deuterated compounds - CH_3D, CH_2D_2, CHD_3, and CD_4. Much of the early work with molecular crystals was done on the rare gas solids[12] because of their molecular simplicity. While CH_4 is not a rare gas solid, it does contain many of characteristics of a simple system such as a closed electron shell, tight internal bonding, weak coupling between molecules, and an almost spherically symmetric molecular structure. The rare gas most closely related to methane is argon, as may be seen through a comparison of the

quantum parameter $\Lambda = {}^{h}/_{\sigma\sqrt{m\epsilon}}$ (Λ_{Ar}=0.187 , Λ_{CH_4}=0.235 , Λ_{CD_4}=0.209)[13]. Here h is Planck's constant, σ is the molecular diameter, m is the mass, and ϵ is the depth of the intermolecular potential well. Methane also exhibits both rotational and translational modes which provide a logical extension of ideas developed using rare gas solids.

Some of the first experimental work with methane was done by Clusius[42] in the late 1920's while trying to verify the Third Law of Thermodynamics. His heat capacity measurements showed two strong λ - type anomalies in CD_4 at 27.1 K and 22.0 K, while only one occurred in CH_4 at 20.4 K. Later calorimetric work [11,16] not only confirmed this, but found two phase transitions in the other deuterated methanes under zero pressure. The phase transition temperatures of the methane isotopes are shown in Table 1.1. It should be noticed how the temperature of respective transitions increases with the amount of deuteration. From the CH_4 phase diagram in figure (1.1), it can be seen that the phase II -phase III transition exists only at pressures above 0.2 kbar[42].

The discovery of these transitions did not spark theoretical interest until 1959, when James and Keenan[17] (JK) published their famous paper on the order-disorder phase transitions in CD_4. They employed a classical mean field approach. The quantum nature of the molecular rotations was neglected and they failed to incorporate the consequences of nuclear spin conversion. The interaction was assumed to be a nearest neighbour octupole-octupole potential, the octupole being the lowest non-vanishing multipole moment for a tetrahedral charge distribution. From these assumptions they

Compound	Phase Transition Temperatures		
	III ↔ II	II ↔ I	I ↔ liquid
CH_4	none	20.4	90.67
CH_3D	16.1	23.1	90.41
CH_2D_2	19.1	24.9	90.17
CHD_3	20.9	26.0	89.96
CD_4	22.4	27.2	89.78

Table 1.1: Phase transition temperatures for methane and its deuterated isotopes.

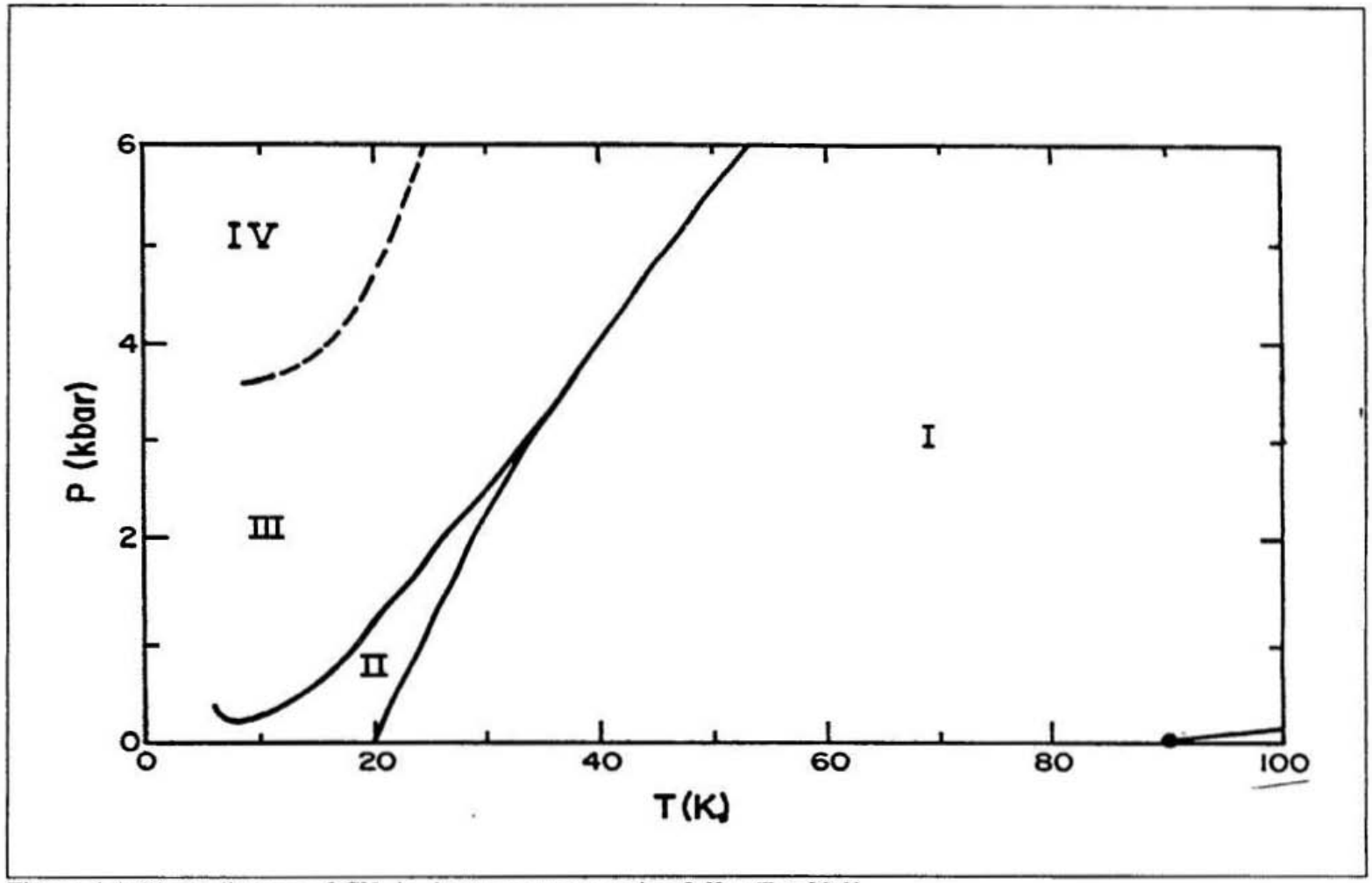

Figure 1.1: Phase diagram of CH_4 in the temperature region 0 K < T < 90 K.

concluded that CD_4 could exist in three stable phases. They found that the higher temperature Phase I consists of an fcc structure in which all the molecules are orientationally disordered. Phase II also consists of an fcc lattice with a partially ordered, eight sublattice structure, in which three of four molecules are orientationally ordered, while the other disordered molecule maintains the symmetry of phase I. Finally, phase III was found to have a tetragonal structure in which all CD_4 tetrahedra are aligned the same way. The predictions of phase I and II were later confirmed by neutron scattering[18],[19] and X-ray diffraction[20],[21] for both CH_4 and CD_4. Phase I is fcc with site symmetry m3m (O_h) and phase II is fcc with ordered sites having symmetry $\bar{4}2m$ (D_{2d}). The structure of phase III shows a slight tetragonal distortion, with a volume change of 0.54%[21]; the exact point and space groups could not be determined from these experiments. The structure of CH_4-II is shown in figure (1.2).

The JK model could only be used qualitatively in describing the statistical mechanics of CH_4. Due to its smaller moment of inertia (with respect to CD_4), the librational energies are much greater, and hence the molecular rotations must be treated quantum mechanically. This problem was undertaken by Yamamoto and his co-workers in a series of papers between 1973 and 1978.[22] They were able to obtain quantitative calculations of the crystalline field as well as the orientational part of the intermolecular interaction. This new Hamiltonian was then substituted into the analysis of James and Keenan to give the Extended James and Keenan model (EJK). Like the JK model this extended picture showed that CH_4-I and CH_4-II are isomorphic to the respective phases in CD_4. One of the most important conclusions to come from this analysis, however, is that the I - II transition must be first order. This fact was confirmed later through x-ray measurements of the volume expansion and lattice parameters.[23],[30]

The dynamics of the phase I - phase II transition in methane has attracted much experimental attention. The early infra red[24],[25],[26] and Raman[27] work were the first to predict the fcc structure of phase I and phase II. Later measurements of the IR

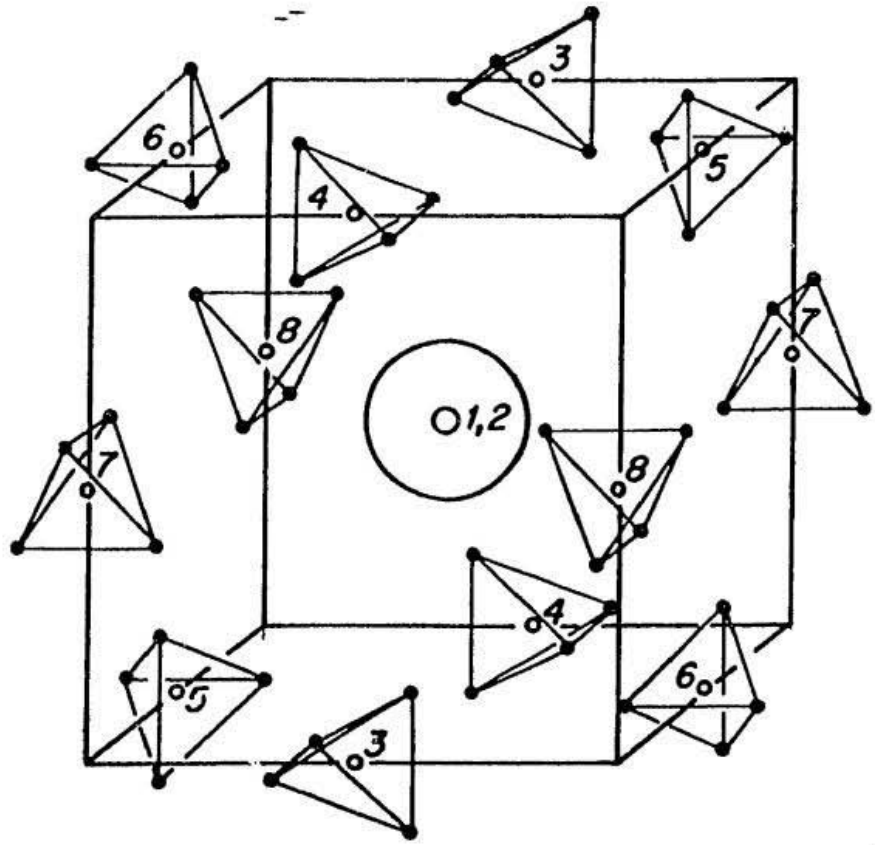

Figure 1.2: Structure of CH_4-II showing the octahedral symmetry (space group Fm3c) with a disordered molecule at the symmetry centre. The ordered molecules have different orientations each with site symmetry $\bar{4}2m$.

spectrum[28],[29] showed frequency ratios consistent with the theoretical predictions, while the overtone bands in phase II showed a full vibrational structure (containing librations and full rotations) consistent with its partially ordered structure. The anti-ferrorotational structure was also exhibited through measurements of the dielectric constant[30] and the scattering of incoherent neutrons[31], the latter of which calculated the energy levels of the freely rotating O_h molecules and the tunnelling states of the ordered T_d molecules. All three of CD_4-I, CD_4-II, and CH_4-I, showed no noticeable birefringence[32], accept that due to internal strain. CD_4-III, however, was markedly birefringent, consistent with its small

tetragonal distortion. CH_4-II did exhibit a small amount of birefringence in the temperature range 17 K - 20 K, while at lower temperatures the effect disappeared. At elevated pressures the birefringence in CH_4 resumed in phase III. X-ray diffraction[120] proved that this was consistent with the tetragonal isomorphic structures of CH_4 and CD_4 in phase III. Methane was also one of the first molecular solids to have its phase transition studied by NMR spectroscopy. These early results were obtained from samples having high O_2 impurity which reduced the relaxation time by a factor of 10^4. Later results of Nijman et al.[33] have produced the most accurate phase diagram of CH_4 to date. Their spin relaxation time measurements have noted that CH_4-III exist only at pressures above 0.2 kbar, while the existence of CH_4-IV was found at pressures above 3 kbar. The complete phase diagram of CH_4 is shown in figure (1.1).

The absence of phase III at zero pressure, is a characteristic which distinguishes CH_4 from its deuterated isotopes. It was, nevertheless, believed that an early thermal inertia measurement found at 9 K was indeed due to the II-III transition.[11] This conclusion seemed well founded when extrapolating from the II-III transition temperatures of the other deuterated species. NMR experiments on the transition temperatures CH_4 CD_4 mixtures[34],[35] have also extrapolated a CH_4 II-III transition at ~9 K. The results of x-ray diffraction and neutron scattering, however, have dismissed the existence of phase III in favour of phase II structure down to 0 K (at zero pressure). The question remains as to what caused these early entropy anomalies. It is known that CH_4 exists in three spin states, A (I=0), T (I=1), and E (I=2). In the beginning, interconversion of different spin species was dismissed as a possible explanation because the magnitude of the entropy measurements were so small. Measurements of the nuclear magnetization[36] were also smaller than the predicted values for total spin conversion. Code et al.[37] examined these differences under the assumption that total conversion does not occur. They suggested that there must be a fast conversion of the disordered molecules and a slow conversion of the ordered ones. Using this suggestion a detailed quantitative analysis was

undertaken[18].This analysis concluded that the conversion was due to a coupling of the intramolecular dipole-dipole interaction and the intermolecular octupole-octupole interaction. The theory was found to be in good agreement with both the thermodynamic and nuclear magnetization results, and has been cited as the explanation of the early calorimetric measurements. Thus CH_4 exists in only two phases, but calculation of the energy levels is made extremely difficult because of this conversion process, where interaction with phonon processes is not completely known. Much work remains if the molecular dynamics is to be completely understood.

The present thesis involves measurements of the elastic constants as a function of temperature, with particular emphasis on the I-II phase transition, in an effort to gain further insight into the molecular dynamics as related to the coupling of the rotational and translational degrees of freedom. First, some background theory will be discussed followed by the experimental methodology.

Chapter 2:

Background Theory

2.1 Theory of Elasticity in Cubic Crystals

The theory of elasticity focuses on the strain state of a solid and the applied forces (i.e. stress) causing it. For a rigorous theoretical treatment the reader can refer to several books by Musgrave [39], Nye [40], and Landau & Lifshitz [41]; only a brief resume will be given here. Let $\vec{r} = (r_1, r_2, r_3)$ denote the position vector of a point in the crystal with respect to some coordinate system, and let $\vec{r}' = (r_1', r_2', r_3')$ denote the position of the point after deformation. Since the deformation is continuous

$$\vec{r}' = \vec{r} + \vec{u} \tag{2.1}$$

where $\vec{u}$, the displacement vector, is a continuous function of r_k $(k = 1,2,3)$. By considering the change in distance between two neighbouring points $\vec{r}$ and $(\vec{r} + d\vec{r})$ before and after the deformation, it can be shown that

$$|d\vec{r}'|^2 - |d\vec{r}|^2 = 2\sum_{i=1}^{3}\sum_{j=1}^{3} e_{ij} dr_i dr_j \tag{2.2}$$

where for small deformations e_{ij} is defined by:

$$e_{ij} = \frac{1}{2}\left(\frac{\partial u_i}{\partial r_j} + \frac{\partial u_j}{\partial r_i}\right) \quad . \tag{2.3}$$

The quantity e_{ij} is called the *strain tensor*; an inspection of (2.3) quickly reveals that $e_{ij} = e_{ji}$, and hence contains only 6 independent components.

The net force acting on a small volume element dV is now considered. Assuming that the atomic forces are of zero range and that body forces can be neglected, then the only forces acting on the volume element are those which act on the surface dS. So let the net force acting on the volume element be denoted $\vec{F} = (F_1, F_2, F_3)$. Since it acts only on the surface it can be expressed as [41]:

$$F_i = \int_s \vec{\sigma}_i \cdot d\vec{a} \tag{2.4}$$

where $d\vec{a}$ is the element of surface area which is directed along the outward normal of dV, and $\vec{\sigma}_i \cdot d\vec{a}$ represents the ith component of force acting on $d\vec{a}$. Applying the divergence theorem gives:

$$F_i = \int_v \nabla \cdot \vec{\sigma}_i \, dv = \int_v \sum_{j=1}^{3} \frac{\partial \sigma_{ij}}{\partial r_j} \, dv \quad . \tag{2.5}$$

The quantity inside the integral is the force per unit volume f_i, while σ_{ij} is a three by three matrix called the *stress tensor*. The elements of the stress tensor are symmetric (i.e. $\sigma_{ij} = \sigma_{ji}$); they represent the ith component of force acting on a unit of area normal to the x_j axis. When an object is subjected to a homogeneous stress, according to Hooke's law, there exists a linear relationship between stress and the resulting strain such that

$$\sigma_{ij} = \sum_{k=1}^{3} \sum_{l=1}^{3} C_{ijkl} e_{kl} \qquad (2.6)$$

where the C_{ijkl} are called the *elastic stiffness constants*. The elastic constants form a fourth rank tensor with 81 elements. The symmetry of e_{ij} and σ_{ij} reduces the number of distinct elastic constants to 36, in which case the elastic constants can be expressed as a 6×6 matrix by relabelling our indices as follows:

TENSOR INDICES:	11	22	33	23	31	12
MATRIX INDICES:	1	2	3	4	5	6

Calculation of the strain energy shows that the matrix C_{ij} is symmetric and that the number of elastic constants reduces to 21. The point group symmetry of cubic crystals further reduces the number of distinct constants to 3, and the matrix is given by [12]:

$$\begin{pmatrix} c_{11} & c_{12} & c_{12} & 0 & 0 & 0 \\ c_{12} & c_{11} & c_{12} & 0 & 0 & 0 \\ c_{12} & c_{12} & c_{11} & 0 & 0 & 0 \\ 0 & 0 & 0 & c_{44} & 0 & 0 \\ 0 & 0 & 0 & 0 & c_{44} & 0 \\ 0 & 0 & 0 & 0 & 0 & c_{44} \end{pmatrix} \qquad (2.7)$$

Since the elastic energy must be positive, it follows that

$$C_{44} > 0 \,, \quad C_{11} > |C_{12}| \,, \quad C_{11} + 2C_{12} > 0 \,. \qquad (2.8)$$

In the case of cubic crystals the anisotropy factor A, the bulk modulus B, the shear modulus G and the Cauchy parameter δ (describing the violation of the Cauchy relation $C_{44} = C_{12}$) are given by

$$A = \frac{2C_{44}}{C_{11} - C_{12}}\ , \quad B = \frac{1}{3}(C_{11} + 2C_{12})\ , \quad \delta = \frac{(C_{44} - C_{12})}{C_{12}}$$
$$G = \frac{1}{2}\left[\frac{C_{44}}{5}\left(3 + \frac{2}{A}\right) + \frac{5C_{44}}{\left(3 + \frac{2}{A}\right)}\right] \quad . \tag{2.9}$$

2.2 *Elastic Waves in Cubic Crystals*

The propagation of elastic waves in a solid is governed by Newton's Second Law. In the case of Brillouin scattering, the elastic waves are of long wavelength and the amount of heat given off in one period is considered negligible. In this context the process is considered adiabatic and the elastic constants will be referred to as *adiabatic elastic constants*. If f_i denotes the force per unit volume along the x_i axis, then using equation (2.5), and Hooke's law (2.6) gives:

$$\sum_{j=1}^{3}\sum_{k=1}^{3}\sum_{l=1}^{3} C_{ijkl}\frac{\partial^2 u_l}{\partial r_j \partial r_k} = \rho\frac{d^2 u_i}{dt^2} \quad . \tag{2.10}$$

This is the differential wave equation and it has plane wave solutions of the form

$$u_i(\vec{r},t) = u_{i0}e^{i[(\vec{q}\cdot\vec{r}) - \omega t]} \quad . \tag{2.11}$$

Upon substitution into equation (2.10) the matrix equation

$$(\lambda_{ij} - \rho\omega^2\delta_{ij})u_{i0} = 0 \tag{2.12}$$

is obtained where, in the case of cubic crystals, λ_{ij} is given by

$$\begin{aligned} \lambda_{ij} &= (C_{12} + C_{44})q_i q_j \qquad i \neq j \\ &= (C_{11} - C_{44})q_i^2 + C_{44}q^2 \qquad i = j \end{aligned} \tag{2.13}$$

Solving the secular equation of (2.12) three eigenvalues $\rho\omega^2$ are obtained. The three distinct solutions ω_μ correspond to a longitudinal mode and two transverse (fast and slow) modes. The velocities of these acoustic waves can be determined from

$$\omega_\mu(\vec{k}) = V_\mu(\vec{k})\,|\vec{k}| \tag{2.14}$$

By measuring the Brillouin shifts the elastic constants can consequently be determined by solving equation (2.12) using the method of least squares.

2.3 *Brillouin Scattering in Cubic Crystals*

Brillouin [43] was the first to show that in a continuous medium, monochromatic light (λ_0, ν_0) can interact with thermally elastic sound waves (λ_s, ν_s) to satisfy the Bragg reflection condition $\lambda_0 = 2\,n\lambda_s \sin(\alpha/2)$ and cause scattering at an angle α. Since then, the theory of Brillouin scattering has been greatly enhanced. A rigorous treatment has been given by several authors: see Born and Huang [44], Fabelinski [45], and Nelson et al [46]. In the particular case of cubic crystals, the reader is referred to a detailed discussion by Benedek and Fritsch [47]. The main purpose here is to give the equations necessary for analysis of the experimental data; they show the relationship between the elastic constants and the Brillouin shifts, and between the elasto-optic (Pockel's) coefficients and the Brillouin intensities.

In a simple molecular crystal the atoms or molecules are in constant thermal motion about their equilibrium lattice positions. The thermal fluctuations of the molecules travel through the solid as sound waves or in quantum mechanical language, as phonons. These acoustic waves produce density fluctuations, i.e. areas of compression

and rarefaction, which in turn cause fluctuations in the dielectric tensor $\epsilon(\vec{r},t)$. The electric field of the incident radiation can be given by

$$\vec{E}'(\vec{r},t) = \vec{E}_0 \exp\{i[(\vec{k}_0 \cdot \vec{r})` - \omega_0 t]\} \quad , \tag{2.15}$$

where $\vec{E}_0$ is the amplitude, ω_0 the angular frequency, $k_0 = \frac{n}{c}\omega_0$ the wave vector of the incident radiation, c is the speed of light in vacuum, and n the refractive index of the medium. In a volume element $|d\vec{r}|$ located at a point $\vec{r}$ in the crystal, the incident radiation is scattered due to the crystal inhomogeneity introduced by the fluctuations in the dielectric tensor $\delta\epsilon(\vec{r},t)$. If a solid continuum is assumed, $|d\vec{r}|^3 \ll \lambda_0^3$, then the far field electric field amplitude at a point $\vec{R}$ is given by

$$\vec{E}'(\vec{R},\vec{q},t) = -\left(\frac{\omega_0}{c}\right)^2 \frac{(2\pi)^{-\frac{3}{2}}}{4\pi R} \sum_{\mu=1}^{3} e^{i(\vec{k}'\cdot\vec{R}-\omega' t)} \left(\hat{1}_k \times \left(\hat{1}_k \times \left(\delta\epsilon_\mu(\vec{q})\vec{E}_0\right)\right)\right) \tag{2.16}$$

In this expression $\hat{1}_k$ is the unit vector in the direction of the scattered light. The fluctuations in the dielectric tensor are expressed in terms of the Fourier components via:

$$\delta\epsilon(\vec{r},t) = (2\pi)^{-\frac{3}{2}} \sum_{\mu=1}^{3} \int d\vec{q}\ \delta\epsilon_\mu(\vec{q})\ e^{i(\vec{q}\cdot\vec{r} \mp \omega_\mu(\vec{q})t)} \tag{2.17}$$

The frequency of the acoustic sound waves is denoted by $\omega_\mu(\vec{q})$; μ indicates the possibility of having three distinct branches in the dispersion relation. From the Brillouin scattering geometry in Fig (2.1)

$$\vec{k}' = \vec{k}_0 \pm \vec{q} \quad ,$$

$$\vec{k}' = \frac{n}{c}\left(\omega_0 \pm \omega_\mu(\vec{q})\right) \quad \textit{and} \tag{2.18}$$

$$\omega' = \omega_0 \pm \omega_\mu(\vec{q}) \quad .$$

From equation (2.18) it is concluded that the incident radiation is Doppler shifted in frequency by an amount $\pm\omega_\mu(\vec{q})$. Since the change in light frequency is small (of the order of sound waves), then $|\vec{k}'| \approx |\vec{k}_0|$. Using this in combination with Figure (2.1) gives

$$|\vec{q}| = 2|\vec{k}|\sin\left(\frac{\alpha}{2}\right) \tag{2.19}$$

where α is the scattering angle. From here it can easily be shown that

$$\omega_\mu(\vec{q}) = \omega' - \omega_0 = \pm 2\frac{n}{c}V_\mu\,\omega_0\sin\left(\frac{\alpha}{2}\right) \quad . \tag{2.20}$$

This is the famous Brillouin equation; light waves are Doppler shifted when reflected from acoustic waves travelling with velocity $\pm V_\mu$. Because of the harmonic motion of the molecules the $\pm$ sign describes sound waves travelling in opposite directions; quantum mechanically it is termed phonon creation or phonon annihilation. Consequently, the Brillouin spectra will consist of two peaks corresponding to each acoustic mode, one up shifted and one down shifted from the central Rayleigh peak.

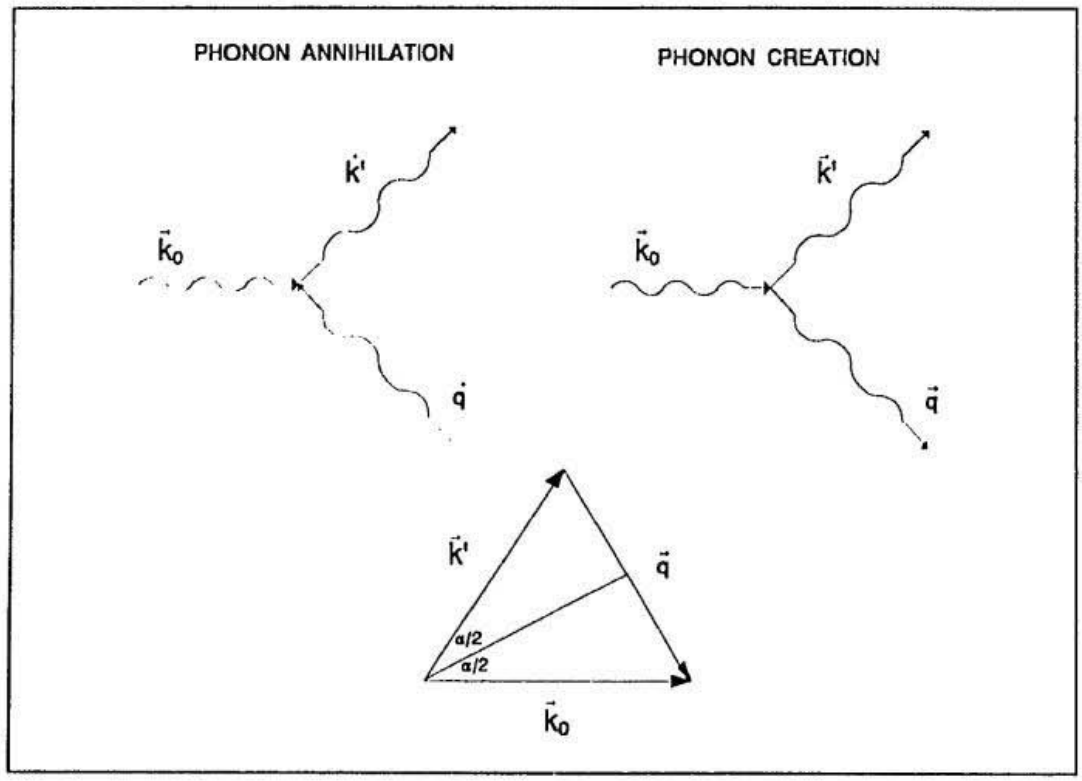

Figure 2.1: Schematic diagram of the Brillouin scattering geometry.

For a crystal under small strain there exists a coupling between the strain and the fluctuations in the dielectric tensor given by [47],[48]

$$-\frac{\delta\epsilon_{ij}(\vec{r},t)}{\epsilon_0^2} = \sum_{k=1}^{3}\sum_{l=1}^{3} P_{ijkl}\, e_{kl}(\vec{r},t) \quad . \tag{2.21}$$

This coupling is called the photoelastic effect: here $\epsilon_0 = n^2$ and P_{ijkl} are called the elasto-optic (Pockel's) coefficients. Using the matrix notation on page 17, the Pockel's coefficients can also be written as a 6x6 matrix. Like the elastic constants, there are only three Pockel's coefficients in the case of cubic crystals, namely, P_{11}, P_{12}, and P_{44}. This simplifies equation (2.21) to

$$-\frac{\delta\epsilon_{ij}(\vec{r},t)}{\epsilon_0^2} = 2P_{44}e_{ij} + (P_{11} - P_{12} - 2P_{44})\delta_{ij}e_{ij} + P_{12}\delta_{ij}\sum_{K=1}^{3} e_{ik} \quad . \qquad (2.22)$$

The average total power of the scattered radiation per unit solid angle per unit frequency at the field point $\vec{R}$ is given by

$$P(\vec{q},\vec{R}) = \frac{c}{8\pi}\left(\frac{1}{2\pi}\int_{-\infty}^{\infty} \left\langle \vec{E}'(\vec{R}',t+\tau), \vec{E}'^{*}(\vec{R},t)\right\rangle e^{i\omega'\tau}d\tau\right) \quad . \qquad (2.23)$$

Here < > denotes the autocorrelation function of $\vec{E}'(\vec{R},t)$. The scattered electric field intensity is expressed in terms of the displacement vector $\vec{u}_\mu(\vec{q},t)$ by taking the Fourier transform of the dielectric tensor. Then, by calculating the autocorrelation function of the displacement vector, the scattered power intensity is written as[17]

$$P(\vec{q},\vec{R}) = \frac{c}{8\pi}\left(\frac{\omega_0}{c}\right)^4 \frac{V}{4\pi^2}\frac{K_B T}{\rho R^2}\varepsilon_0^4 E_0^2 \sum_{\mu} \frac{|\vec{\xi}_\mu|^2 |\vec{q}|^2}{|\omega_\mu(q)|^2} \times$$
$$\frac{1}{2\pi}\left(\frac{\Gamma_\mu(\vec{q})}{(\omega' - \omega_0 - \omega_\mu(\vec{q}))^2 + \Gamma_\mu^2(q)} + \frac{\Gamma_\mu(\vec{q})}{(\omega' - \omega_0 + \omega_\mu(\vec{q}))^2 + \Gamma_\mu^2(q)}\right) \quad . \qquad (2.24)$$

Equation (2.24) gives the full details of the Brillouin spectrum. It consists of three doublets of frequency $\pm\omega_\mu(\vec{q})$, with a full width at half maximum $2\Gamma_\mu(\vec{q})$. The vector $\vec{\xi}_\mu$ arises from the Fourier transform of $\delta\epsilon(\vec{q},t)$ which is substituted into the expression for $\vec{E}'(\vec{R},t)$ and is a function of the elastic constants C_{11}, C_{12}, C_{44} and the Pockel's coefficient ratios $\frac{P_{12}}{P_{11}}$ and $\frac{P_{44}}{P_{11}}$. It also contains all the elasto-optic information and used to determine the relative intensities of the three Brillouin components. The intensity

ratio of two acoustic modes, say L and T, is given by

$$\frac{I_T}{I_L} = \left[\frac{\omega_L(\vec{q})|\vec{\xi}_T|}{\omega_T(\vec{q})|\vec{\xi}_L|}\right] \quad . \tag{2.25}$$

From measurements of the intensity ratios of the Brillouin components ratios of the Pockel's coefficients can therefore be determined.

2.4 *Dynamical Theory of Rotation-Translation Coupling in Solid Methane*

When atoms or molecules arrange themselves in a lattice at the triple point, the angular (orientational) motion of each molecule is greatly affected by its neighbours and this produces an orientational crystal field. In molecular crystals there exists a static interaction between the translational and rotational degrees of freedom. This rotation-translation (RT) coupling is of great significance near order-disorder phase transitions where molecular reorientation and lattice deformation occur at the same time. The effects of RT coupling can generally be seen in the anomalous temperature behaviour of the elastic constants due to the softening of the transverse acoustic phonons near the transition temperature.

The existence of RT coupling in methane can be inferred from a comparison of its elastic data with the elastic data of the rare gas solids. Table (2.1) gives the anisotropy A, the bulk modulus B, and the Cauchy parameter δ, for CH_4, Ne, Ar, Kr, and Xe. As mentioned earlier the fcc phase I of methane closely resembles that of the rare gas solids. Due to the lack of long range orientational order and because the crystal field does not interact with the lowest electrostatic multipole moment, the molecules can be considered as freely rotating and the corresponding rotational probability density will be almost isotropic. There are, however, vast differences between

	Ne	Ar	Kr	Xe	CD_4	CH_4
Low T	6.5 K	10 K	10 K	10 K	34.5 K	15.5 K
B (kbar)	11.02	29.97	36.5	36.4	26.9	24.11
A	2.41	2.43	2.35	2.41	3.35	2.65
δ	0.09	-0.055	-0.08	0.05	-0.38	0.00
High T	24.3 K	82.3 K	115.6 K	156 K	85.6 K	90.4 K
B (kbar)	8.77	18.33	20.36	22.6	17.1	16.2
A	2.74	2.73	2.71	2.74	3.65	3.60
δ	-0.18	-0.28	-0.27	-0.22	-0.39	-0.36

Table 2.1: Elastic constant data for the rare gas solids (see Wonneberger et al.[49] and references therein), methane and heavy methane[63].

the anisotropies of methane (A_{CH_4} = 3.3)and the rare gas solids (A_{RGS} = 2.4 - 2.7). The violation of the Cauchy relation is also much greater in methane (δ = 39%) than in the R.G.S. (δ = 18% - 22%). Recent theoretical calculations by Wonneberger and Huller[49] have shown that these differences can be attributed to the strong RT coupling which occurs in phase I of CD_4. Much of the following theory has been worked out by the above authors but has been reconstructed here to emphasise the relationship between RT coupling and the elastic constants of methane.

The mathematical formulation of the rotation-translation coupling effects in methane begins with a more general discussion of correlation functions and generalized susceptibility. A *correlation function* is the thermal average of variables which describe the physical properties of the system of interest. In the present analysis they are the molecular displacement from the equilibrium $\vec{x}(\vec{r},t)$, and the molecular rotation $\Omega(\theta,\psi,\chi,t)$ (θ, ψ, χ are the Euler angles of the molecule relative to the crystal frame).

Let $A(\vec{r},t)$ and $B(\vec{r},t)$ be observable quantities of the present system, or in quantum mechanical terms Hermitian operators. From statistical mechanics the correlation function of $A(\vec{r},t=0)$ and $B(\vec{r},t)$, denoted as $\langle A(\vec{r}), B(\vec{r},t)\rangle$, is given by the expression

$$\langle A(r), B(r,t)\rangle = \left(\frac{1}{Z}\right) Trace\left\{\exp\left(-\frac{H}{k_B t}\right)\langle A(\vec{r}), B(\vec{r},t)\rangle\right\} \tag{2.26}$$

where $Z = Trace\{\exp(-H/k_B t)\}$ is the partition function. The trace operation is expressed in terms of the eigenstates of the Hamiltonian via[50] $H|\mu\rangle = E_\mu|\mu\rangle$, in which case equation (2.26) is written

$$\begin{aligned}\langle A(\vec{r})B(\vec{r},t)\rangle &= \frac{1}{Z}\sum_{\mu} \langle\mu|\exp(-\beta H)A(\vec{r})B(\vec{r},t)|\mu\rangle \\ &= \frac{1}{Z}\sum_{\mu} \exp(-\beta E_\mu)\langle\mu|A(\vec{r})B(\vec{r},t)|\mu\rangle \quad .\end{aligned} \tag{2.27}$$

If a system in equilibrium is subject to a small perturbation at some time t=0, the response of the system is given by a correlation function in terms of the dynamic variable which couples the perturbation to the system. Assuming a linear relationship between the response and the strength of the perturbation then the response function has the form[50]

$$S(\vec{r},\vec{r}',\omega) = \int_{-\infty}^{+\infty} dt \exp(-i\omega t)\langle A(\vec{r})A^*(\vec{r}',t)\rangle \quad . \tag{2.28}$$

This form of the response function comes from Fermi's Golden Rule for transition states which is a consequence of first-order quantum perturbation theory. If the unperturbed Hamiltonian is H_0, then the new system Hamiltonian is given by

$$\begin{aligned}H &= H_0 - A^*(\vec{r}')h(t) \\ h(-\infty) &= 0 \quad ,\end{aligned} \tag{2.29}$$

where $h(t)$ is the strength of the perturbation. This assumes that the perturbation is

localized at the point $\vec{r}'$ and if the disturbance is continuous throughout the medium then $h(t)$ is replaced by $h(\vec{r}',t)$ and the contribution to the Hamiltonian by $\int d\vec{r}' A(\vec{r}')h(\vec{r}',t)$. The response in the system is measured by calculating the change in the average value of $A(\vec{r},t)$, denoted by $\delta\langle A(\vec{r},t)\rangle$, which for a linear response is given by

$$\delta\langle A(\vec{r},t)\rangle = \int_V d\vec{r}' \int_{-\infty}^{t} dt' h(\vec{r}',t')\mathrm{K}(\vec{r},\vec{r}',t-t') \qquad (2.30)$$

The function $\mathrm{K}(\vec{r},\vec{r}',t)$ is called the *linear response function*, it measures the average value of $A(\vec{r})$ due to the perturbation at time t=0. It can be shown [51] that $\mathrm{K}(\vec{r},\vec{r}',t)$ has the form

$$\mathrm{K}(\vec{r},\vec{r}',t) = \frac{i}{\hbar}\langle |A(\vec{r},t), A^{+}(\vec{r}')| \rangle \quad . \qquad (2.31)$$

For a localized disturbance with a strength function given by $h(t) = h_0 \exp(i\omega t + \varepsilon t)$ (where $h(-\infty) = 0$ and $\varepsilon > 0$), equation (2.30) has the form

$$\delta\langle A(\vec{r},\vec{r}',t)\rangle = -h_0 \int_0^t dt' \mathrm{K}(\vec{r},\vec{r}',t') \exp(-i\omega t' - \varepsilon t') \quad . \qquad (2.32)$$

The generalized susceptibility is defined to be the Laplace transform of $\mathrm{K}(\vec{r},\vec{r}',t)$

$$\tilde{\chi}(\vec{r},\vec{r}',s) = -\int_0^{\infty} dt \mathrm{K}(\vec{r},\vec{r}',t) \exp(-st) \quad ; \qquad (2.33)$$

combining this with (2.32) gives a simple relationship between the induced change in the average value of $A(\vec{r},t)$ and the generalized susceptibility,

$$\delta\langle A(\vec{r},\vec{r}',t)\rangle = -h_0 \tilde{\chi}(\vec{r},\vec{r}',i\omega); \quad \textit{where } \varepsilon \to 0 \qquad (2.34)$$

The generalized susceptibility can now be used to determine the

quantitative effects of RT coupling on the elastic properties of methane. The interaction potential is assumed to be of the Lennard-Jones type where the central carbon atoms attract each other via an r^{-6} potential, while the protons of the hydrogen atoms repel each other with an r^{-12} potential. The total interaction potential has the form [49]

$$V_t\left(\vec{R}_a - \vec{R}_b, \omega_a, \omega_b\right) = \frac{-D}{|\vec{R}_a - \vec{R}_b|^6} + \sum_{ij=1}^{4} \frac{C}{|\vec{R}_a + \vec{r}_{ai} - \vec{R}_b - \vec{r}_{bj}|^{12}} \qquad (2.35)$$

where $\vec{R}_a$ and $\vec{R}_b$ are the positions of the centres of mass of two adjacent methane molecules a and b. The orientational dependent term is given by

$$V(\vec{R}_a - \vec{R}_b, \omega_a, \omega_b) = \sum_{ij=1}^{4} \frac{C}{|\vec{R}_a + \vec{r}_{ai} - \vec{R}_b - \vec{r}_{bj}|^{12}} \qquad (2.36)$$

In the above equation $\vec{r}_{ai}$ denotes the position of the i^{th} hydrogen atom of molecule a relative to the central carbon atom, while ω_a and ω_b are the Euler angles of molecules a and b with respect to the lattice frame of reference. The constants C and D are chosen to recover the experimental values of the bulk modulus and the lattice constant. To facilitate this, equation (2.36) is expanded into cubic harmonics and averaged over the orientations of molecule b to give

$$\bar{V}(\vec{R}, \omega_b) = \frac{16\pi}{|\vec{R}|^{12}} \sum_{i=1}^{4} \sum_{l=0}^{\infty} A_l\left(\frac{r}{R}\right) \sum_{m=1}^{2l+1} K_{lm}(\theta,\varphi) K_{lm}(\theta_i,\varphi_i) \quad . \qquad (2.37)$$

Here $R = |\vec{R}_a - \vec{R}_b|$ with corresponding polar angles (θ,φ) and $r = |\vec{r}_{ai}| = |\vec{r}_{bj}|$ with corresponding polar angles (θ_i, φ_i).

To determine the mean value of the total rotational potential $\bar{W}(\omega_a)$, the average potential of equation (2.37) is averaged over the nearest neighbours of molecule a; the expression is of the form

$$\bar{W}(\omega_a) = \int d\vec{R} \int d\vec{r}\, \bar{V}(\vec{R}, \omega_a)\, \varrho_{NN}(\vec{R})\, \varrho(\vec{r}) \quad . \qquad (2.38)$$

Expanding the density of nearest neighbours $\varrho_{NN}(\vec{R})$ and the density of protons $\varrho(\vec{r})$ into

cubic harmonics, the density of protons is transformed into the crystal frame by the cubic rotator functions $U^{(l')}_{m''m'}(\omega_a)$:

$$\varrho_{NN}(\vec{R}) = \sum_{\lambda=0}^{\infty} \sum_{\mu=1}^{2\lambda+1} a_{\lambda\mu}(R)\, K_{\lambda\mu}(\theta,\varphi) \qquad (2.39)$$

$$\varrho(\vec{r}) = \sum_{l'=0}^{\infty} \sum_{\substack{m'' \\ m'=1}}^{2l'+1} b_{l'm}(r)\, K_{l'm''}(\theta,\varphi)\, U^{(l')}_{m''m'}(\omega_a) \quad . \qquad (2.40)$$

Substitution into (2.38) gives

$$\bar{W}(\omega_a) = 16\pi C \sum_{l=0}^{\infty} \sum_{\substack{m \\ m'=1}}^{2l+1} B^{l}_{mm'}\, U^{(l)}_{mm'}(\omega_a) \quad , \qquad (2.41)$$

where the coefficients $B^{l}_{mm'}$ are given by:

$$B^{l}_{mm'} = b^{0}_{lm'} \int dR\, R^2\, A_l(r/R)\, \frac{a_{lm}(R)}{R^{12}} \quad . \qquad (2.42)$$

The molecular and site symmetry will cause most of the $B^{l}_{mm'}$ to vanish, and by considering only the lowest order terms in l, (2.41) reduces to

$$\bar{W}(\omega_a) = 16\pi C \sum_{m} B^{4}_{m1}\, U^{(4)}_{m1}(\omega_a) \quad . \qquad (2.43)$$

In this discussion the lattice vibrations are assumed to perturb the rotational motion of the molecule and vice versa. The three phonon modes $\alpha = 1,2,3$ have displacements given by

$$\vec{u}_{\alpha}(\vec{R}) = -\tilde{u}(\vec{q}_{\alpha})\, \hat{e}(\vec{q}_{\alpha}) \left(\frac{2}{N}\right)^{\frac{1}{2}} \sin(\vec{q}_{\alpha}\cdot\vec{R}) \quad . \qquad (2.44)$$

The choice of wave vector $\vec{q}_{\alpha}$ and corresponding polarization vector $\hat{e}_{\alpha}$ is arbitrary so long as all three elastic constants can be determined from the frequencies of these modes.

For simplicity wave vectors in the high symmetry directions are chosen: they are shown in Table (2.2) along with their corresponding mode stiffness $v_\alpha^2 \rho$.

Substituting $\vec{R} \rightarrow \vec{R} + \vec{u}_\alpha(\vec{R})$ back into (2.39) and (2.41), the orientational potential of molecule n due to its twelve nearest neighbours is expressed as

$$\bar{W}(\vec{q}_\alpha, \omega_n) = C\left\{16\pi B_{11}^4 U_{11}^{(4)} - \vec{u}(\vec{q}_\alpha)\left(\frac{2}{N}\right)^{\frac{1}{2}} \sin\left(\frac{q_\alpha a}{\kappa_\alpha}\right) \times \cos(\vec{q}_\alpha \cdot \vec{R}_\alpha) \sum_m W_{\alpha m} U_{ml}^{(4)}(\omega_n)\right\} \tag{2.45}$$

where a is the lattice constant. By defining the quantities

$$\Omega^{(4)}(\omega_n) = \sum_m \frac{W_{\alpha m}}{W_\alpha} U_{ml}^{(4)}(\omega_n)$$

$$W_\alpha = \left(\sum_m W_{\alpha m}^2\right)^{\frac{1}{2}} \quad , \tag{2.46}$$

$$\hat{W}(\vec{q}_\alpha) = \left(\frac{2}{N}\right)^{\frac{1}{2}} \sin\left(\frac{qa}{\kappa_\alpha}\right) \cos(\vec{q}_\alpha \cdot \vec{R}_\alpha) W_n \quad , \tag{2.47}$$

and then substituting back into (2.45) implies

$$W(\vec{q}_\alpha) = C\left[16\pi B_{11}^4 U_{11}^{(4)} - \vec{u}(\vec{q}_\alpha) \hat{W}_n(\vec{q}_\alpha) \Omega^{(4)}(\omega_n)\right] \quad . \tag{2.48}$$

Equation (2.45) is a perturbed Hamiltonian of the form

$$H(t) = H_0 - \sum_l F^{(l)}(t) \Omega^l \quad . \tag{2.49}$$

In this case the generalized force is given by $F^{(1)}(t) = C\hat{W}_n(\vec{q}_\alpha)\tilde{u}(\vec{q}_\alpha)$ and the rotational variable by $\Omega^1 = \Omega^4(\omega_n)$. The rotational susceptibility, $\chi_{\Omega^4}(\omega)$, is calculated by combining (2.48), (2.31), and (2.33) to give

$$\chi_{\Omega^4}(\omega) = \frac{i}{\hbar}\int_0^\infty e^{i\omega t}\langle[\Omega^4(t),\Omega^4(0)]\rangle dt \qquad (2.50)$$

Using the eigenstates of the unperturbed spherical top, the closed form expression of equation (2.50) is given by

$$\chi_{\Omega^4}(\omega) = \frac{2\beta}{(2(4)+1)^2}\sum_{n=1}^{4} e^{-\beta n^2/4}\left[1 - \frac{\beta n^2}{2} + \frac{\beta\omega^2}{2n^2} + \beta^{\frac{3}{2}}\left(\frac{\omega^3}{4n^3} - n\omega\right)\sqrt{\pi}\,i\zeta\left(\frac{\omega\sqrt{\beta}}{2n}\right)\right] \qquad (2.51)$$

where ζ is the complex error function.

In an interacting system the Hamiltonian can be expanded in the form

$$H = \sum_{i=1} H_i(Q_i,P_i) - \frac{1}{2}\sum_{ij}\pi_{ij}Q_iQ_j \qquad (2.52)$$

with generalized coordinates Q_i, momenta P_i, and coupling coefficients π_{ij}. If H_i denotes the Hamiltonian of uncoupled degrees of freedom, then it has a corresponding dynamic susceptibility χ_i when it is subject to a perturbation $H_i'(t) = -F(t)Q_i$. It can be shown [3] that there exists a relationship between the coupled and uncoupled susceptibilities χ_{ij} and χ_i given by

$$\chi_i(\omega) = [\mathbf{1} - \boldsymbol{\chi}(\omega)\boldsymbol{\pi}]^{-1}_{ij}\chi_j(\omega) \quad , \qquad (2.53)$$

where $\boldsymbol{\chi}(\omega)$ is the diagonal matrix of uncoupled susceptibilities, and $\boldsymbol{\pi}$ is the matrix of

coupling coefficients. This investigation consists of a translational and a rotational degree of freedom with a corresponding Hamiltonian

$$H = H_T + H_\Omega - H_{T\Omega} \quad . \tag{2.54}$$

The phonon Hamiltonian is given by

$$H_T = \frac{P^2(\vec{q}_\alpha)}{2m} + \frac{1}{2} m \omega_0^2(\vec{q}_\alpha) \tilde{u}^2(\vec{q}_\alpha) \tag{2.55}$$

with corresponding susceptibility [50]

$$\chi_T(\vec{q}_\alpha, \omega) = \frac{1}{m} \frac{\omega_0^2(\vec{q}_\alpha) - \omega^2 + i\gamma\omega}{\left(\omega_0^2(\vec{q}_\alpha) - \omega^2\right)^2 + \gamma^2\omega^2} \quad , \tag{2.56}$$

m being the mass of the molecule, ω_0 the phonon frequency, and γ the damping constant. The rotational term H_R is in the form of the spherical top and the corresponding susceptibility is given by equation (2.51), while the interaction term H_{TR} is given by equation (2.48)

$$H_{T\Omega} = C\tilde{u}(\vec{q}_\alpha) \sum_{n=1}^{N} \hat{W}_n(\vec{q}_\alpha) \Omega^4(\omega_n) \quad . \tag{2.57}$$

Using the periodicity relation $\frac{1}{N}\sum_{n=1}^{N} e^{i\vec{q}\cdot\vec{R}_n} = \delta_{\vec{q},0}$ it can be shown that

$$\sum_{n=1}^{N} \hat{W}_n^2(\vec{q}_\alpha) = W_\alpha^2 \sin^2\left(\frac{qa}{\kappa_\alpha}\right) \quad . \tag{2.58}$$

Substitution of (2.48), (2.56),(2.57) and (2.58) into (2.53) gives the coupled phonon-phonon susceptibility

$$\chi_{TT}(\vec{q}_\alpha,\omega) = \chi_T(\vec{q}_\alpha,\omega)\left(1 - \chi_T(\vec{q}_\alpha,\omega)\,\chi_{\Omega^4}(\omega)\,C^2 W_\alpha^2 \sin^2\left(\frac{qa}{\kappa_\alpha}\right)\right)^{-1} \quad . \tag{2.59}$$

In the limit $|\vec{q}| \to 0$, $\omega \to 0$ the acoustic phonon velocity is given by

$$v_\alpha^2 = \lim_{|q_\alpha| \to 0} \lim_{\omega \to 0} \left(\chi_{TT}(\vec{q}_\alpha,\omega)\,|\vec{q}_\alpha|^2 \omega\right) \quad . \tag{2.60}$$

Substituting the modes in Table 2.2, then replacing χ_T by the uncoupled elastic constants (C_{11}^0, C_{12}^0, C_{44}^0), and χ_{TT} by the coupled constants (C_{11}, C_{12}, C_{44}), the following expressions are obtained

$$\begin{aligned}
C_{11} &= C_{11}^0 - \frac{1}{a}\chi_{\Omega^4}(0)C^2 W_1^2 \\
C_{44} &= C_{44}^0 - \frac{1}{a}\chi_{\Omega^4}(0)C^2 W_2^2 \\
C_{12} &= C_{12}^0 + \frac{1}{a}\chi_{\Omega^4}(0)C^2\left(4W_3^2 - W_1^2\right) \\
B &= B^0 + \frac{1}{a}\chi_{\Omega^4}(0)C^2\left(8W_3^2 - 3W_1^2\right).
\end{aligned} \tag{2.61}$$

The expressions (2.61) give a quantitative interpretation of the effects of RT coupling on the elastic constants of CD_4. This classical mean field approach is probably not as valid in the case of CH_4 due the more quantum nature of the molecular rotations. These equations, nevertheless, give some indication of how the elastic constants of CH_4 will behave across the I-II transition. From chapter 1 it is known that the rotational motion

decreases from phase I to phase II. By considering Phase I as a state with strong RT coupling and phase II as a state with a weaker coupling of the rotational modes, then increases should be seen in C_{11} and C_{44}, while there should be a decrease in C_{12}.

Mode (α)	1	2	3
$\vec{q}_\alpha$	(0,0,1)	(0,1,0)	$(1,1,0)/\sqrt{2}$
$\hat{e}_\alpha$	(0,0,1)	(1,0,0)	$(1,-1,0)/\sqrt{2}$
$v_\alpha^2 \cdot \rho$	C_{11}	C_{44}	$(C_{11} - C_{12})/2$
κ_α	2	2	$\sqrt{2}$

Table 2.2: Table of high symmetry phonon data. Given are the directions, polarizations and mode stiffness.

Chapter 3:

Experimental Setup

3.1 Optical Configuration

A schematic representation of the experimental setup can be found in figure (3.1). This Chapter encompasses only a brief summary; a more complete and detailed description can be found elsewhere.[52][53] Single crystals of CH_4 are grown in a cylindrical quartz cell encased in a liquid helium cryostat. Highly coherent, monochromatic radiation at 514.5 nm from a single mode argon laser (Spectra Physics 2020 and 165-08) is incident vertically along the axis of the cell. The scattering is observed horizontally through a Brillouin spectrometer. The spectrometer consists of a piezoelectrically - scanned Fabry-Perot interferometer (FP), a photomultiplier tube, an amplifier discriminator (A-D), and a data acquisition and stabilization system (DAS-1). The DAS-1 stores the spectrum in a 1024/512 multichannel memory and displays the spectrum on a CRT screen.

The main components of the optical setup are also diagrammed in figure (3.1). The optic axis of the spectrometer is defined by a He-Ne laser which designates the Y-axis of the laboratory reference frame. The beam of the argon laser is directed vertically along the axis of the cell and defines the Z-axis. The beam is polarized along

the X-axis and intersects the He-Ne beam at 90°. With the laboratory reference frame defined, the axis of the X-ray collimator CO is aligned with the optic axis. This ensures that the radiation from the X-ray machine passes through the crystal along the optic axis and is necessary to determine the orientation of the crystal axis. The laser beam is focused by a quartz lens L1 (focal length 30 cm) and directed along the axis of the cell by a high quality mirror M. The apertures A1 and A2 are used to block any unwanted radiation, especially reflections. A high quality quartz lens L2 (focal length 45 cm) is focused on the centre of the cell, to ensure that the FP only receives light parallel to the optic axis. From the interferometer, the light is then focused on to a pinhole A4 (600 micron diameter) via another quartz lens L4 (focal length 80 cm). The light passing through the pinhole is then collected and digitized by a combination photomultiplier tube (PMT) (model ITT FW130) and amplifier-discriminator (AD). The resulting pulses then feed into the DAS-1 where each scan is added to its running memory and the resultant spectrum displayed on a CRT screen.

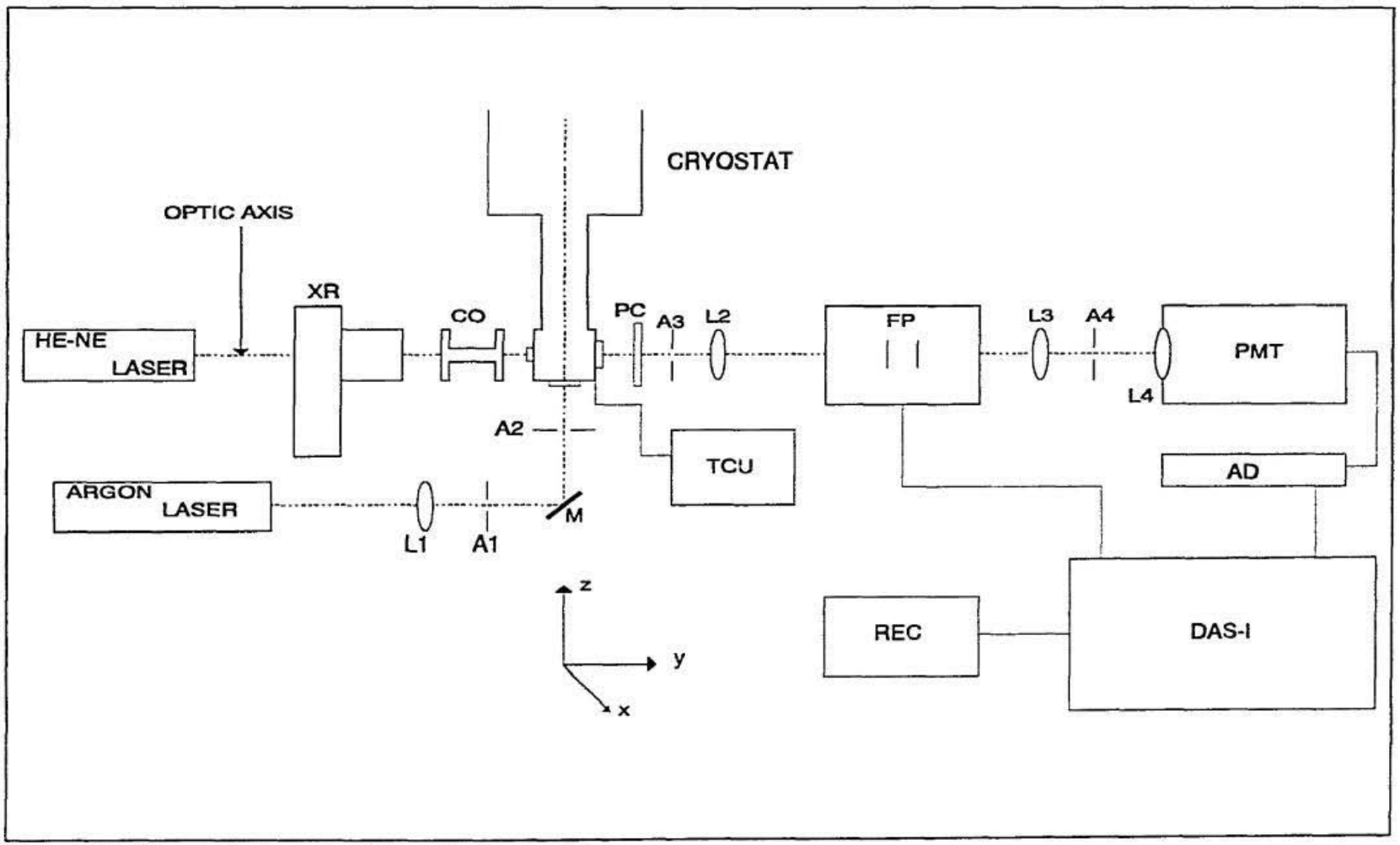

Figure 3.1: Schematic diagram of the optical apparatus.

The Fabry-Perot Interferometer

In this experiment the Brillouin spectrometer uses a commercial Fabry-Perot interferometer (FP) (Burleigh RC110). It is constructed of Superinvar and consists of a cavity formed by two parallel transparent plates separated by a distance d; the plates in this experiment are flat to within $\lambda/200$. The plates are coated with a highly reflective film of reflectivity R and transmission coefficient T. The front mirror is placed on a mount which is adjustable using three fine micrometer screws, while the mount for the back mirror consists of three piezoelectric transducers in triangular geometry.[57] An applied voltage causes these transducers to expand and contract, enabling the mirror to translate and tilt in any direction.

When light rays enter the FP parallel to the optic axis, the only wavelengths to pass through are those which satisfy the resonance condition

$$2nd = m\lambda \quad , \tag{3.1}$$

where n is the index of refraction of the medium in the cavity ($n = 1$ for air), and m is the order of interference. By moving the back mirror, thereby varying the distance d, different wavelengths are passed, and the FP essentially acts as a tunable frequency filter. The range of frequencies between two consecutive orders is called the Spectral Free Range (SFR) and is given by

$$SFR = \frac{c}{2nd} \quad . \tag{3.2}$$

The SFR is changed by adjusting the average separation between the two plates. This is done for two reasons: (1) to increase the resolvable bandwidth of the spectrometer and (2) to overcome the problem of overlapping Brillouin components from different orders. In this experiment two different values are used. SFR_1 = 16.43 GHz is used for the first 6 crystals but component overlap forced a change to SFR_2 = 18.27 GHz for the last

crystal (#7).

As stated earlier, high resolution is a necessity for Brillouin spectroscopy. The minimum bandwidth $\Delta\omega$, sometimes called the full width at half maximum (FWHM), is governed by a factor called the finesse F. The finesse is defined in terms of the SFR through the relationship

$$F = \frac{SFR}{\Delta\omega} = \frac{SFR}{FWHM} \quad . \tag{3.3}$$

Another important quantity used to determine the quality of Brillouin spectra is the contrast C, defined as the ratio of the transmission maximum to the transmission minimum:

$$C = \frac{T_{max}}{T_{min}} \quad . \tag{3.4}$$

On the screen of the DAS-1, this is effectively equal to the ratio of the height of the Rayleigh peak to the background noise (minus the PMT darkcount). The ability to obtain high values of finesse and contrast depends on the flatness of the mirrors, their reflectivity, and the overall optical alignment. In addition, in this experiment high finesse and contrast are obtained by placing the FP in the triple pass mode, whereby the scattered light passes through the FP cavity three times. This is equivalent to having the light pass through three FPs in series. Triple passing is accomplished by using retroreflectors. These are the corners of a fused quartz cube which have the property that the incident beam is displaced laterally, and returned parallel to the incident direction. Triple passing in this experiment increases the finesse by a factor of about 3 and cubes the contrast. Typical values for the finesse were from 50 - 65, while the contrast was about 10^6 - 10^7. To overcome the decrease in throughput of the Fabry-Perot, mirrored coatings with high transmission and lower reflectivity (such as 93% in this experiment) are used.

The Data Acquisition System (DAS-I)

After the scattered light passes through the Fabry-Perot it enters the photomultiplier tube where the radiation is detected by the A-D which renders each detected photon as a 1V pulse. This digital output is fed into a commercial data acquisition and stabilization system (Burleigh DAS-I). The DAS-I performs important functions necessary for recording and analyzing the Brillouin spectrum. (1) The DAS-I displays the digital input on a CRT screen via a 1024/512 multichannel analyzer (MCA). When a channel is accessed, by a moveable cursor, the channel number and the number of photon counts are displayed on screen. There is a direct correspondence between channel number and frequency which facilitates the measurement of the frequency shifts of the Brillouin components. (2) The DAS-I also acts as a stabilization unit for both the laser cavity, the electronics, and the Fabry-Perot mirrors, by maintaining the central Rayleigh component within a stabilization window centred on a particular channel. (3) Through the long collection process, high values of finesse and contrast are maintained by the finesse optimizer of the DAS-I . The finesse optimizer keeps the FP plates as parallel as possible. (4) A final feature of the DAS-I is the segmented ramp which allows more photon counts to be accumulated in selected regions. These selected regions, called segments, are important for measuring the position of the weak transverse features of the Brillouin spectrum.

3.2 The Liquid Helium Cryostat

The cryostat used in these experiments has been described in detail elsewhere.[52] [58] A schematic diagram is of the cryostat is shown in figure (3.2). The cryostat was manufactured by Janis Research Co. (Model 10DT) and was modified to

allow the cell assembly (16) to be in vacuum. The outer body of the cryostat is made of stainless steel and contains two cryogenic liquid reservoirs. The outer reservoir (8) is for liquid nitrogen, while the inner one (9) contains liquid helium. The nitrogen supply is maintained by a level indicator and controller (American Mag. Inc., Model KE 101) which refills the reservoir automatically every 4 hours from a 200 litre tank. The helium level is monitored by a helium level indicator (American Mag. Inc., Model KE 101) and the reservoir is manually refilled every two days from a 60 litre tank.

The cell is connected to a long stainless steel tube (2) which is centred in the bore of the cryostat by teflon spacers (21). This in turn is connected to an internal brass tube (1) which serves as the inlet for the sample CH_4 gas. The cell can be rotated easily through the use of rotary seals (29,30) at the top of the cryostat. These seals also enable the cell assembly to be raised and lowered within the body of the cryostat.

The cold temperatures are maintained by the flow of liquid helium down a capillary tube (22) to a heat exchanger (20). The helium flow is adjusted by a needle valve (23) which is opened by a control knob (28). The control knob is opened automatically by an electric motor connected to the heat exchanger's temperature control unit. The vaporized helium returns to the helium recovery system via outlet (4). A brass rod protrudes on each side of the heat exchanger and acts as the cold finger. Each rod is connected to a copper braid (19) which is in turn connected to clamps on the top and bottom of the cell. To help control the temperature, 50 Ω of resistance wire (12) is wrapped around the heat exchanger and used as a heating element.

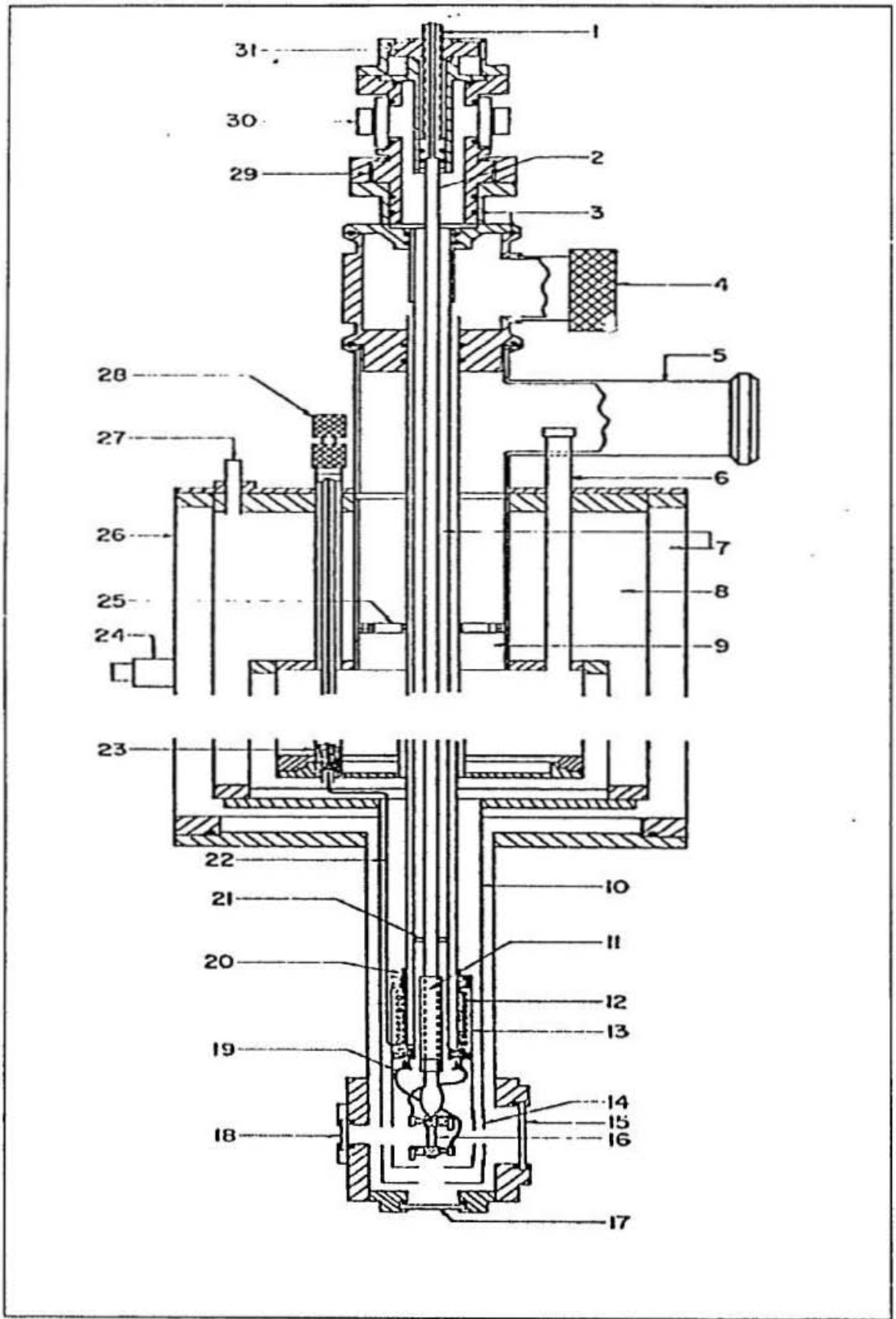

Figure 3.2: Diagram of the liquid helium cryostat (not to scale).

1 Brass inlet tube
2 Stainless steel tube
3 Rubber O-rings
4 Port for He recovery from heat exchanger
5 Port for He recovery from He reservoir
6 Inlet for liquid He fill
7 Space under vacuum
8 Liquid nitrogen reservoir
9 Liquid helium reservoir
10 Radiation shield
11 Dust collector assembly
12 Heater wires
13 Radiation shield
14 Aluminum foil
15 Plexiglass large window
16 Quartz sample cell
17 Polished quartz window
18 Plexiglass small window
19 Copper Braids
20 Heat exchanger
21 Teflon Spacer
22 Liquid helium capillary tube
23 Needle valve
24 Cryostat pumping port and electrical feedthrough
25 Thermal anchor
26 Polished stainless steel outer wall of cryostat
27 Liquid nitrogen fill inlet
28 Control knob for the needle valve
29 Rotary seal for rotating the sample cell
30 Electrical feedthrough for temperature and gradient measurements
31 Assembly for raising and lowering the cell

The Cell Assembly

A schematic diagram of the cell assembly is shown in figure (3.3). It consists of a cylindrical quartz tube (5 mm outer diameter, 3 mm inner diameter, 2 cm high) with a kovar seal at the top. The kovar is soldered to a beryllium-copper dust trap, which in turn is connected to the steel tube ((2). A highly polished quartz plug is epoxied to the bottom of the cell and provides a window for the laser beam, plus a cold spot for crystal growth. Two spring clamps are attached to the bottom and top of the cell. In addition to cooling, the clamps also provide a place where gallium-arsenide and silicon diodes are placed in thermal contact with the cell wall, these are used for temperature control and measurement. The clamps also contain a housing for a differential thermocouple used to monitor the temperature gradient across the sample.

A unique feature of this cell is the optically transparent but electrically resistive (10 Ω) film which surrounds the outside wall. The heating action of the film aids in crystal growth by reducing the possibility of crystal nucleation on the cell wall. The film is also used extensively and is crucial in the cooling procedure. It first melts the crystal from the cell wall and provides a sufficient amount of heat to stop crystal regrowth during the cooling period.

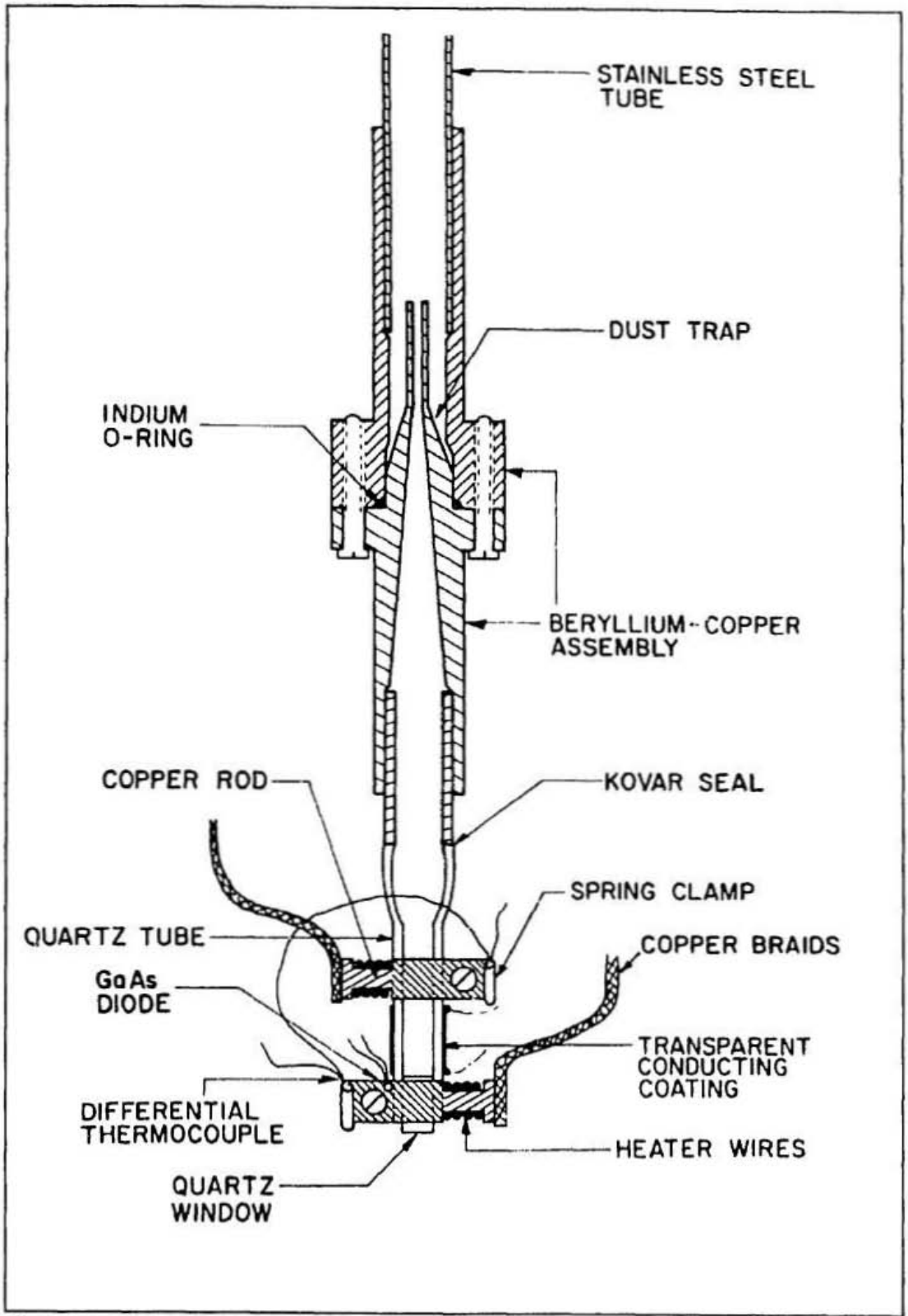

Figure 3.3: Schematic diagram of the cell assembly (not to scale).

3.3 Temperature Control and Diode Calibrations

The cell temperature is governed by the heat transfer from the heat exchanger to the clamps on the cell via the copper braids. The temperature of the heat exchanger is determined mainly by regulating the flow of helium down the capillary tube. The temperature of both the heat exchanger and cell are further controlled by a cryogenic temperature indicator/controller (Lake Shore Cryotronics Inc., Model DTC-500) used in conjunction with the gallium-arsenide (GaAs) and a silicon (Si) diodes. The diodes have the characteristic that when a constant current flows through, the voltage increases with decreasing temperature.

More specifically, the temperature of the heat exchanger was cooled to about 5 K below the cell temperature by opening the needle valve. The voltage on the diode (either GaAs or Si) is compared to the set point voltage on the controller. The difference is amplified and used to regulate the current flowing through the 50 Ω resistance wires. When this current reaches a limiting value, the controller sends an electric signal to the electric motor and automatically opens the needle valve. This method maintains the temperature of the heat exchanger with an accuracy of ± 0.5 K. With the latter temperature stable, the cell temperature is controlled by a second indicator/controller in the same manner as described above to a long term accuracy of better than ± 0.01 K. The cell temperature gradient is controlled in a similar manner using the differential thermocouple and a custom-made controller.

GaAs and Silicon Diode Calibrations

The early stages of this investigation were hampered by the inability to accurately pinpoint the CH_4 I-II transition temperature using the diodes. Previous

investigations used the GaAs diode, whose calibration curve was linear only in the temperature range T>40 K. The Si diodes however contained two regions of linearity, T>25 K and T<21 K. The first region was calibrated at the same time as the GaAs diode, the low temperature of the phase transition, however, required the calibration of the second region.

The low temperature calibrations were achieved by placing pure samples of hydrogen (99.99% pure, Matheson Gas Company) and neon (99.98% pure, Matheson Gas Company) into the quartz cell of the cryostat. The hydrogen had a boiling point of T_{boil}=20.0 K at 650 mmHg, and a triple point T_{tp}=13.8 K. The neon had a triple point T_{trp}=25.4 K. By observing the phase changes above, the corresponding voltages were recorded and used to calibrate the low temperature regions of both the GaAs and silicon diodes. The resulting calibration curve for silicon is shown in figures (3.4). In the low temperature region, the Si diode is very sensitive and provides a precise and stable temperature reading. Other points shown in figure (3.4) are, from 40 K to 90 K respectively, (1) β-γ O_2 phase transition, (2) O_2 triple point, (3) α-β CO phase transition, (4) N_2 triple point, (5) CO triple point, (6) Ar triple point, (7) and the CH_4 triple point. The points were initially used by Ahmad[52] and Askarpour[53] to calibrate GaAs and were transferred to calibrate the Si diode.

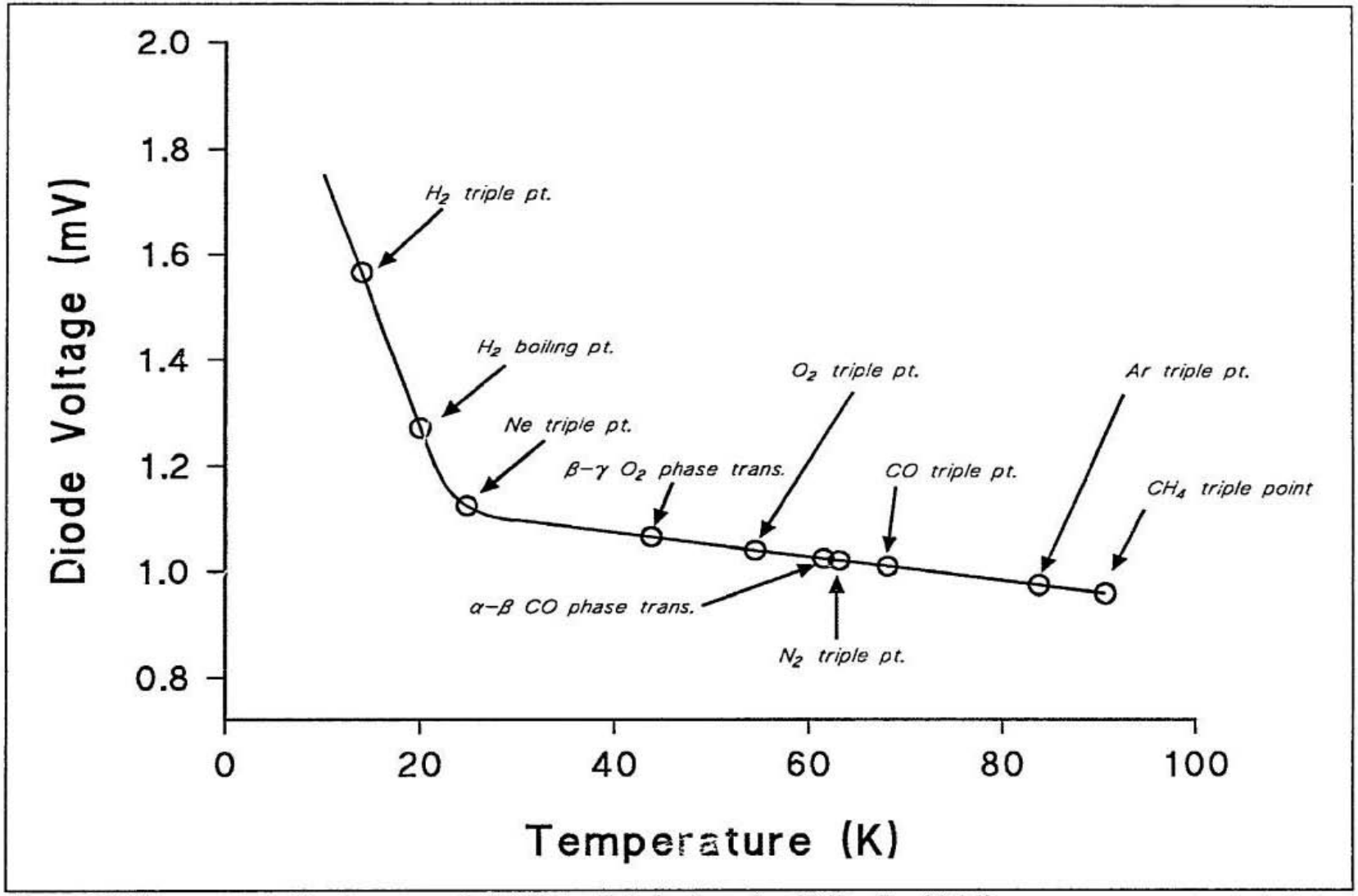

Figure 3.4: Temperature calibration curve of the silicon diode in the region 10 K < T < 90.6 K.

Chapter 4

Experimental Procedures and Data Analysis

4.1 Crystal Growth and Cooling

One single crystal growing technique has been described in detail in two previous investigations.[52][53] It is based upon Bridgemann's method [59] where the solid forms slowly from the liquid, from just above the triple point, in the presence of a temperature gradient. However, two rapid growth techniques are also used for growing single crystals. The first involves cooling the liquid quickly from just above the triple point, the other involves cooling the liquid quickly from temperatures much higher.

All growing procedures begin by filling the nitrogen reservoir and precooling the cryostat for 12 hours. The helium reservoir is then filled and the needle valve adjusted until liquid forms in the cell. In the slow growing process (method #1), the cell temperature is lowered to 0.5 K above the triple point and the liquid is left in equilibrium for about 2 hours. After this time, the temperature of the cell is automatically lowered by 0.05-0.1 K per hour. This is an overnight process and produces a seed crystal of 1-2 mm in height. The cooling occurs while a temperature gradient of 2 K is maintained between the top and bottom of the cell, and a voltage of 15 mV is applied to

the resistive film. The seed crystal is then grown to a height of 1 cm in a period of 2-3 hours by further reducing the temperature. Laue X-ray photographs are then taken to ensure the crystal is single and of good quality. Strained or polycrystalline samples are melted and the growing procedure is repeated until a high quality crystal is obtained.

An alternative method involving rapid growth begins with liquid in the cell as described above. The cell temperature is then quickly lowered until solid forms in the bottom of the cell. This generally involves supercooling to a temperature ~1 K lower than the triple point. This solid equilibrates for about 1 hour and then the temperature is slowly increased until the solid just disappears from the cell bottom (about 0.05-0.1 K above the triple point). After settling down for 2-4 hours, the temperature of the cell is quickly lowered by 0.2-0.3 K, to produce a seed crystal 2-3 mm in height. The seed is left for about 1 hour and then slowly grown manually to a height of 1 cm, at which point X-ray photographs were taken.

A variation of the rapid growth technique begins at temperatures well above the triple point. The cell temperature is first raised to 20 K above the triple point and left in equilibrium for 2 hours. The needle valve is then completely opened to allow liquid helium to saturate the heat exchanger. This causes the cell temperature to fall rapidly and the triple point is reached in less than 20 minutes. Once the triple point is reached, the needle valve is closed and the heat exchanger begins to warm up. Although the latter is still cooling the cell, closing the valve limits the cell temperature to about 1 K below the triple point. This procedure produces a seed crystal which grows very fast. Once the seed is detected the cell temperature is warmed to contain the crystal to a height of 1 cm. While this procedure is fast, it is also very delicate and has to be watched carefully. The heat exchanger has to be cooled to just the right amount so that the cooling of the cell can be stopped within 5 minutes.

The rapid growth methods involved a remarkably high success rate ~35% for the growth of high quality single crystals. It is important to emphasize, however, that

this requires maintaining a voltage to the resistive film of -150 mV. Much difficulty occurs when crystals are grown without the presence of a film voltage. This was demonstrated at one point when the film voltage was lost due to an electrical malfunction.

Cooling Procedure

The cooling of molecular solids is unique to the experiments conducted in this laboratory. Obtaining high quality crystals at low temperatures involves several factors: (1) the crystal must remain single, and relatively free of internal strain; (2) the outer surface of the crystal must be parallel to the cell wall to ensure a scattering angle of 90°; (3) the crystal wall must remain transparent and non-amorphous to allow scattered light to pass through. The resistive film surrounding the cell allows quality single crystals to be grown with little strain. Crystals cooled in a previous investigation[54] were dome shaped and free standing in the cell. The dome shape introduces an unknown scattering angle due to refraction, while the crystals lose their transparency due to small crystallites growing on the sides. To solve these problems a cooled crystal must be obtained that will adhere to the walls of the cell.

The previous cooling method is described in detail[54]. It involves two coolings, one from 90 K to 70 K, the other from 70 K to 50 K. Once 50 K is reached the thermal expansion is low enough to allow further cooling without having to free the crystal from the cell wall. In the first stage slow pumping is used, in conjunction with the resistive film, to remove the crystal from the cell wall and keep it free standing through the cooling duration. The crystal then regrows against the cell wall. In the second stage only pumping is used to remove the crystal and keep it free standing throughout. The pumping reduces the vapour pressure so much, that the crystal will fail to regrow a second time, leaving a domed-shaped crystal with a non-transparent surface.

Several other methods were attempted to try to obtain a quality crystal at 50 K. The pumping, however, continued to be a problem. With this in mind a successful cooling method was found (quite by accident) that reduced the amount of pumping. It was accomplished by increasing the maximum voltage applied to the resistive film to up to 600 mV whereas in the previous method the film voltage was raised to a maximum of 350 mV. The extra heat energy reduced the amount of pumping required to keep the crystal away from the cell wall during cooling. Only one cooling stage was used with the crystal temperature being reduced from 90 K to 60 K. Further cooling was accomplished with the crystal stuck to the cell wall. To date three CH_4 single crystals have been successfully cooled below 30 K, two crystals at 25 K, and one crystal at 15.5 K. The full recipe for cooling single crystals is given below.

The cooling is controlled by an automatic cooling unit (ACU) which has a built in digital counter. The counter ranges from 0 to ~3600, which corresponds to a voltage increase of ~80 mV, and a temperature decrease of ~7 K. To begin cooling a fine, balanced pumping rate must first be established (a good pumping rate will cause a pressure decrease of ~20 mmHg in 30 minutes). The cell entry valve is opened very slowly (about $\frac{1}{50}$ th of a turn every 2 minutes) until the needle on the cell pressure begins to fall. If the pressure decreases too fast, the valve is closed to slow the pumping process, and then reopened by $\sim\frac{1}{100}$ th of a turn every 30 minutes until the desired rate is established. With the desired pumping rate established, the film voltage is increased from 150mV by 10mV every 15 minutes up to a maximum of 250mV or until the crystal breaks free of the walls. While the pressure in the cell is dropping, the crystal itself begins to grow. At the start the seed should be about 3-5 mm in height, and it generally grows to a height of 1.5-2.0 cm before it breaks free of the cell wall. Once the crystal is free standing the automatic cooler is engaged and the temperature is decreased. When the ACU is started, the readings on the cell temperature control unit (TCU) change, the current in the cell's heater decreases and the null detector on the cell's TCU will not read

zero. This means that the heat exchanger is cooling the cell slower than the rate established by the ACU. To overcome this, the heat exchanger must be cooled at a faster rate by manually opening the helium valve. If the heat exchanger is cooling properly, the null detector on the cell TCU reads zero, and there is a current of 0.06-0.08 mA in the heater wires. While the temperature is being lowered, the cell must be watched very carefully. At the same time, the voltage on the film is increased by 10 mV, after every 500 counts on the ACU. A point is reached where the crystal regrows along the walls at the cell bottom. The ACU is stopped and the cell entry valve is opened slightly. Once the crystal again becomes free, cooling can be resumed. When the desired temperature is reached (60 K in this experiment) the ACU is shut off and the temperature is maintained by the cell's TCU. The cooling to this stage usually involves a total time of about 3 hours. The crystal then regrows against the cell wall in the presence of a high film voltage. When the crystal comes to equilibrium (usually 12 hours), the film voltage is decreased to 200 mV in 10 mV steps every 5 minutes. Further cooling is accomplished by lowering the cell temperature manually via the TCU. A good cooling rate during this latter stage is about 5 K per hour, a faster rate may induce a small amount of internal strain.

4.2 Crystal Orientation Procedure

Determination of the elastic and photoelastic constants requires that the scattering wave vector $\vec{q}$ must be known in the crystal's frame of reference. The orientation of the crystal axes, with respect to the lab frame, are expressed in terms of the Euler angles (θ, ϕ, χ). Their mathematical representations and the transformation matrices can be found in any standard mechanics text, however a graphical representation is shown in figure (4.1).

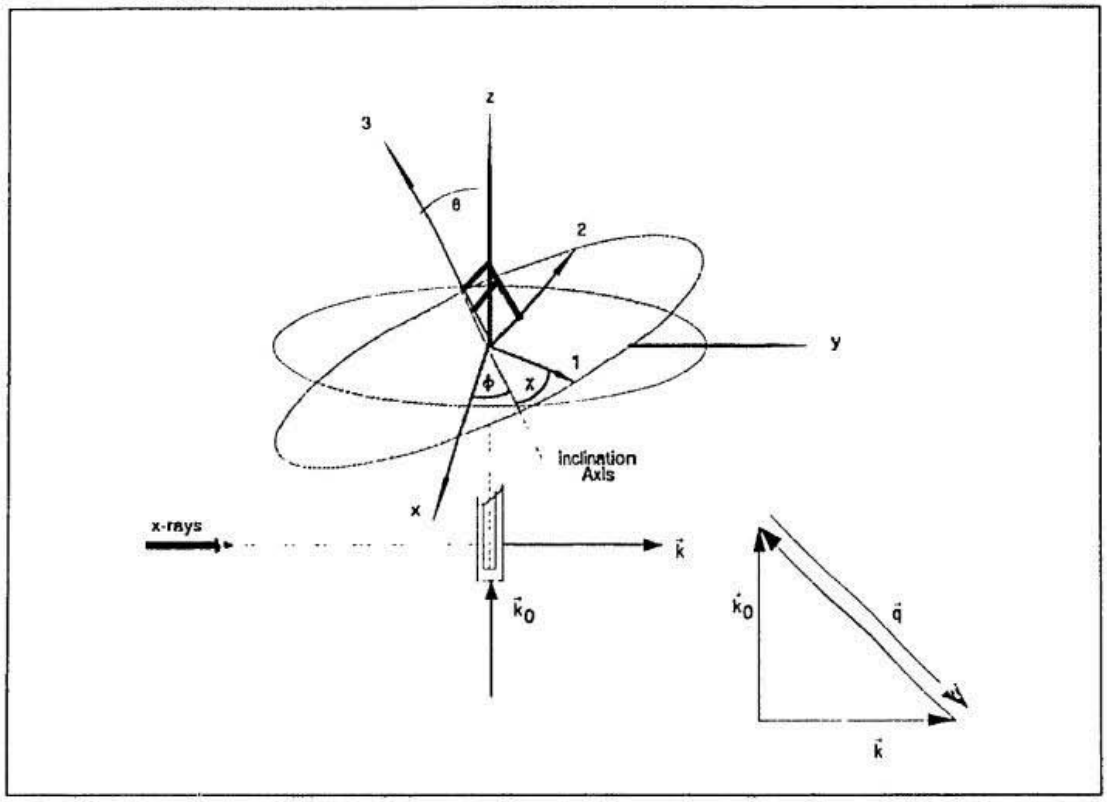

Figure 4.1: Diagram showing the Euler angles (θ,ϕ,χ) used to transform from the laboratory reference frame to the crystal reference frame. The vectors $\vec{k}$, $\vec{k}_0$, and $\vec{q}$ which define the scattering geometry are also shown.[12]

The orientation is found by analyzing X-ray transmission Laue photographs[60]. The X-ray source is a water-cooled Phillips MO 100/Be 100 kV beryllium window tube which is operated at 70 kV and 10 mA. The beam is incident on the crystal along the optic axis. The scattered X-rays produces a Laue diffraction pattern which is recorded on Polaroid 57 X-ray film. The film is mounted perpendicular to the optic axis in a Polaroid XR-7 Land Diffraction Cassette. The Laue photograph consists of a central round spot corresponding to the undiffracted beam, and several elliptical spots, due to the constructive interference of the diffracted X-rays from a set of Bragg planes. The orientation procedure is based on the theory of stereographic projection[60];

it is simply a way of taking the relationships among the crystal planes in 3 dimensions, and expressing them in 2 dimensions. In figure (4.2) the coordinates of the Laue spots (x',z') are measured using a rectangular grid with a grid spacing of 0.025 cm. They represent the input for a computer program used to calculate the Euler angles.

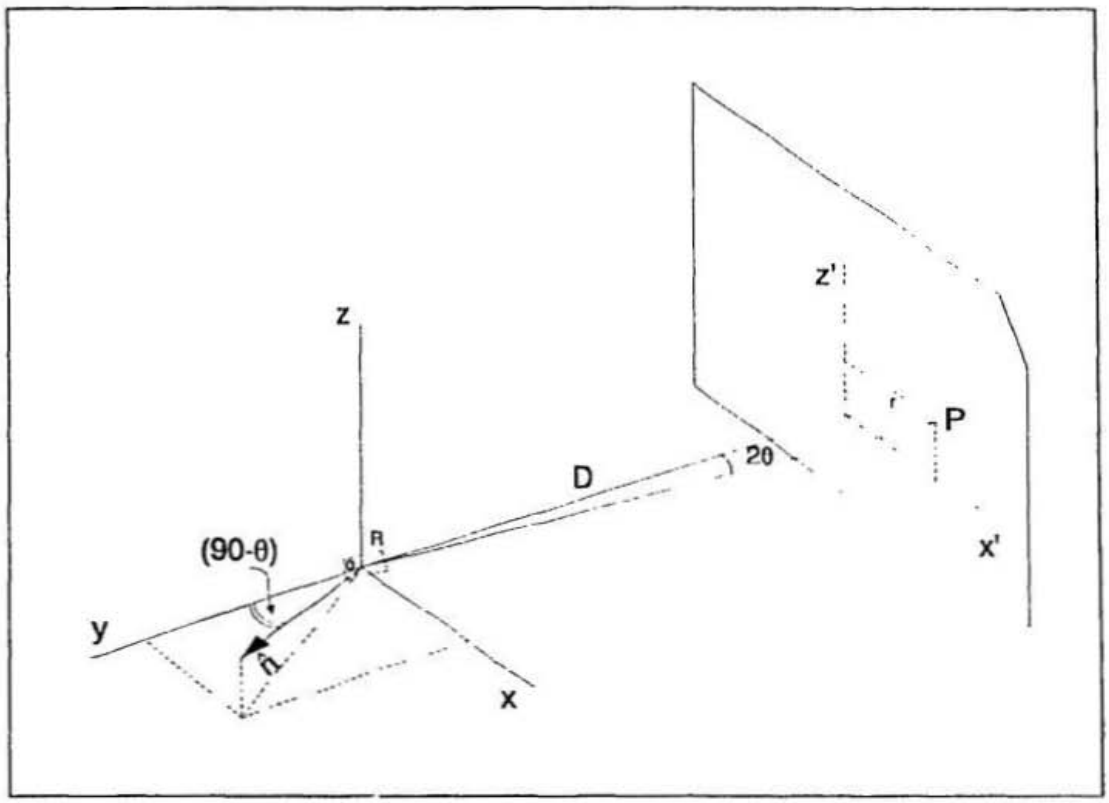

Figure 4.2: Schematic diagram of the X-ray diffraction geometry. (x,y,z) is the laboratory coordinate frame. The X-rays were incident along the y-axis, R is the reflecting plane with normal $\hat{n}$, P is the Laue spot with coordinates (x',z'), and 2θ is the angle of diffraction.

The computerized orientation procedure was developed by Gannon[44]. The input for the program consists of the Laue spot coordinates, the structure matrix of the crystal, and a specified maximum error for calculating interplanar angles. From the coordinates of the first three Laue spots (which must not lie in the same crystallographic

zone), the direction cosines of the normals to the corresponding planes are calculated using the equations of stereographic projection[60]. The three interplanar angles are then calculated using the dot product of the normal vectors. From a generated Miller indices list, three Miller indices are chosen as normal vectors of three Bragg planes. The direction cosines of the interplanar angles are then calculated and compared with those found earlier from the method of stereographic projection. If all three are within the input tolerance, then the rotation matrix R, and hence a set of Euler angles can be calculated by applying the method of least squares to the orientation equation[61],

$$\begin{pmatrix} X \\ Y \\ Z \end{pmatrix} = S R^{-1} Q^{-1} \begin{pmatrix} h \\ k \\ l \end{pmatrix} \quad . \tag{4.1}$$

In the above equation (X,Y,Z) are the direction cosines in the lab frame, (h,k,l) are the Miller indices of the plane producing the Laue spot, S is the interplanar spacing of the {hkl} planes, Q is the structure matrix, and R is the rotation matrix expressed in terms of the Euler angles[60].

These Euler angles are then used to assign Miller indices to the remaining spots and give a calculated set of cartesian coordinates (x'_{cal}, z'_{cal}). This is basically a procedure which produces a number of possible sets of Euler angles within the experimental tolerance. Only those with an average cartesian coordinate difference of < 1 mm are kept for a least squares fitting program which determines the correct set of angles.

By rotating the cryostat another Laue photograph is taken. This corresponds to a change in the ϕ angle while θ and χ are held fixed. By using one of the Euler angle sets from the first program (with the ϕ angle changed appropriately) and the Laue coordinates from this photograph, a least squares fitting program calculates a finer set of angles and an average cartesian coordinate difference. The input and output angles are specified to be within ± 1°. If this produces more than one set of angles

within the desired tolerance, the procedure is repeated with a third photograph taken at another cryostat angle. Once a consistent orientation is determined, the least squares fitting program is run on all remaining orientations. In cases where the cell is not set exactly perpendicular to the optic axis, this also takes care of any wobbling effects when the cryostat is rotated. A sample Laue photograph is shown in figure (4.4) along with a schematic diagram showing the Bragg planes and best fit Euler angles. In the orientation procedure, Euler angles were determined for seven different orientations by varying ϕ over a 60° range in 10° intervals.

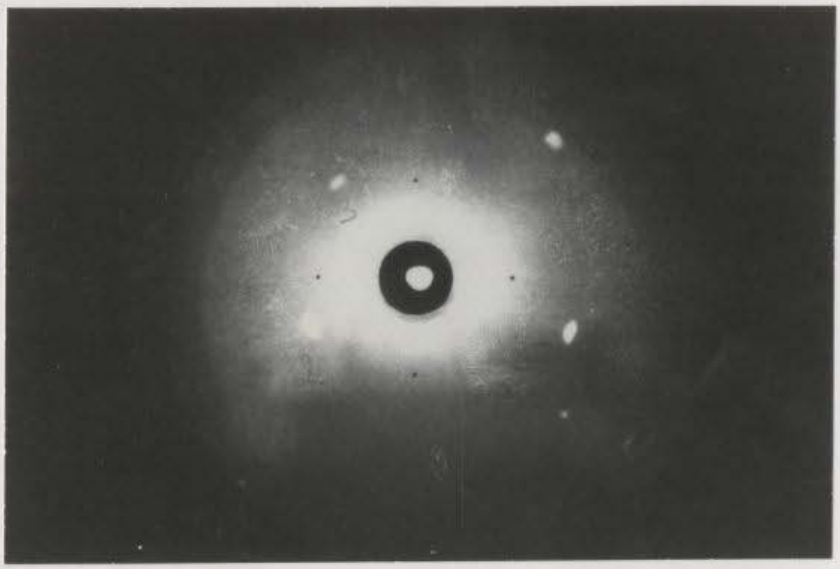

θ=113.6, ϕ=275.4, χ=196.9

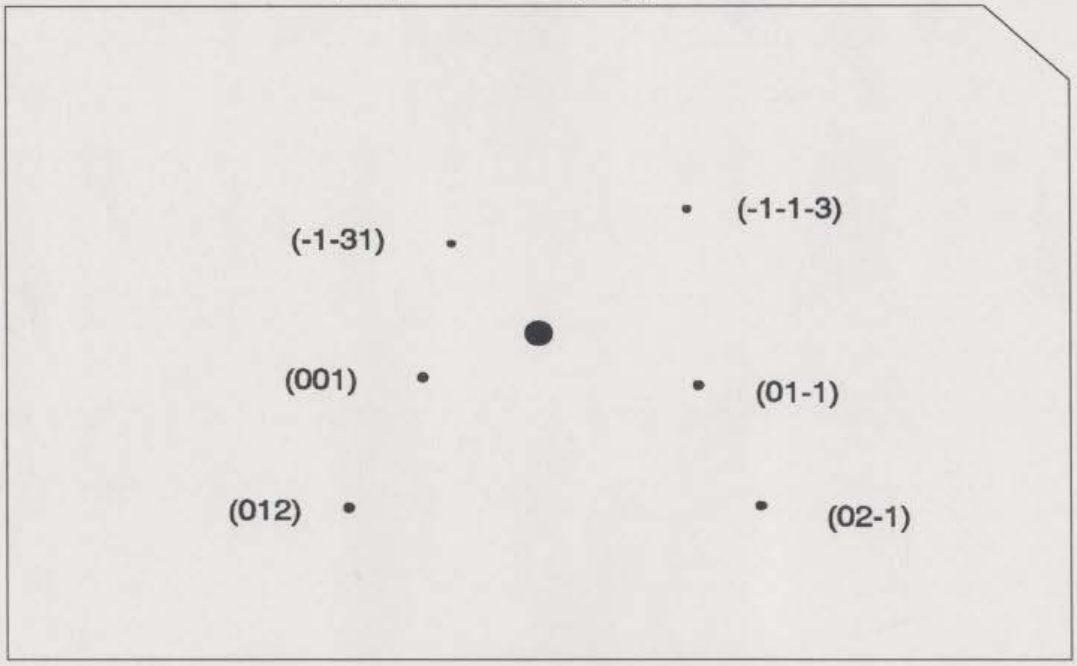

Figure 4.3: Sample Laue diffraction photograph of crystal #7 at T=60 K. Below the photo is a schematic diagram of the Laue spots showing the Miller indices of the Bragg planes causing the interference. The best fit Euler angles are also given.

4.3 OPTICAL ALIGNMENT

The optical alignment is most crucial if high finesse and contrast are to be obtained from the Brillouin spectrometer. The optical components of the spectrometer are placed on a track mounted on a large steel table which is rubber mounted and loaded with bricks to eliminate vibration. With reference to figure (3.1), the alignment begins by passing the He-Ne beam through the pinholes A3 and A4 into the photomultiplier tube. The Fabry-Perot is then placed on the table perpendicular to He-Ne beam. With the Fabry-Perot in its single pass mode, the horizontal and vertical levelling screws are adjusted until the beam passes through the centre of the front and rear apertures. By adjusting the three fine micrometre screws at the front, the mirrors are made parallel to each other and perpendicular to the optic axis by backreflecting the He-Ne beam. The focusing lens L2 is then put in place and adjusted to cause backreflection of the beam and send a parallel beam through the FP. The lens L3 is then adjusted so that the exit beam from the FP passes through A4 in both single and triple pass modes. Once these rough adjustments are made with the He-Ne, a card is placed at the intersection of both laser beams. The DAS-1 is used to observe the scattering of the argon beam from the card with the FP in single pass mode. The mirrors of the FP are aligned more precisely using first the three micrometre screws, then using the PZT bias controls on the DAS-1. The lens L2 is then adjusted (without the pinhole A4) to maximize the signal. With the FP switched to triple pass, the lens L2 and the bias controls are adjusted once more. Finally the pinhole A4 is put in place and the lens L3 is adjusted to maximize the signal received by the phototube.

4.4 BRILLOUIN SPECTRA ANALYSIS

At each orientation the respective Brillouin Spectra are recorded by the DAS-I. As stated in section (3.1) the CRT screen displays the channel number and the corresponding photon counts in each channel alphanumerically. Because of the linear relationship between channel number and frequency, the frequency of a specific Brillouin component is calculated by measuring the number of channels between itself and the unshifted laser line.

A stick diagram of a typical CH_4 spectrum is shown in figure (4.4). The DAS-I displays two complete FP orders consisting of three Rayleigh peaks, and four sets of Brillouin components. Two different SFR's are used in this experiment (16.43 GHz and 18.27 GHz), both of which cause an overlap between the down-shifted (longitudinal) component of one order, with the up-shifted (longitudinal) component of the next order. There is no overlap between longitudinal and transverse components.

With reference to figure (4.4), using the cursor of the DAS-I, the channel number and corresponding photon counts of the central components R_i and the Brillouin components L_i, T_i^s, and T_i^f are recorded. From these measurements four values for the free spectral range SFR_i $(i = 1-4)$, and four values for each Brillouin component ΔL_i, ΔT_i^s, ΔT_i^f $(i = 1-4)$ are calculated in channel number. Then from the value of the free spectral range given in terms of frequency, SFR_{GHz}=16.43 GHz or 18.27 GHz, the frequencies of the various Brillouin components are calculated as follows

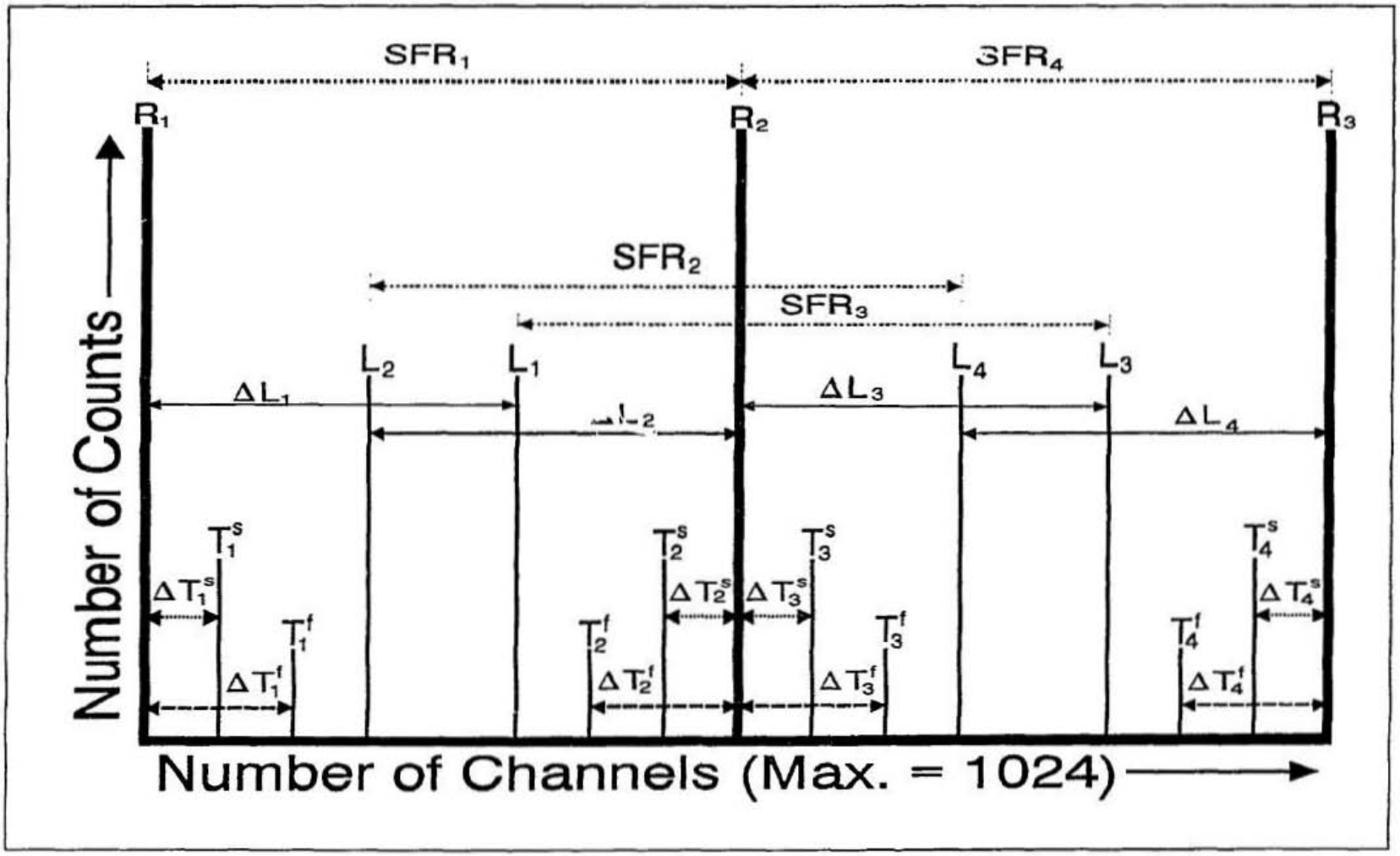

Figure 4.4: Stick diagram of a typical CH_4 spectrum showing the various frequency shifts. The R_i are the central Rayleigh components, the L_i, T_i^s, and T_i^f are the longitudinal, slow transverse, and fast transverse components, respectively. The SFR_i are the free spectral ranges, the ΔL_i, ΔT_i^s and ΔT_i^f are the frequency shifts of the L_i, T_i^s, and T_i^f components.

$$\nu(L) = \frac{SFR_{GHz}}{4} \sum_{i=1}^{4} \frac{L_i}{SFR_i}$$

$$\nu(T^s) = \frac{SFR_{GHz}}{4} \sum_{i=1}^{4} \frac{T_i^s}{SFR_i} \qquad (4.2)$$

$$\nu(T^f) = \frac{SFR_{GHz}}{4} \sum_{i=1}^{4} \frac{T_i^f}{SFR_i} \quad .$$

This averaging process is used to compensate for the non-linearity of the ramp voltage used to scan the Fabry-Perot interferometer. This causes a discrepancy of about 1% in the number of channels between the successive orders on the CRT screen, and consequently a channel number difference between the four shift measurements of a specific Brillouin component.

4.5 *Determination of Elastic Constants and Pockel Coefficients*

The elastic constants and Pockel's coefficients are obtained from a least squares fitting procedure based upon Newton's fixed point method. The input for the program consists of three initial values of the elastic constants C_{11}, C_{12}, and C_{44}, the crystal orientations specified by the Euler angles and the corresponding measured Brillouin shifts ν_k^{obs}. Using the trial elastic constants, the λ_{ij}'s are calculated from equation (2.13) and used to diagonalize the matrix (2.12). The matrix diagonals give three eigenvalue solutions $\rho\omega_\mu^2$ from which the frequencies of the three acoustic modes are calculated. These frequencies are labelled $\nu_k^{calc}(C_{ij})$. The best fit elastic constants are obtained by minimizing the difference between the observed and calculated frequencies using a least squares fitting procedure. The term, minimized with respect to the variation

in the elastic constants, is χ^2 and is defined by

$$\chi^2 = \frac{1}{N-3}\sum_{k=1}^{N}\left(\frac{v_k^{calc}(C_{ij}) - v_k^{obs}}{\sigma_k}\right)^2 \quad . \tag{4.3}$$

Here N is the total number of measured Brillouin components, N-3 is the number of degrees of freedom, and σ_k is a weighting factor which represents the average standard deviation in the measured frequency shifts. Increasing the weighting factor increases the relative fitting errors of the elastic constants. The errors quoted in chapter 5 are based on the criterion that $\chi^2 = 1$ when the standard deviation σ_k was a maximum. Similarly, with respect to equation (2.25), the Pockel's coefficient ratios are determined from the measured intensity ratios.

Chapter 5:

Experimental Results and Discussion

5.1 Results for CH_4-I and CH_4-II

The present experiment marks the first determination (using single crystal data) of the temperature dependence of the elastic constants across the I-II phase transition in CH_4. The Brillouin scattering data for CH_4 have been compiled in tables (5.1) to (5.11). Brillouin spectra were recorded from 7 different crystals and at 12 different temperatures ranging from 72.8 K to 15.5 K. The data from crystals #1, #2, and #3 were recorded in a previous investigation by V. Askarpour and the present author[53] at temperatures 72.8 K, 50.9 K, 38.5 K, and 25.0 K. The previous lower temperature data have been reanalysed here along with the current data.

The instrumental linewidths were typically ~300 MHz. The central component was usually $\sim 10^4$-10^5 times greater than the longitudinal components; this was very much dependent on the crystal quality and the optical alignment. Most CH_4 spectra recorded in this laboratory encountered an overlap problem between the longitudinal component of one order with the fast transverse of the next order. Consequently, the SFR of the FP was increased to 18.27 GHz and used to record the spectrum of crystal #7. The

strongest Brillouin spectra were recorded at the triple point (90.4 K): a typical spectrum at this temperature would run for 2 hours, in which case the longitudinal component would accumulate ~800-1000 photon counts. As the temperature of the crystal was decreased, so did the strength of the Brillouin spectra. A CH_4 Brillouin spectrum recorded at 17.5 K is shown in figure (5.1): a typical spectrum at this temperature would be recorded for ~24 hours and the resulting longitudinal components would accumulate ~500-800 photon counts.

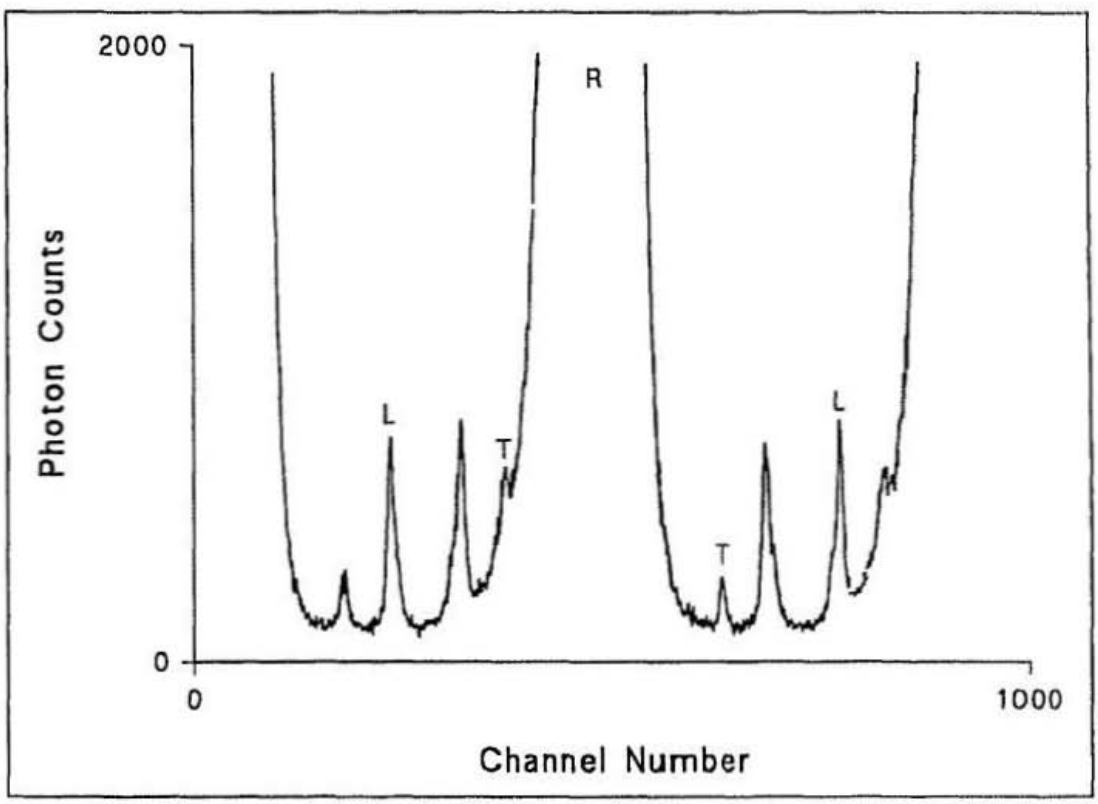

Figure 5.1: Brillouin spectrum of crystal #7 recorded at T = 17.5 K. Only two components are visible, the longitudinal L and the slow transverse T belonging to the central Rayleigh component R.

EULER ANGLES (°)			OBSERVED (GHz)			CALCULATED (GHz)			OBSERVED		CALCULATED	
θ	φ	χ	ν_L	ν_{T_2}	ν_{T_1}	ν_L	ν_{T_2}	ν_{T_1}	I_{T_2}/I_L	I_{T_1}/I_L	I_{T_2}/I_L	I_{T_1}/I_L
*Crystal #1**												
98.0	287.6	269.1	9.22	5.46	-	9.203	5.410	3.099	0.036	-	0.020	0.015
98.0	277.6	269.1	9.19	-	-	9.177	5.491	3.031	-	-	0.006	0.002
98.0	267.6	269.1	9.20	-	-	9.222	5.388	3.082	-	-	0.021	0.002
98.0	257.6	269.1	9.31	5.21	-	9.322	5.120	3.233	0.068	-	0.055	0.004
98.0	247.6	269.1	9.44	4.83	-	9.434	4.754	3.460	0.111	-	0.072	0.011
98.0	237.6	269.1	9.47	4.45	-	9.513	4.381	3.724	0.045	-	0.046	0.036
98.0	227.6	269.1	9.51	-	3.88	9.533	4.258	3.816	-	0.111	0.013	0.052
*Crystal #2**												
40.8	51.8	38.9	9.24	-	3.86	9.232	4.855	3.805	-	0.130	0.001	0.183
40.8	42.7	38.2	9.03	-	4.04	9.034	5.025	4.088	-	0.222	0.005	0.218
40.1	32.9	38.4	8.80	-	4.35	8.758	5.217	4.433	-	0.206	0.007	0.213
40.3	22.9	38.4	8.41	-	4.73	8.451	5.384	4.813	-	0.169	0.005	0.167
39.8	12.6	39.0	8.22	-	5.14	8.175	5.483	5.164	-	0.062	0.002	0.094
39.8	2.6	39.0	8.02	-	5.37	8.028	5.478	5.395	-	0.063	0.006	0.036
39.8	352.6	39.0	8.04	-	5.36	8.078	5.490	5.308	-	0.052	0.003	0.054
*Crystal #3**												
117.5	333.6	61.2	8.46	-	4.78	8.484	5.352	4.790	-	0.175	0.006	0.174
117.5	323.6	61.2	8.22	-	5.11	8.214	5.469	5.117	-	0.053	0.003	0.100
117.1	313.4	61.1	8.22	-	5.34	8.062	5.483	5.339	-	0.048	0.005	0.049
116.4	304.3	6..5	8.22	-	5.35	8.095	5.481	5.291	-	0.049	0.005	0.062
117.6	294.6	61.9	8.21	-	5.04	8.285	5.464	5.007	-	0.063	0.003	0.124
116.1	285.5	61.9	8.49	-	4.68	8.512	5.375	4.714	-	0.173	0.008	0.171
116.1	275.5	61.9	8.78	-	4.40	8.800	5.194	4.377	-	0.191	0.010	0.214
Crystal #4												
106.0	269.3	224.5	8.22	-	5.05	8.248	5.491	5.038	-	0.205	0.000	0.146
106.0	259.3	224.5	8.58	-	4.42	8.552	5.486	4.508	-	0.261	0.000	0.253
106.2	249.4	224.6	8.85	-	3.90	8.832	5.485	3.933	-	0.237	0.000	0.281
106.1	239.5	224.7	9.01	-	3.45	9.034	5.490	3.436	-	0.189	0.000	0.195
105.6	230.2	224.8	9.12	5.48	3.17	9.141	5.490	3.141	-	0.083	0.001	0.073
106.1	219.3	224.1	9.18	-	-	9.188	5.465	3.046	-	-	0.002	0.021
105.8	209.4	224.2	9.15	5.35	3.13	9.169	5.392	3.229	-	0.125	0.005	0.104

Table 5.1: Brillouin scattering data for CH_4-I at 72.8 K.

*Data from crystals #1, #2, and #3 were compiled in a previous investigation by R. Kelly and V. Askarpour[58]

EULER ANGLES (°)			OBSERVED (GHz)			CALCULATED (GHz)			OBSERVED		CALCULATED	
θ	ϕ	χ	ν_L	ν_{T_2}	ν_{T_1}	ν_L	ν_{T_2}	ν_{T_1}	I_{T_2}/I_L	I_{T_1}/I_L	I_{T_2}/I_L	I_{T_1}/I_L
Crystal #1												
98.0	287.6	269.1	9.68	5.85	-	9.800	5.829	3.492	0.094		0.017	0.016
98.0	277.6	269.1	9.64	-	-	9.773	5.913	3.426			0.028	0.020
98.0	267.6	269.1	9.67	5.65	-	9.819	5.807	3.476	0.071		0.015	0.002
98.0	257.6	269.1	9.80	5.49	-	9.923	5.532	3.625	0.106		0.086	0.006
98.0	247.6	269.1	9.90	5.18	-	10.010	5.157	3.850	0.115		0.112	0.018
98.0	237.6	269.1	10.00	4.72	-	10.123	4.777	4.111	0.066		0.088	0.019
98.0	227.6	269.1	10.03	4.62		10.143	4.653	4.206	0.055		0.051	0.069
Crystal #2												
40.8	51.8	38.9	9.97	-	4.22	9.829	5.291	4.197		0.200	0.083	0.171
40.8	42.7	38.2	9.74	-	4.45	9.622	5.434	4.183		0.243	0.087	0.211
40.3	32.9	38.4	9.51	-	4.74	9.335	5.632	4.833		0.218	0.110	0.216
40.3	22.9	38.4	9.17	-	5.12	9.016	5.804	5.220		0.231	0.087	0.178
39.8	12.6	39.0	8.85	-	5.52	8.731	5.901	5.579		0.141	0.089	0.106
39.8	2.6	39.0	8.66	-	5.77	8.579	5.900	5.815		0.077	0.023	0.029
39.8	352.6	39.0	8.58	5.94	-	8.630	5.912	5.726	0.053		0.061	0.013
Crystal #3												
117.5	333.6	61.2	9.08	-	5.29	9.051	5.710	5.196		0.185	0.010	0.181
117.5	323.6	61.2	8.79	-	5.65	8.771	5.891	5.540	-	0.130	0.010	0.110
117.1	313.4	61.1	8.54	5.87	-	8.614	5.904	5.758	0.093		0.053	0.022
116.4	304.3	61.5	8.67	-	5.78	8.618	5.902	5.708		0.071	0.022	0.068
117.6	294.6	61.9	8.87	-	5.48	8.844	5.885	5.418		0.141	0.010	0.134
116.3	285.5	61.9	9.15	-	5.15	9.080	5.793	5.119		0.177	0.013	0.177
116.3	275.5	61.9	9.46	-	4.80	9.379	5.607	4.776		0.239	0.015	0.215
Crystal #5												
137.9	70.3	274.0	10.06	5.28	3.88	10.019	5.201	3.845			0.024	0.002
136.5	59.5	273.0	9.94	-	3.83	9.875	5.487	3.821		0.034	0.015	0.017
137. .	48.9	272.2	9.81	-	3.92	9.696	5.655	4.029		0.120	0.007	0.147
137.1	40.5	272.7	9.53	-	4.34	9.463	5.769	4.404		0.212	0.003	0.248
136.7	31.0	272.7	9.16	-	4.86	9.167	5.851	4.849		0.263	0.091	0.266
137.2	19.6	270.7	8.77	-	5.50	8.889	5.886	5.344		0.166	0.000	0.200
137.9	10.8	271.0	8.47	-	5.85	8.638	5.894	5.732		0.061	0.002	0.068

Table 5.2: Brillouin scattering data for CH_4-I at 50.9 K.

EULER ANGLES (°)			OBSERVED (GHz)			CALCULATED (GHz)			OBSERVED		CALCULATED	
θ	φ	χ	ν_L	ν_{T_2}	ν_{T_1}	ν_L	ν_{T_2}	ν_{T_1}	I_{T_2}/I_L	I_{T_1}/I_L	I_{T_2}/I_L	I_{T_1}/I_L
Crystal #3'												
117.5	333.6	61.2	9.37	-	5.57	9.376	6.247	5.625	-	0.230	0.018	0.216
117.5	323.6	61.2	9.06		5.92	9.066	6.373	5.830	-	0.154	0.025	0.137
117.1	313.4	61.1	8.95		6.24	8.889	6.387	6.225	-	0.176	0.047	0.061
116.4	303.3	61.5	8.97		6.17	8.928	6.385	6.172	-	0.157	0.046	0.080
117.6	293.6	61.9	9.16		-	9.147	6.368	5.861	-	0.153	0.024	0.163
116.3	285.5	61.9	9.51	-	-	9.407	6.271	5.545	-	0.225	0.025	0.210
116.3	275.5	61.9	9.81		-	9.731	6.078	5.190	-	0.202	0.021	0.246

Table 5.3: Brillouin scattering data for CH_4-I at 38.5 K.

EULER ANGLES (°)			OBSERVED (GHz)			CALCULATED (GHz)			OBSERVED		CALCULATED	
θ	φ	χ	ν_L	ν_{T_2}	ν_{T_1}	ν_L	ν_{T_2}	ν_{T_1}	I_{T_2}/I_L	I_{T_1}/I_L	I_{T_2}/I_L	I_{T_1}/I_L
Crystal #5												
139.9	70.3	274.0	10.53	-	4.34	10.560	4.322	-	-	0.018	0.030	0.018
136.5	59.5	273.0	10.36	-	4.31	10.401	4.292	-	-	0.057	0.018	0.056
137.3	48.9	272.2	10.24	-	4.42	10.205	4.500	-	-	0.228	0.008	0.204
137.1	40.5	272.7	9.97	-	4.81	9.950	4.884	-	-	0.315	0.003	0.347
136.7	31.0	272.7	9.63	-	5.39	9.622	5.398	-	-	0.551	0.001	0.383
137.2	19.6	270.7	9.36	-	5.79	9.310	5.878	-	-	0.243	0.000	0.300
137.9	10.8	271.0	9.03	-	6.26	9.019	6.306	-	-	0.109	0.036	0.057

Table 5.4: Brillouin scattering data for CH_4-I at 30.0 K.

EULER ANGLES (°)			OBSERVED (GHz)			CALCULATED (GHz)			OBSERVED		CALCULATED	
θ	ϕ	χ	ν_L	ν_{T_2}	ν_{T_1}	ν_L	ν_{T_2}	ν_{T_1}	I_{T_2}/I_L	I_{T_1}/I_L	I_{T_2}/I_L	I_{T_1}/I_L
Crystal #5												
117.5	333.6	61.2	9.57		5.81	9.618	6.125	5.742		0.306	0.013	0.229
117.5	323.6	61.2	9.23	-	6.17	9.282	6.561	6.129			0.015	0.141
117.1	313.4	61.1	9.12	-	6.23	9.008	6.576	6.397		0.121	0.031	0.072
116.4	304.3	61.5	9.13	-	6.40	9.131	6.574	6.338		0.111	0.031	0.090
117.6	294.6	61.9	9.37	-	6.03	9.371	6.555	5.999		0.263	0.011	0.173
116.3	285.5	61.9	9.69	-	5.53	9.651	6.451	5.651		0.317	0.017	0.223
116.3	275.5	61.9	10.07	-	5.29	10.000	6.241	5.271		0.273	0.018	0.260
Crystal #7												
113.6	295.4	196.9	10.29	6.55	4.21	10.283	6.586	4.200	0.025	0.130	0.031	0.119
113.6	285.4	196.9	10.22	-	4.50	10.223	6.496	4.479		0.203	0.038	0.178
113.6	275.4	196.9	10.24	-	4.72	10.259	6.259	4.728		0.295	0.056	0.221
113.8	265.8	197.1	10.40	5.97	4.83	10.361	5.999	4.838	0.015	0.381	0.040	0.282
113.6	257.0	197.3	10.58	-	4.69	10.479	5.901	4.701		0.296	0.011	0.298
113.8	247.0	196.8	10.60	-	4.31	10.608	5.918	4.382		0.177	0.003	0.194
113.9	237.4	197.1	10.64	-	4.18	10.658	6.001	4.139		0.082	0.003	0.059
113.7	227.1	197.0	10.64	-	-	10.639	6.041	4.129			0.002	0.050
113.6	215.4	196.9	10.53	-	-	10.500	6.073	4.431		0.156	0.003	0.221

Table 5.5: Brillouin scattering data for CH_4-I at 25.0 K.

EULER ANGLES (°)			OBSERVED (GHz)			CALCULATED (GHz)			OBSERVED		CALCULATED	
θ	ϕ	χ	ν_L	ν_{T_2}	ν_{T_1}	ν_L	ν_{T_2}	ν_{T_1}	I_{T_2}/I_L	I_{T_1}/I_L	I_{T_2}/I_L	I_{T_1}/I_L
Crystal #7												
113.6	285.4	196.9	10.27	6.47	4.54	10.301	6.531	4.510	0.022	0.182	0.024	0.166
113.6	275.4	196.9	10.34	6.31	4.75	10.340	6.293	4.760	0.032	0.242	0.040	0.208
113.8	265.8	197.1	10.47	6.08	4.85	10.442	6.033	4.871	0.023	0.291	0.026	0.258
113.6	257.0	197.3	10.61	-	4.65	10.560	5.937	4.733		0.249	0.004	0.263
113.8	247.0	196.8	1.69	-	4.37	10.690	5.952	4.442		0.165	0.002	0.158
113.9	237.4	197. .	10.74	-	4.18	10.740	6.037	4.168		0.044	0.004	0.036
113.7	227.1	197.0	10.69	-	4.24	10.721	6.078	4.158			0.004	0.029

Table 5.6: Brillouin scattering data for CH_4-I at 23.0 K.

EULER ANGLES (°)			OBSERVED (GHz)			CALCULATED (GHz)			OBSERVED		CALCULATED	
θ	ϕ	χ	ν_L	ν_{T_2}	ν_{T_1}	ν_L	ν_{T_2}	ν_{T_1}	I_{T_2}/I_L	I_{T_1}/I_L	I_{T_2}/I_L	I_{T_1}/I_L
Crystal #7												
113.6	285.4	196.9	10.32	6.53	4.51	10.323	6.571	4.534	0.026	0.195	0.026	0.1[illegible]
113.6	275.4	196.9	10.38	6.38	4.84	10.359	6.331	4.786	0.040	0.220	0.048	0.238
113.8	265.8	197.1	10.48	-	4.88	10.463	6.070	4.897	-	0.323	0.035	0.305
113.6	257.0	197.3	10.59	-	4.73	10.582	5.973	4.759	-	0.277	0.006	0.323
113.8	247.0	196.8	10.71	-	4.44	10.713	5.988	4.437	-	0.229	0.000	0.203
113.9	237.4	197.1	10.75		-	10.762	6.074	4.193	-	-	0.001	0.041
113.7	227.1	197.0	10.73	-	-	10.743	6.115	4.182	-	-	0.001	0.024

Table 5.7: Brillouin scattering data for CH_4-I at 21.5 K.

EULER ANGLES (°)			OBSERVED (GHz)			CALCULATED (GHz)			OBSERVED		CALCULATED	
θ	ϕ	χ	ν_L	ν_{T_2}	ν_{T_1}	ν_L	ν_{T_2}	ν_{T_1}	I_{T_2}/I_L	I_{T_1}/I_L	I_{T_2}/I_L	I_{T_1}/I_L
Crystal #7												
113.6	285.4	196.9	10.31	-	4.65	10.348	6.575	4.570	-	0.209	0.012	0.171
113.6	275.4	196.9	10.38	6.33	4.81	10.383	6.338	4.818	0.028	0.193	0.031	0.209
113.8	265.8	197.1	10.54	6.10	4.92	10.486	6.079	4.928	0.022	0.290	0.022	0.257
113.6	257.0	197.3	10.65	-	4.71	10.603	5.984	4.791	-	0.299	0.003	0.261
113.8	247.0	196.8	10.71	-	4.46	10.733	5.999	4.473	-	0.152	0.002	0.157
113.9	237.4	197.1	10.78	-	-	10.783	6.084	4.232	-	-	0.004	0.035
113.7	227.1	197.0	10.73	-	-	10.764	6.124	4.222	-	-	0.003	0.026

Table 5.8: Brillouin scattering data for CH_4-I at 20.5 K.

EULER ANGLES (°)			OBSERVED (GHz)			CALCULATED (GHz)			OBSERVED		CALCULATED	
θ	ϕ	χ	ν_L	ν_{T_2}	ν_{T_1}	ν_L	ν_{T_2}	ν_{T_1}	I_{T_2}/I_L	I_{T_1}/I_L	I_{T_2}/I_L	I_{T_1}/I_L
Crystal #7												
113.8	265.8	197.1	10.68	6.34	5.19	10.682	6.354	5.197	0.007	0.216	0.023	0.220
113.6	257.0	197.3	10.83	-	5.04	10.801	6.258	5.064		0.267	0.006	0.214
113.8	247.0	196.8	10.96	6.39	4.78	10.933	6.273	4.754	0.006	0.150	0.006	0.126
113.9	237.4	197.1	11.02	-	-	10.983	6.358	4.520			0.008	0.038
113.7	227.1	197.0	10.87	-	-	10.961	6.398	4.510			0.007	0.047

Table 5.9: Brillouin scattering data for CH_4-II at 19.5 K.

EULER ANGLES (°)			OBSERVED (GHz)			CALCULATED (GHz)			OBSERVED		CALCULATED	
θ	ϕ	χ	ν_L	ν_{T_2}	ν_{T_1}	ν_L	ν_{T_2}	ν_{T_1}	I_{T_2}/I_L	I_{T_1}/I_L	I_{T_2}/I_L	I_{T_1}/I_L
Crystal #7												
113.6	285.4	196.9	10.56	-	4.94	10.617	6.903	4.940		0.203	0.034	0.133
113.6	275.4	196.9	10.64	6.66	5.17	10.653	6.668	5.178	0.036	0.149	0.016	0.161
113.8	265.8	197.1	10.81	-	5.27	10.757	6.413	5.283		0.211	0.033	0.198
113.6	257.0	197.3	10.90	-	5.19	10.876	6.319	5.152		0.272	0.014	0.197
113.8	247.0	196.8	10.98	-	4.83	11.007	6.334	4.848		0.137	0.011	0.129
113.9	237.4	197.1	10.07	-		11.056	6.418	4.619			0.010	0.061
113.7	227.1	197.0	11.04	-	-	11.037	6.457	4.609			0.009	0.063

Table 5.10: Brillouin scattering data for CH_4-II at 17.5 K.

EULER ANGLES (°)			OBSERVED (GHz)			CALCULATED (GHz)			OBSERVED		CALCULATED	
θ	ϕ	χ	ν_L	ν_{T_2}	ν_{T_1}	ν_L	ν_{T_2}	ν_{T_1}	I_{T_2}/I_L	I_{T_1}/I_L	I_{T_2}/I_L	I_{T_1}/I_L
Crystal #7												
113.6	285.4	196.9	10.68	-	5.00	10.710	6.994	4.999		0.141	0.044	0.147
113.6	275.4	196.9	10.73	6.74	5.26	10.747	6.756	5.240	0.048	0.189	0.048	0.187
113.8	265.8	197.1	10.87	6.50	5.33	10.853	6.497	5.347	0.072	0.220	0.033	0.233
113.6	257.0	197.3	11.00	-	5.24	10.974	6.402	5.215	-	0.215	0.010	0.237
113.8	247.0	196.8	11.13	-	4.90	11.106	6.416	4.908		0.142	0.005	0.148
113.9	237.4	197.1	11.18	-	4.66	11.157	6.501	4.676		0.043	0.006	0.051
113.7	227.1	197.0	11.10	-	4.68	11.137	6.541	4.666		0.048	0.005	0.048

Table 5.11: Brillouin scattering data for CH_4-II at 15.5 K.

Determination of the elastic constants requires a knowledge of the density and refractive index at each temperature. The density data were taken from an X-ray investigation by Prokhvatilov et. al.[88]. The value of the refractive index at the triple point is well known[64], namely, $n_{tr}(90.4\ K) = 1.323$, $\rho_{tr}(90.4) = 0.4874\ g/cm^3$. These values for density and refractive index were used along with the Lorentz relation[52]:

$$\frac{(n_x^2-1)}{(n_x^2+2)} = \frac{\rho_x}{\rho_{tr}} \frac{(n_{tr}^2-1)}{(n_{tr}^2+2)} \tag{5.1}$$

to calculate the refractive indices found in Table (5.12). The previous investigation[53] assumed a linear relationship between density and temperature from 90.4 K to 25.0 K; this proved to be incorrect[88]. From the measured data, the elastic constants were calculated at the temperatures listed in Table (5.12) using the method described in section (4.8). The elastic constants, the bulk modulus and the shear modulus are plotted versus temperature in figures (5.2) to (5.8). The elastic constants at the triple point (90.4 K) were also determined in this laboratory and were found to be in good agreement with the previous determinations of Rand and Stoicheff[63].

To normalize χ^2, the values of the standard deviation σ_k ranged from 0.02 GHz to 0.08 GHz. In addition to the quoted uncertainties in table (5.12), there is a possible systematic error of ≈ 1% due the uncertainties in the values of density, refractive index, and scattering angle. This is also reflected in the values of B and G. Much of the fitting error, C_{12} being particularly sensitive, is caused by the inability to obtain spectra containing both transverse modes. This can be seen from the measured intensity ratios in tables (5.1) to (5.11): while one transverse (usually the slow T_1 mode) is very strong, the other is very weak. Only in crystal #7, where the SFR was changed from 16.43 GHz to 18.27 GHz, were both transverse components observed consistently at each orientation. This partly accounts for the inconsistencies (usually within experimental error) in C_{12} in the low temperature region, especially at 30.0 K. The effects of spin conversion in CH_4 are also called into question here. Measurements of the spin lattice

relaxation time[33] have shown that the effects of nuclear spin conversion usually come into play at ~30 K and are dependent on the cooling and equilibration history of the molecule. Maintaining a consistent thermal history between all crystals is a problem in the present experiment because the cooling and timing procedure is not always the same, and as a result the thermal history of each crystal is very different.

Temperature K	Refractive Index	Density g/cm^3	C_{11} kbar	C_{12} kbar	C_{44} kbar	A	B kbar	G kbar
Phase I								
90.4[33]	1.323	.4875	19.57 ± 0.30	14.46 ± 0.20	9.20 ± 0.15	3.60	16.16	5.53
72.8	1.333	0.5018	23.64 ± 0.09	16.80 ± 0.10	11.27 ± 0.06	3.30	19.08	7.00
50.9	1.341	0.5136	27.33 ± 0.18	18.48 ±0.20	13.22 ± 0.12	2.99	21.43	8.53
38.5	1.346	0.5183	29.13 ± 0.17	19.10 ± 0.24	15.51 ± 0.13	3.09	21.61	9.88
30.0	1.348	0.5213	30.12 ± 0.17	18.74 ± 0.60	15.71 ± 0.41	2.76	22.15	10.46
25.0	1.348	0.5228	30.47 ± 0.14	19.49 ± 0.15	16.52 ± 0.10	3.01	23.15	10.63
23.0	1.349	0.5234	31.02 ± 0.23	19.88 ± 0.19	16.69 ± 0.13	3.00	23.59	10.76
21.5	1.350	0.5241	31.03 ± 0.19	19.77 ± 0.15	16.90 ± 0.12	3.00	23.52	10.89
20.5	1.350	0.5248	31.39 ± 0.30	19.83 ± 0.23	16.93 ± 0.19	2.93	23.68	11.01
Phase II								
19.5	1.353	0.5282	32.51 ± 0.42	19.09 ± 0.29	18.40 ± 0.24	2.71	23.56	12.29
17.5	1.353	0.5288	33.27 ± 0.27	19.13 ± 0.21	18.69 ± 0.19	2.61	23.81	12.67
15.5	1.354	0.5294	33.78 ± 0.15	19.28 ±0.12	19.21 ± 0.10	2.65	24.11	13.00

Table 5.12: Temperature dependent elastic constant data for single crystals of CH_4-I and CH_4-II.

Using the intensity ratios, the Pockel's coefficient ratios and estimated values of the Pockel's coefficients are calculated as outlined in section (4.8). They are listed in table (5.14) along with the estimated errors. Unlike the accuracy of the frequency measurements, the intensity measurements are estimated to be good to only

about 10-20%. The fitting procedure was carried out using the fcc lattice configuration in both phase I and phase II.

Laue X-ray photographs taken in both phases showed no structural change across the transition which is consistent with the previous structural determination[18]. The density calculations, which were carried out in both phases, have also showed a slight increase from phase I to phase II, this is common to most order-disorder transitions (where there is no structural change).

Temperature K	$\frac{P_{12}}{P_{11}}$	$\frac{P_{44}}{P_{11}}$	P_{11}	P_{12}	P_{44}
Phase I					
90.4[a]	1.031 ± 0.035	0.069 ± 0.010	0.23	0.23	0.016
72.8	1.132 ± 0.076	0.074 ± 0.026	0.28	0.32	0.021
50.9	1.016 ± 0.062	0.148 ± 0.009	0.31	0.31	0.046
38.5	0.787 ± 0.340	0.183 ± 0.048	0.37	0.29	0.067
30.0	0.938 ± 0.038	0.233 ± 0.020	0.33	0.31	0.077
25.0	0.958 ± 0.086	0.176 ± 0.017	0.32	0.31	0.057
23.0	1.005 ± 0.050	0.138 ± 0.008	0.32	0.32	0.043
21.5	1.107 ± 0.070	0.158 ± 0.014	0.29	0.33	0.046
20.5	1.230 ± 0.190	0.068 ± 0.088	0.27	0.34	0.019
Phase II					
19.5	0.922 ± 0.113	0.130 ± 0.019	0.33	0.31	0.043
17.5	0.842 ± 0.080	0.145 ± 0.018	0.35	0.30	0.051
15.5	0.912 ± 0.034	0.159 ± 0.012	0.34	0.31	0.053

Table 5.13: Temperature dependence of the Pockel's coefficients for CH_4-I and CH_4-II single crystals.

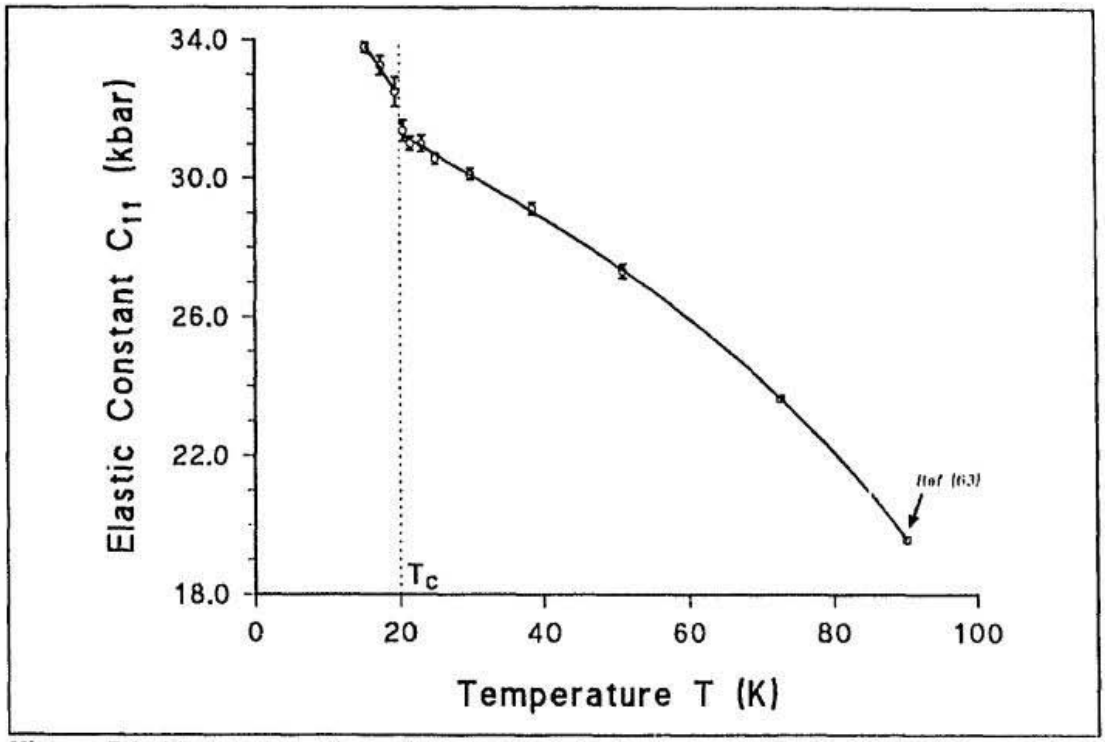

Figure 5.2: Temperature dependence of the elastic constant C_{11} in CH_4 single crystals.

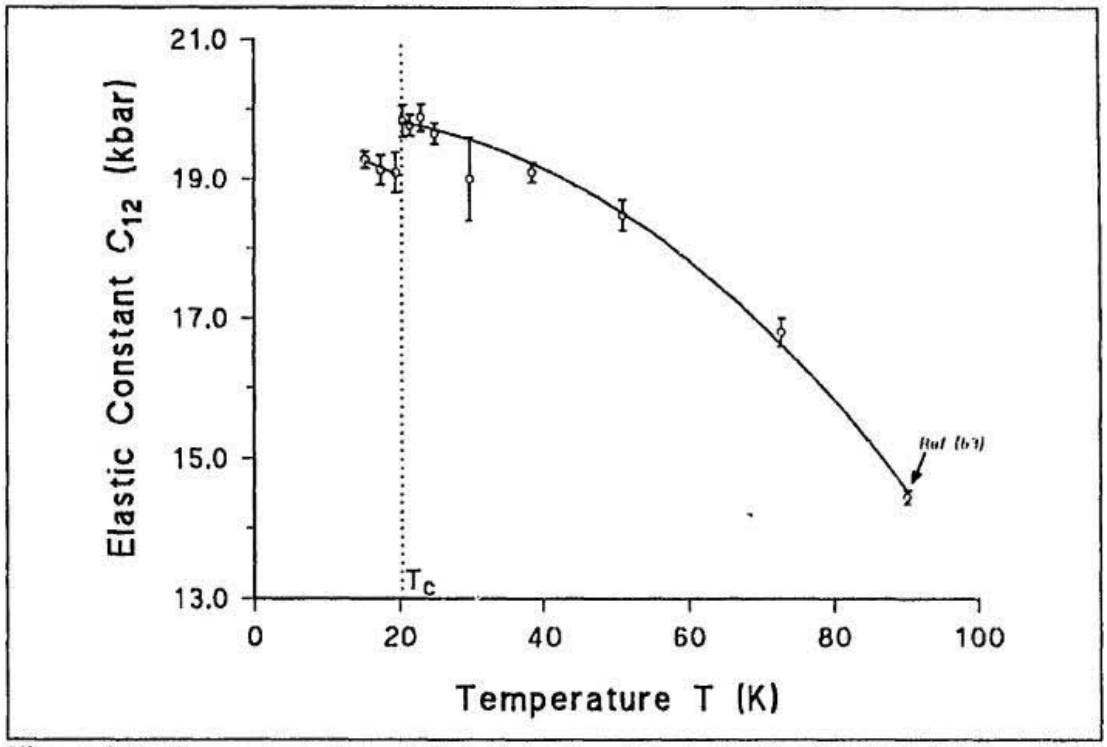

Figure 5.3: Temperature dependence of the elastic constant C_{12} for CH_4 single crystals.

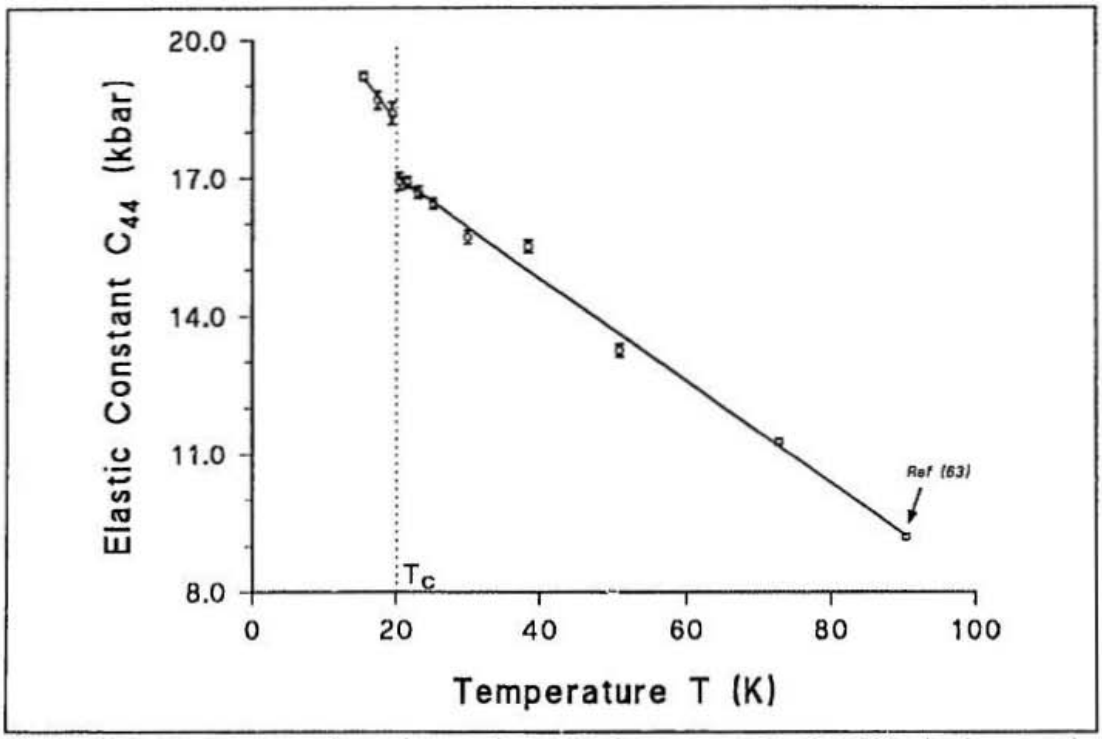

Figure 5.4: Temperature dependence of the elastic constant C_{44} for CH_4 single crystals.

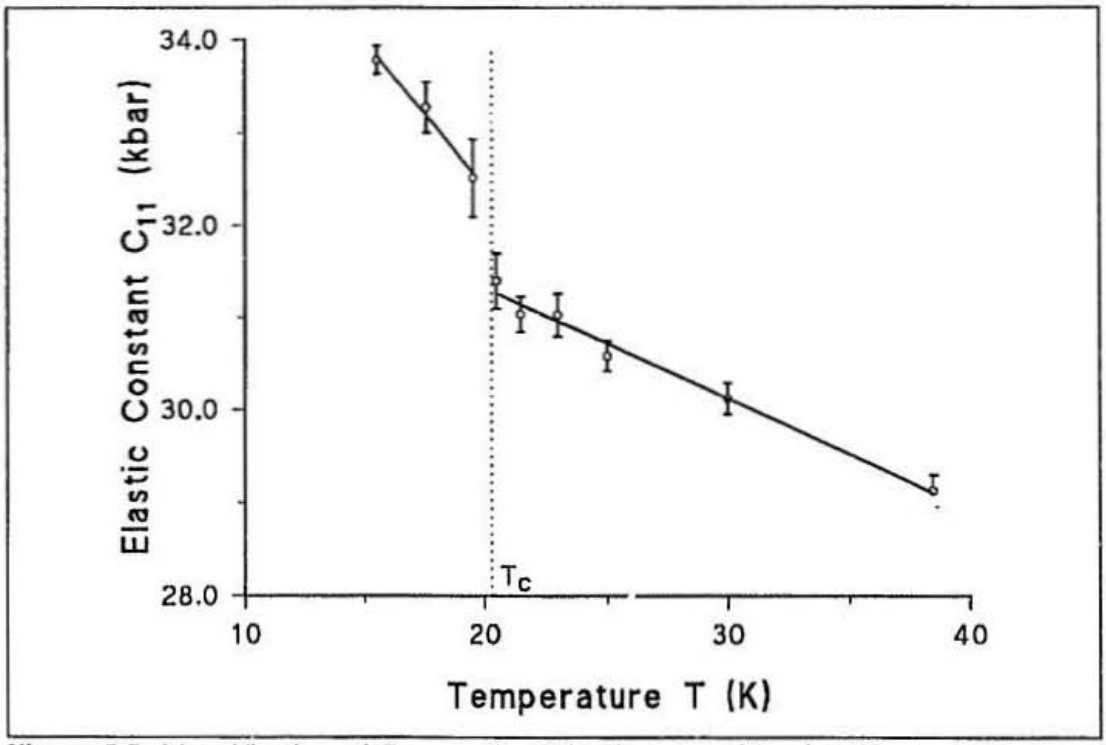

Figure 5.5: Magnification of C_{11} near the O-D phase transition in CH_4.

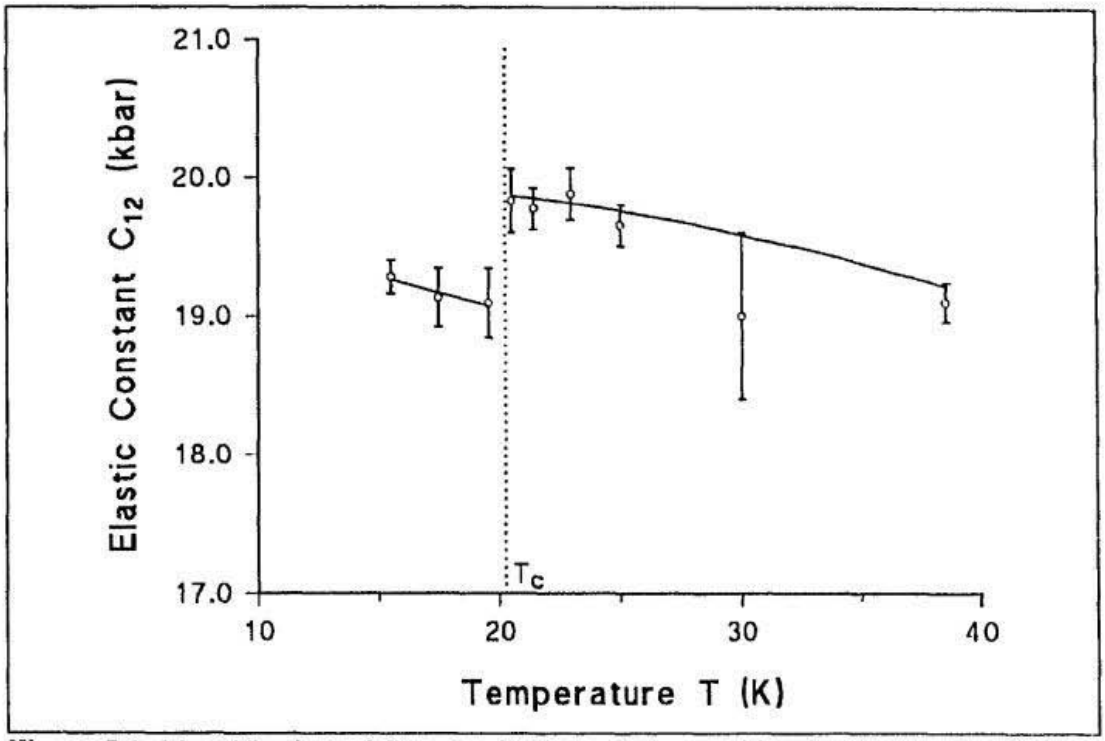

Figure 5.6: Magnification of C_{12} near the O-D phase transition in CH_4.

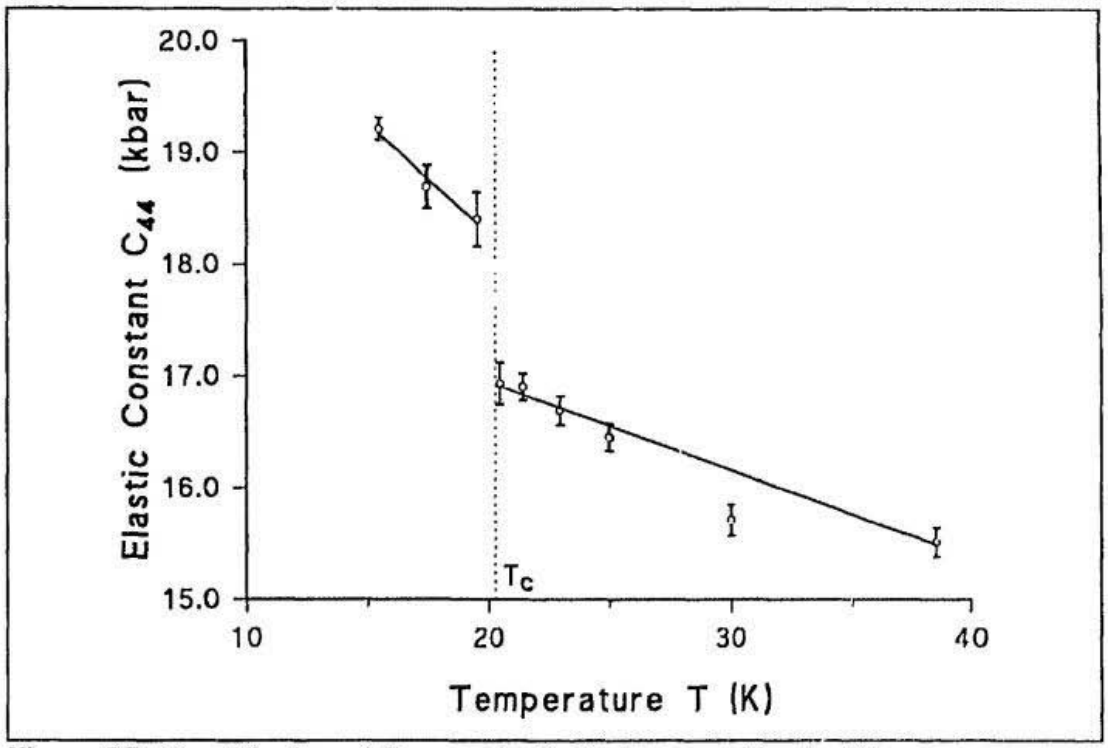

Figure 5.7: Magnification of C_{44} near the O-D phase transition in CH_4.

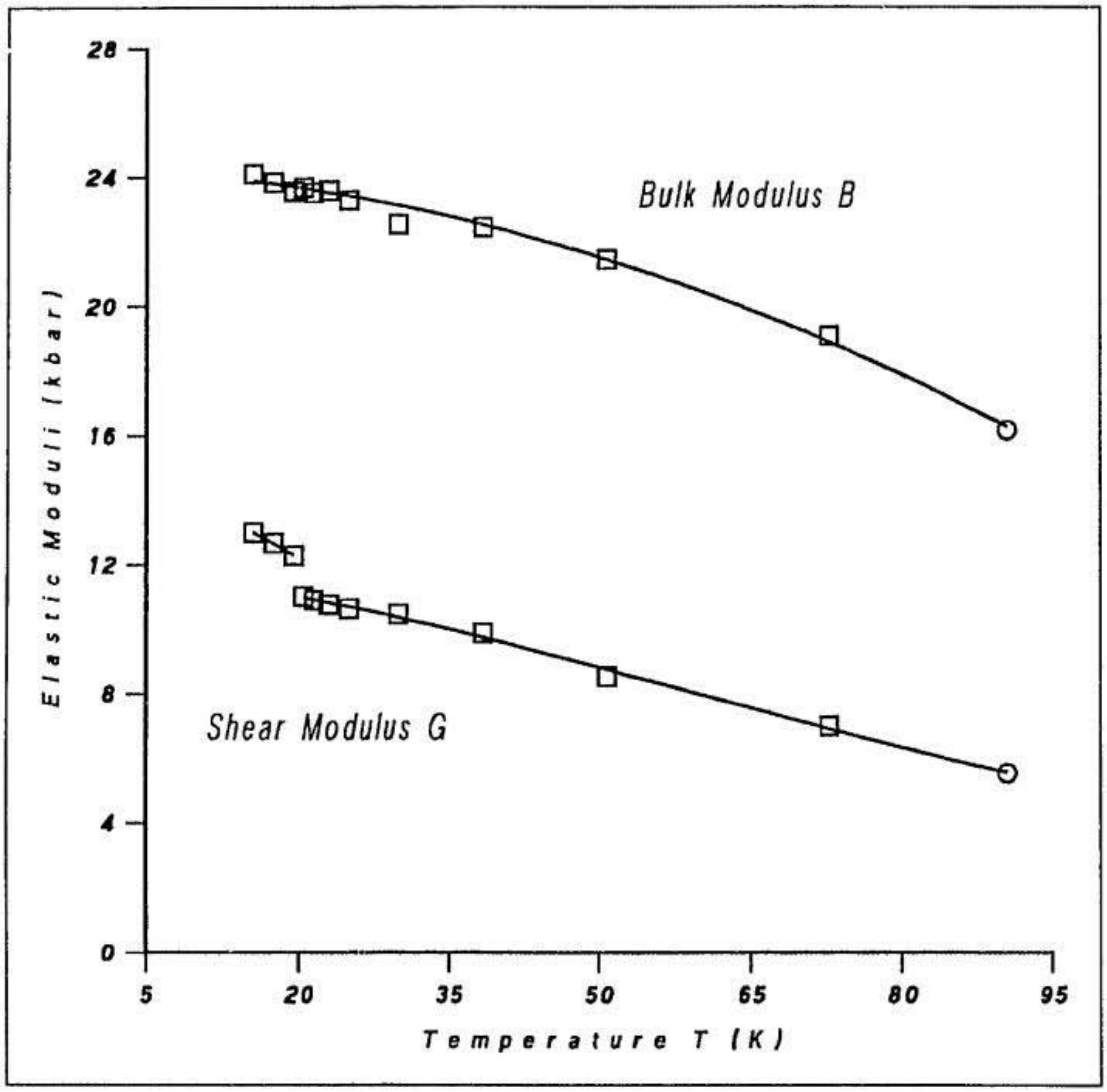

Figure 5.8: Temperature dependence of the elastic moduli for single crystals of CH_4. The triple point data at 90.4 K were compiled by Rand et al.[63].

5.2 RT Coupling and the O-D Phase Transition in CH_4

The rotation-translation interaction is known to be a major contributor to the intermolecular potential of both CH_4 and CD_4. Bounds et al.[61] performed the first molecular dynamics simulation on CD_4 in which the intermolecular potential was assumed to be of the atom-atom type neglecting any coupling between translational and rotational motion. Their calculated elastic constants proved to be much smaller than the experimental values found by Rand and Stoicheff[63]. This led to the conclusion that their calculated crystal was too soft, such that the intermolecular potential was too weak. As discussed in section (3.4), Wonneberger and Huller[40] later performed another molecular dynamics calculation using the classical mean field approach of Michel and Naudts[65,67]. Their calculations were based on an interaction potential composed of centre of mass translations and rotations of the CD_4 tetrahedra. Using such a model they were able to predict elastic constants in good agreement with Rand and Stoicheff. The theoretical and experimental elastic constants of CH_4 and CD_4 have been tabulated in Table (5.14).

	Calculated Uncoupled[65]	Calculated Uncoupled[59]	Calculated Coupled[59]	Measured[63]
C_{11}	16.4	26.0	20.97	20.04
C_{12}	13.6	13.82	15.22	15.00
C_{44}	6.0	13.82	11.52	9.15

Table 5.14: Comparison of the theoretical (using coupled and uncoupled potentials) and the experimental elastic constants near the triple point.

While the classical approach is strictly not valid for describing the molecular rotations in CH_4, the theory of section (2.4) is quite useful in analyzing the variations of the elastic constants. According to equations (2.61), a decrease in RT coupling results in an increase in C_{11} and C_{44}, but a decrease in C_{12}. As the temperature is lowered through the I- II phase transition in CH_4, the rotational motion of 3 out of 4 molecules is frozen out. Therefore, if phase II is assumed to be a state involving weak RT coupling and phase I strong RT coupling, then the elastic constant changes shown in Figures (5.2) to (5.7) are in quantitative agreement with the dynamical equations (2.61). C_{12} starts to level off at 25 K and then drops sharply at the phase transition temperature (20.4 K) indicative of the softening of the slow transverse phonon in the <110> direction.

The bulk modulus is given by equation (2.9). In the region near the transition temperature, the bulk modulus exhibits no anomalous behaviour (within experimental error) between Phase I and Phase II, thus the crystal does not undergo any large bulk changes such as a structural deformation, or large density change. Wonneberger and Huller[49], however, predict (equations 2.61) that the bulk modulus should increase through the phase transition as $8W_3^2 - 3W_1^2$. With respect to the present results, this implies that $8W_3^2 = 3W_1^2$. Substitution back into the equation for C_{12} (equation 2.62c) gives $|\Delta C_{12}| = \frac{1}{2}|\Delta C_{11}|$. This, in fact, is in reasonable qualitative agreement with the data of table (5.12) and figures (5.2) and (5.3) where $|\Delta C_{11}| = 1.12$ (kbar) and $|\Delta C_{12}| = 0.74$ (kbar).

For single crystal measurements of the elastic constants, the shear modulus is also given by equations (2.9). The shear modulus, on the other hand, is observed to increase sharply from phase I to Phase II (figure 5.8). From polycrystalline sound velocity measurements, it is known that the shear modulus is given by $G = \rho V_T^2$, where ρ is the density and V_T is the average transverse sound velocity. The anomalous behaviour of the shear modulus clearly indicates that the rotational motion of the CH_4

tetrahedron is coupled more strongly to the transverse acoustic phonons.

Within experimental error the Pockel's coefficient ratios showed no significant changes across the phase transition. This is consistent with the small density and volume changes which accompany the transition.

To further the analysis of the elastic constants near the phase transition the acoustic velocities in high symmetry directions are introduced. The velocity of the longitudinal and transverse modes in the <100>, <110>, and <111> directions are derived from equation (2.13) and are shown below. Using these equations the high symmetry acoustic velocity ratios are calculated in table (5.16). The sudden sharp decrease in velocity ratios from 90.4 K to 72.8 K is indicative of rapid crystal hardening. From 72.8 K the acoustic ratios show little change until the phase transition is reached.

<100> direction

$$V_L = \left[\frac{C_{11}}{\rho}\right]^{\frac{1}{2}}, \qquad V_{T_1,T_2} = \left[\frac{C_{44}}{\rho}\right]^{\frac{1}{2}} \tag{5.1}$$

<110> direction

$$V_L = \left[\frac{C_{11}+C_{12}+2C_{44}}{2\rho}\right]^{\frac{1}{2}}, \qquad V_{T_1} = \left[\frac{C_{44}}{\rho}\right]^{\frac{1}{2}}, \qquad V_{T_2} = \left[\frac{C_{11}-C_{12}}{2\rho}\right]^{\frac{1}{2}} \tag{5.2}$$

<111> direction

$$V_L = \left[\frac{C_{11}+2C_{12}+4C_{44}}{3\rho}\right]^{\frac{1}{2}}, \qquad V_{T_1,T_2} = \left[\frac{C_{11}-C_{12}+C_{44}}{3\rho}\right]^{\frac{1}{2}} \tag{5.3}$$

Temperature	<100> $V_l/V_{tr,12}$	<110> V_l/V_{tr}	<110> V_l/V_{tr}	<111> $V_l/V_{tr,12}$
90.4[64]	1.47	1.70	3.23	2.46
72.8	1.33	1.54	2.51	2.10
50.9	1.33	1.55	2.52	2.11
38.5	1.37	1.60	2.56	2.13
30.0	1.38	1.60	2.65	2.19
25.0	1.36	1.59	2.71	2.24
23.0	1.36	1.58	2.70	2.20
21.5	1.36	1.58	2.74	2.22
20.5	1.36	1.59	2.75	2.22
19.5	1.37	1.59	2.65	2.18
17.5	1.44	1.64	2.84	2.30
15.5	1.43	1.67	3.03	2.38

Table 5.15: Temperature dependence of the ratios of acoustic velocities in high symmetry directions for CH_4-I and CH_4-II.

Experimental Comparisons

The elastic constants of methane (both CH_4 and CD_4) have been determined by several other experimental and theoretical techniques and they are summarized in table (5.16). It is evident that much more work has been done on the deuterated species. CD_4 is more suitable for neutron scattering, it does not experience the problem of spin conversion and the molecular rotations can be treated classically. With respect to CD_4, the results of Marx et al.[82] (Schaefer-Bergman) and Rand et al.[61] (Brillouin scattering) are in good agreement; Marx's values are slightly higher but they were recorded at a lower temperature. The neutron scattering results of Stirling et al.[98] and Press et al.[121] in phase I of CD_4 (at 32.5 K and 34.5 K) are in agreement with the present results on CH_4. While this similarity is interesting it is important to realize that the neutron scattering data have quoted errors of greater than 10%. Also shown in table (5.16) are

the theoretical Born-von Kármán calculations of Stirling et al.[98] for CD_4, and the

REFERENCE	METHOD	SUBSTANCE	TEMP.	C_{11} (kbar)	
Marx et al. (1984)[82]	Schaefer-Bergmann	CD_4	85.57 K	20.56 ± 0.15	
Rand et al. (1982)[63]	Brillouin Scattering	CD_4	89.2 K	20.04 ± 0.3	
Stirling et al. (1977)[98]	Neutron Scattering	CD_4	32.5 K	30.8 ± 2.0	
Press et al. (1977)[127]	Neutron Scattering	CD	34.5 K	32.8 ± 1.6	
Stirling et al. (1977)[98]	Born-von-Kármán	CD_4	32.5 K	34.1	
Stirling et al. (1977)	Leonard-Jones	CD_4	32.5 K	30.7	
Rand et al. (1982)[63]	Brillouin Scattering	CH_4	90.4 K	19.57 ± 0.30	
Bounds et al. (1980)[64]	Molecular dynamics	CH_4	91.2 K	16.4 ± 1.0	
Wonneberger et al. (1987)[49]	Molecular dynamics	CD_4	86.0 K	20.97	

Table 5.16: Comparison of various experimental and theoretical values of the elastic constants in methane.

molecular dynamics calculations of Bounds et al.[64] and Wonneberger et al.[49]. Stirling's calculations are a fit to his neutron scattering data. They assumed that the methane intermolecular potential was a central harmonic interaction. His resulting theoretical values are 10-25% higher than the experimental determinations. As stated earlier, the intermolecular potential used in Bound's calculation was also based on atom-atom potentials with no rotation-translation interaction, and this accounts for his low values for the elastic constants.

Along with the single crystal data there have been three ultrasound velocity measurements in polycrystalline samples. The first measurements of Bezuglyi et al.[128] were reported in the temperature range 4.2 K to 77 K; the actual measurements were made, however, between 64 K and 77 K and 14.4 K to 21.4 K while the values from 21.4 K to 64 K were interpolated. The ultrasound data of Wolf et al.[123] were determined in the range 2-77 K. In these experiments, sound velocity measurements were made while the sample was warming up at a rate of 6 K/hr. Equilibrium sound velocity measurements in phase I were made by Tarasenko et al.[129]

For a comparison of the sound velocity data with those of Brillouin scattering, it is necessary to convert them to a common form. Consequently the temperature dependence of the bulk and shear modulus for CH_4 are plotted in figure (5.9), while the corresponding graph for CD_4 is given in figure (5.10). Mars et al.[82] have noted that the equilibrium values of Tarasenko are probably the most accurate. The results of the present investigation confirm this in that the shear modulus values of the present work are in remarkably good agreement with those of Tarasenko; it is difficult to distinguish between the two curves in figure (5.8). The bulk modulus values of Tarasenko are also in good agreement down to 50 K, at which point his curve levels off while the curve of the present work continues to increase. The elastic moduli of Bezuglyi et al. and Wolf et al. do not agree as well with the present work. When considering the conditions under

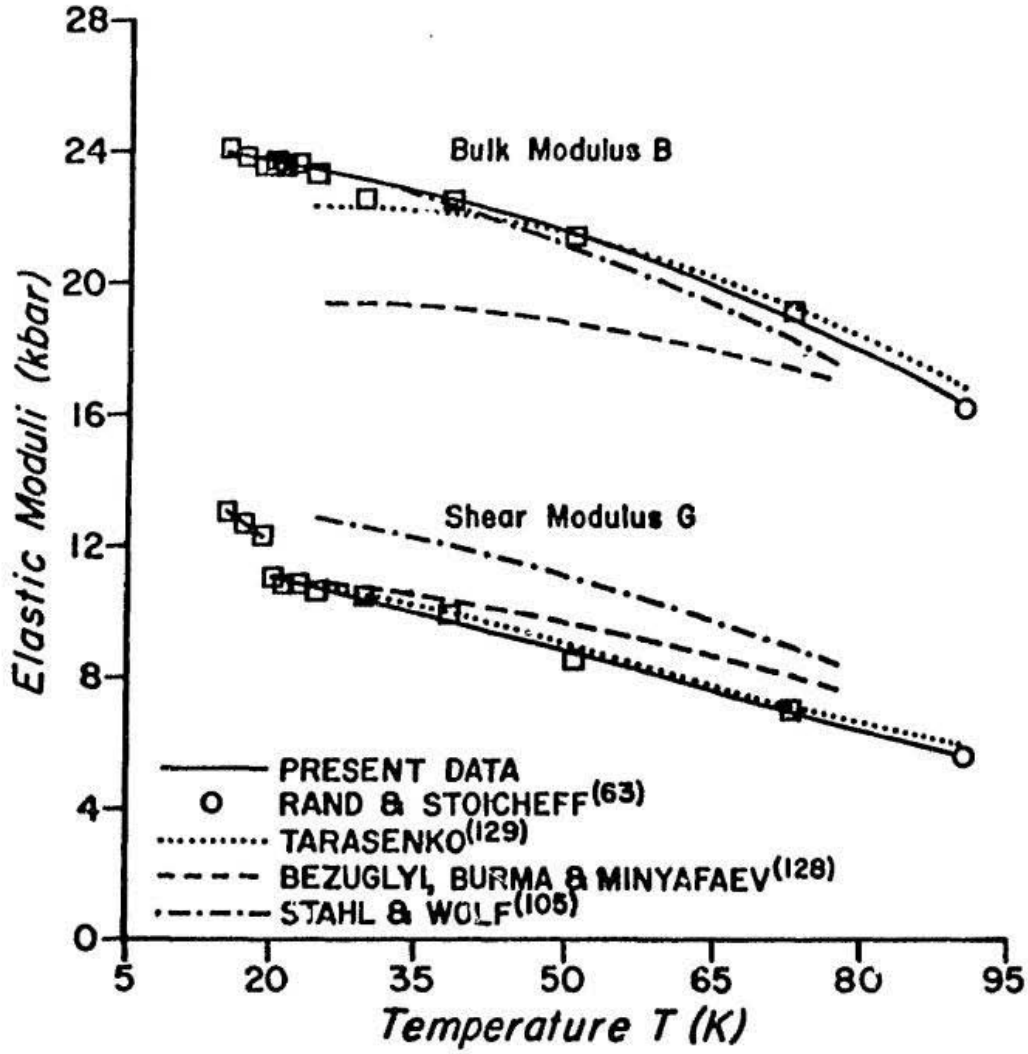

Figure 5.9: Comparison of the temperature dependence of the elastic moduli of solid CH_4 using both single and polycrystal data.

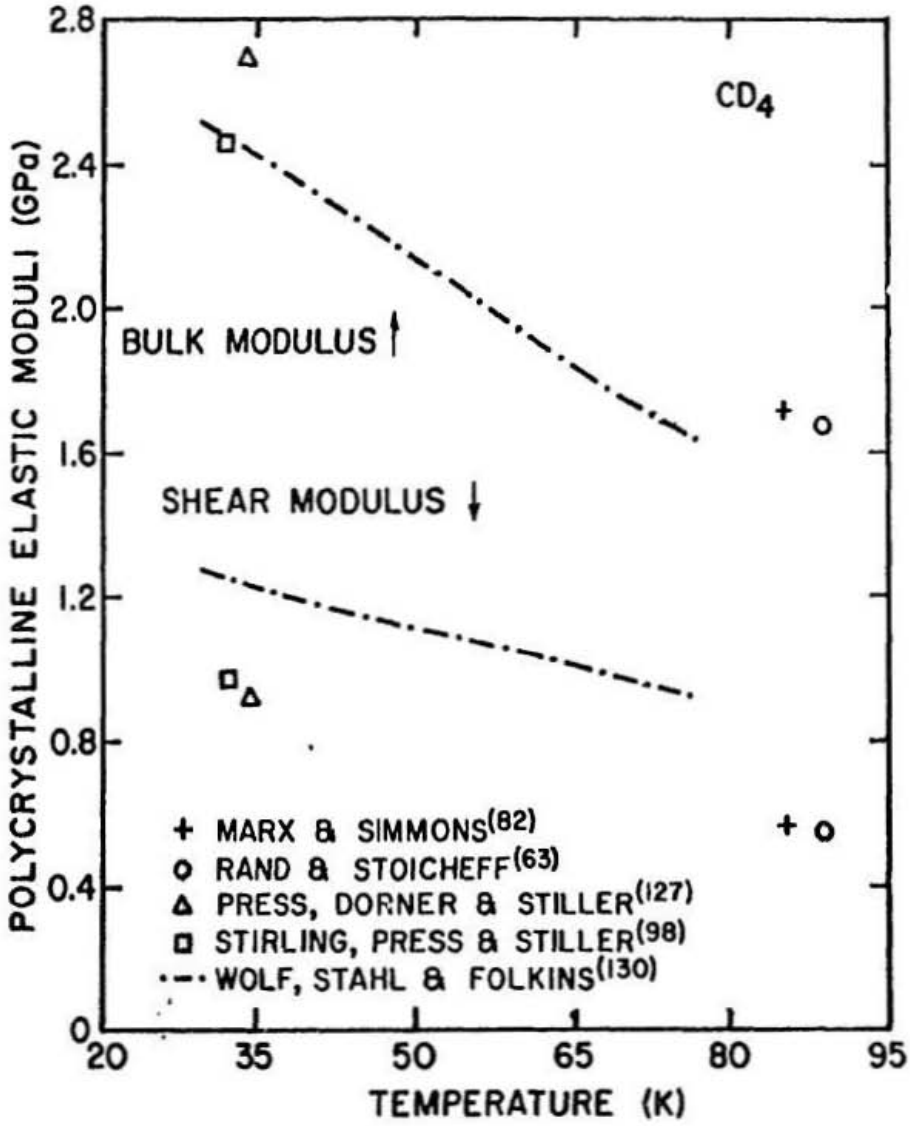

Figure 5.10: Comparison of the temperature dependence of the elastic moduli of solid CD_4 using both single and polycrystal data.

which these data were obtained the discrepancies are not surprising. The shear modulus values of Bezuglyi et al. and the bulk modulus values of Wolf et al., however, do show some quantitative agreement with the present results especially in the region below 40 K. In phase I, the bulk and shear modulus in CD_4 (figure 5.9) are also quite similar to their counterparts in CH_4. The ultrasonic results of Wolf, Stahl and Folkins[130], as for their CH_4 results, were recorded while the sample was warming, and would probably account for the discrepancy between the Brillouin scattering[63] and the Schaefer-Bergmann method[82]. A comparison of figures (5.9) and (5.10) reveals that the present moduli determinations in CH_4 agree quite well with the low temperature neutron scattering results[98][121]. This is somewhat surprising when considering the differences in their moments of inertia and hence the differences in their rotational energies.

5.3 *Methane, and the Rare Gas solids*

Because of their simplicity, the rare gas solids (RGS) were among the first molecular crystals to be studied by Brillouin spectroscopy. CH_4, because of its spherical rotational symmetry, tight internal bonding, and spherical electron probability distribution, also exhibits characteristics similar to of the RGS. The present investigation provides an opportunity for comparing the elastic constant temperature dependence in CH_4 with those of the RGS. The elastic constants, anisotropy factor A, and Cauchy parameter δ of CH_4 and the rare gas solids are listed in table (5.17). There is, however, little experimental low temperature data on the RGS.

From a comparison of the elastic constants at the triple point, CH_4 most closely resembles argon. This is not surprising when comparing the similarities in the molecular weight, diameter, and depth of the potential well. At the triple point, however, it does have a much larger anisotropy, and a larger Cauchy parameter.

	C_{11}	C_{12}	C_{44}	A	δ
CD_4 (89.2 K)[66]	20.04	15.00	9.15	3.64	-0.39
CH_4 (90.4 K)[66]	19.57	14.46	9.20	3.60	-0.36
CH_4 (72.8 K) Present Work	23.64	16.80	11.27	3.30	-0.33
CH_4 (50.9 K) Present Work	27.33	18.48	13.22	2.99	-0.28
CH_4 (38.5 K) Present Work	29.06	17.93	15.50	2.79	0.14
CH_4 (25.0 K) Present Work	30.47	19.49	16.52	3.01	0.15
CH_4 (20.5 K) Present Work	31.39	19.83	16.93	2.93	-0.15
CH_4 (19.5 K) Present Work	32.51	19.09	18.40	2.74	-0.04
CH_4 (17.5 K) Present Work	33.27	19.13	18.69	2.64	-0.02
CH_4 (15.5 K) Present Work	33.78	19.28	19.21	2.65	0.00
Neon (24.3 K)[132]	11.70	7.31	6.02	2.74	-0.18
Krypton (82.3 K)[132]	26.57	17.25	12.61	2.71	0.27
Xenon (156 K)[132]	29.80	19.00	14.80	2.74	0.22
Argon (82.3 K)[132]	23.80	15.60	11.20	2.73	0.28
Argon (25.0 K)[133]-Theoretical	38.10	18.70	18.80	1.94	0.01
Argon (10.0 K)[135]	42.10	22.70	21.70	2.24	-0.04
Argon (7.0 K)[134]-Theoretical	39.70	19.20	20.00	1.95	0.04

Table 5.17: Elastic Data for CH_4, CD_4, and the rare gas solids. The theoretical values for low temperature argon are derived from a Lennard-Jones potential[133][134].

The larger Cauchy parameter can be interpreted as an indication of the stronger coupling of the rotational and translational modes in CH_4. In CH_4-I the anisotropy factor A is about 30% higher. Following the phase transition (at 19.5 K) A drops to 2.74, within the range of the RGS. This is not surprising considering the decrease in molecular rotation in phase II of CH_4 and hence the rotational coupling of the CH_4 tetrahedron to the acoustic phonon modes. Comparison of the Cauchy relation of CH_4-II with the Cauchy relation in argon at low temperatures show that in both cases the Cauchy relation is essentially satisfied (i.e. $\delta \sim 0$). The values of C_{12} and C_{44} in argon, at 25 K, 10 K and 7 K, are quite similar to the values of C_{12} and C_{44} found in CH_4-II at 15.5 K. This implies that the character of the crystalline field in CH_4 has become less orientational and more central in nature, which is consistent with the decreased rotation motion of the CH_4

molecules in phase II.

5.4 *Concluding Remarks*

In this investigation a temperature dependent Brillouin scattering study, particularly emphasizing the I-II phase transition, in CH_4 has been completed in an attempt to determine the variations of the elastic constants as related to the effects of RT coupling. Acoustic anomalies have been found in all three elastic constants across the phase transition, and are consistent with the theoretical predictions of Wonneberger et al.[49]. At the phase transition (T=20.4 K) all the elastic constants show a sharp discontinuity which indicates and confirms that the transition is indeed first order. The present elastic constants are also shown to be in excellent agreement with previous ultrasonic and neutron scattering data. The temperature variation of the Pockel's coefficients, and coefficient ratios, show no significant anomalies across the phase transition. This is not surprising since the rotational ordering does not induce any large density fluctuations and hence any drastic changes in Rayleigh or Brillouin intensities and again emphasizes the first order nature of the transition.

Theoretical calculations[49] have shown a strong correlation between rotational and translational modes in CH_4-I. The decrease in C_{12} supports these predictions. At the phase transition, the softening of the acoustic phonons in the <110> direction has been attributed to the decreased rotational motion which significantly decreases the RT coupling interaction. The rotational motion is coupled more strongly to the transverse phonons as indicated by the anomaly in the shear modulus, while the bulk modulus showed no significant change at the phase transition. The decrease in RT coupling was also inferred through a comparison with the rare gas solids. Comparisons with low temperature argon have shown that in CH_4-II the intermolecular potential has

become more central in nature, losing most of its orientational dependence. Both the deuterated and undeuterated species exhibit very similar elastic properties in Phase I.

Further experiments are under way to confirm some of the low temperature data of this investigation. Other experiments in this laboratory will involve determining the acoustic anomalies in CD_4 and to compare any RT coupling effects with those of this investigat'on. An effort will also be made to study the CH_2D_2 in order to draw comparisons between the symmetric and asymmetric species as related to RT coupling.

Bibliography

[1] C. N. N. Rao, K. J. Rao, *Phase Transitions in Solids* (McGraw-Hill, 1978).

[2] K. Clusius, Z. Phys. Chem. Teil B3, 41 (1929).

[3] L. D. Landau and E. M. Lifschitz, *Statistical Physics* 3rd ed. Part I, (Pergamon Press, Oxford 1980)

[4] *Structural Phase Transitions I*, K. A. Müller and H. Thomas Ed., (Springer-Verlag, New York 1981)

[5] C. W. Garland: In *Physical Acoustics Vol II*, W. P. Watson and R. N. Thurston ed. (Academic, New York 1970).

[6] C. W. Garland and J. D. Baloga, Phys. Rev. **B13**, 2145 (1976).

[7] W. Rehwald, Solid State Communications **8**, 607, 1483 (1970).

[8] R. O. Bell and C. Rupprecht, Phys. Rev. **129**, 90 (1963).

[9] K. Fossheim and B. Berre, Phys. Rev. **B5**,3292 (1972).

[10] B. Lüthi and T. J. Morgan, Phys. Rev. **B2**, 1211 (1970).

[11] S. Kashida, I. Hatta, A. Ikushima and Y. Yamada, J. Phys. Soc. Jpn. **34**, 997 (1973).

[12] B. P. Stoicheff, in *Rare Gas Solids Vol II*, M. L. Klein and J. A. Venables Ed. (Academic, London 1976).

[13] J. De Boer, Physica **14**, 139 (1948).

[14] J. H. Colwell, E. K. Gill and J. A. Morrison, J. Chem. Phys. **36**, 2223 (1962).

[15] J. H. Colwell, E. K. Gill and J. A. Morrison, J. Chem. Phys. **39**, 635 (19630.

[16] J. H. Colwell, E. K. Gill and J. A. Morrison, J. Chem. Phys. **42**, 3144 (1965).

[17] H. M. James and T. A. Keenan, J. Chem. Phys. **31**, 12 (1959).

[18] W. Press, J. Chem. Phys. 56, 2597 (1972).

[19] E. Arzi and E. Sandor, Acta Crystallogr. **A31**, **S3**, 188 (1975).

[20] D. N. Bol'shutkin, D. N. Gasan, V. M. Prokhvatilov, and A. I. Erenburg, J. Struct. Chem. 12, 313 (1971).

[21] D. R. Baer, B. A. Fraass, D. H. Riehl and R. O. Simmons, J. Chem. Phys. **68**, 1411 (1978).

[22] T. Yamamoto, Y. Kataoka and K. Okada, J. Chem. Phys. **66**, 2701 (1977).

[23] A. I. Prokhvatilov and A. P. Isakina, Sov. J. Low Temp. Phys. **9**, 213 (1983).

[24] G. E. Ewing, J. Chem. Phys. **40**, 179,(1964).

[25] G. B. Savitsky and D. F. Hornig, J. Chem. Phys. **36**, 2634 (1962).

[26] R. Savoie and R. P. Fournier, Chem. Phys. Lett. **7**, 1 (1970).

[27] A. Anderson and R. Savoie, J. Chem. Phys. **31**, 12 (1959).

[28] J. Obriot, F. Fondère, Ph. Marteau, H. Vu and K. Kobashi, Chem. Phys. Lett. **60**, 90 (1978).

[29] G. Baciocco, P. Calvani and S. Cunsolo, J. Chem. Phys. **87**, 1913 (1987).

[30] M. S. Costantino and W. B. Daniels, J. Chem. Phys. **62**, 764 (1975).

[31] W. Press and A. Kollmar, Solid State Commun. **17**, 405 (1975).

[32] E. A. Ballik, D. J. Gannon and J. A. Morrison, J. Chem. Phys. **57**, 1793 (1972).

[33] A. J. Nijman and N. J. Trappeniers, Chem. Phys. Lett. **47**, 188 (1977).

[34] F. Lostak, K. O. Prins and N. J. Trappeniers, Physica **B162**, 254 (1990).

[35] M. Sprik, T. Hijmans and N. J. Trappeniers, Physica **B112**, 285 (1982).

[36] K. P. Wong, J. D. Noble, M. Bloom and S. Alexander, J. Magn. Reson. **1**, 55 (1969)

[37] R. F. Code and J. Higinbotham, Can. J. Phys. **54**, 1248 (1976).

[38] A. J. Nijman and A. J. Berlinsky, Phys. Rev. Lett. **38**, 408 (1977).

[39] M. J. P. Musgrave, *Crystal Acoustics*, (Holden-Day, San Francisco 1970).

[40] J. F. Nye, *Physical Properties of Crystals* (Clarendon, Oxford 1957).

[41] L. D. Landau and E. M. Lifshitz, *Theory of Elasticity* 2nd ed., (Pergamon Press, Oxford 1970).

[42] C. Kittel, *Introduction to Solid State Physics* 3rd ed., (John Wiley & Sons, New York 1966)

[43] L. Brillouin, Ann. Phys. **17**, 88 (1922).

[44] M. Born and K. Huang, *Dynamical Theory of Crysta Lattices* (Clarendon Press, Oxford 1954).

[45] I. L. Fabelinskii, *Molecular Scattering Of Light* (Plenum Press, Ney York 1968).

[46] D. F. Nelson, P. D. Lazay and M. Lax, Phys. Rev **B6**, 3109 (1972).

[47] G. B. benedek and K. Fritsch, Phys. Rev. **149**, 647 (1966).

[48] T. S. Narasimhamurty, *Photoelastic and Electro-Optic Properties of Crystals*, (Plenum Press, New York 1981).

[49] S. Wonneberger and A. Huller, Z. Phys. **B66**, 191 (1987).

[50] S. W. Lovesey, *Condensed Matter Physics: Dynamic Correlations 2nd ed* (Benjamin Cummings Publishing Co. Inc. 1986).

[51] R. Kubo, J. Phys. Sos. Japan **12**, 570 (1966).

[72] S. F. Ahmad, Ph. D. Thesis, Memorial University of Newfoundland, St. John's Newfoundland 1980 (Unpublished).

[53] V. Askarpour, Ph. D. Thesis, Memorial University of Newfoundland, St. John's Newfoundland 1991 (Unpublished).

[54] M. Born and E. Wolf, *Principles of Optics* (Pergamon Press, New York 1964).

[55] P. Jacquinot, Rep. Prog. Phys. **23**, 267 (1960).

[56] J. R. Sandercock, *Proc. 2nd. Int. Conf. on Light Scattering in Solids*, M. Balkanski ed. (Paris 1971) p. 9.

[57] V. Mazzacurati, G. Signorelli and G. Ruocco, Europhys. Lett. **2**, 877 (1986).

[58] S. F. Ahmad, H. Kiefte, M. J. Clouter, and M. D. Whitmore, Phys. Rev. **B26**, 4239 (1982).

[59] J. C. Brice, *The Growth of Crystals From the Melt* (North-Holland, Amsterdam 1965).

[60] B. D. Cullity, *Elements of X-ray Diffraction* (Addison-Wesley, Ma. 1967).

[61] P. H. Gammon, M. Sc. Thesis, Memorial University of newfoundland, St. John's Newfoundland 1978 (Unpublished).

[62] H. Goldstein, *Classical Mechanics* (Addison-Wesley, Cambridge 1950).

[63] S. C. Rand and B. P. Stoicheff, Can. J. Phys. **60**, 287 (1982).

[64] D. G. Bounds, M. L. Klein and G. N. Patey, J. Phys. Chem. **72**, 5348 (1980).

[65] K. H. Michel and J. Naudts, Phys. Rev. Lett. **39**, 212 (1977).

[66] K. H. Michel and J. Naudts, J. Chem. Phys. **67**, 547 (1977).

[67] K. H. Michel and J. Naudts, J. Chem. Phys. **68**, 216 (1978).

[68] G. Briganti, P. Calvani, F. De Luca and B. Maraviglia, Can. J. Phys. **56**, 1182 (1978).

[69] W. G. Stirling, W. Press and H. Stiller, J. Phys. **C10**, 39599 (1977).

[70] R. A. Fisher and R. O. Watts, Mol. Phys. **23**, 1051 (1972).

[71] M. L. Klein, G. K. Horton and V. V. Goldman, Phys. Rev. **B2**, 4995 (1970).

[72] C. Feldman, M.L. Klein and G. K. Horton, Phys. Rev. **184**, 910 (1969).

[73] J. Tolédano and P. Tolédano, *The Landau Theory Of Phase Transitions* (World Scientific 1987).

[74] P. D. Lazay, J. H. Lunacek, N. A. Clarke and G. B. Benedek, in *Light Scattering Spectra of Solids*, G. B. Wright ed. (Springer-Verlag, New York 1969).

[75] W. Press, B. Dorner and G. Will, Phys. Lett. **31A**, 253 (1970).

[76] W. Press, Acta Cryst. **A29**, 257 (1973).

[77] D. Fabre, M. Thiéry, H. Vu and K. Kobashi, J. Chem. Phys. **71**, 3081 (1979).

[78] A. Cabana and N.D. Thé, Can. J. Chem. **55**, 3862 (1977).accent on e in The.

[79] D. C. Heiberlein and E. D. Adams, J. Low Temp. Phys **3**, 115 (1970).

[80] R. J. Stevenson, J. Chem. Phys. **27**, 656 (1957).

[81] J. W. Stewart, J. Phys. Chem. Solids **12**, 122 (1959).

[82] S. V. Marx and R. O. Simmons, J. Chem. Phys. **81**, 944 (1984).

[83] P. H. Gammon, H. Kiefte and M. J. Clouter, J. Chem. Phys. **70**, 810 (1979).

[84] N. Rich, M.J. Clouter, H. Kiefte and S.F. Ahmad, Bull. Amer. Phys. Soc. **27**, 633 (1982).

[85] H. Glätti, A. Sentz and M. Eisenkremer, Phys. Rev. Lett. **28**, 871 (1972).

[86] C. Chapados and A. Cabana, Can. J. Chem. **50**, 3521 (1972).

[87] M. A. White and J. A. Morrison, J. Chem. Phys. **72**, 5927 (1980).

[88] A. I. Prokhvatilov and A. P Isakina, Sov. J. Low Temp. Phys. **16**, 91 (1984).

[89] M. Bloom and J. A. Morrison, in *Surface and Defect Properties Of Solids, Vol II*, (Chem. Soc., London (1973).

[90] E. A. Ballik, D. J. Gannon and J. A. Morrison, J. Chem. Phys. **58**, 5639 (1973).

[91] M. A. White and J. A. Morrison,J. Chem. Phys. **70**, 5384 (1979).

[92] N. P. Wong, J. D. Noble, M. Bloom and J. Alexander, Mag. Reson. **1**, 55 (1969).

[93] F. D. Medina and W. B. daniels, J. Chem. Phys. **70**, 2688 (1979).

[94] F. D. Medina, J. Chem. Phys. **73**, 77 (1980).

[95] C. Chapados and A. cabana, Chem. Phys. Lett. **16**, 191 (1970).

[96] B. W. Baran and F. D. Medina, Chem. Phys. Lett. **176**, 509 (1991).

[97] A. I. Prokhvatilov, A. P. Isakina and I. N. Krupskii, Solid State Commun. **42**, 59 (1982).

[98] W. G. Stirling, W. Press and H. H. Stiller, J. Phys. C: Solid State Phys. **10**, 3959 (1977).

[99] A. Hüller, Phys. Rev. **B10**, 4403 (1974).

[100] K. H. Michel and D. M. Kroll, J. Chem. Phys. **64**, 1300 (1976).

[101] G. A. De Witt and M. Bloom, Can. J. Phys. **47**, 1195 (1969).

[102] J. E. Piott and W. D. McCormick, Can. J. Phys. **54**, 1784 (1976); **54**, 1799 (1976).

[103] H. Glättli, P. Calvani and B. Bouchet, J. Chem. Phys. **85**, 671 (1986).

[104] A. G. McLellan, J. Phys. **C9**, 939 (1976).

[105] R. P. Wolf and F. A. Stahl, in *Low Temperature Physics* LT 13, K. D. Timmerhaus, W. J. O'Sullivan and E. F. Hammel ed. (Plenum, New York 1974).

[106] V. G. Manjhelii, A. M. Tolkachev and V. G. Gavrilko, J. Phys. Chem. Solids **30**, 2759 (1969).

[107] W. Press, A. Hüller, H. Stiller, W. Stirling and R. Currat, Phys. Rev. Lett. **32**, 1354 (1974).

[108] R. A. McLaren, Ph. D. Thesis, University of Toronto, Toronto Ontario 1974 (Unpublished).

[109] H. Kiefte and M. J. Clouter, J. Chem. Phys. **62**, 4870 (1975).

[110] H. Kiefte, R. Penney and M. J. Clouter, J. Chem. Phys. **88**, 5846 (1988).

[111] H. E. Stanley, *Phase Transitions and Critical Phenomena*, (Clarendon Press, Oxford 1971).

[112] W. Yelon, in *Proceedings of the NATO Advanced Study Institute on Anharmonic Lattices, Structural Phase Transitions and Melting*, Geilo, Norway, 1973, T. Riste ed. (Noordhoof, Leiden 1974).

[113] A. I. Prokhvatilov and A. P. Isakina, Acta Cryst. **B36**, 1576 (1980).

[114] L. A. Schwalbe and R. N. Wilkins, J. Chem. Phys. **72**, 3130 (1980).

[115] A. Heidemann, W. Press, K. J. Lushington and J. A. Morrison, J. Chem. Phys. **75**, 4003 (1981).

[116] A. Hüller, Phys. Rev. **B16**, 1844 (1977).

[117] M. Sprik and N. J. Trappeniers, Physica **A103**, 411 (1980).

[118] J. Herczeg and R. E. Stoner, J. Chem. Phys. **54**, 2284 (1971).

[119] A. Hüller and W. Press, Phys. Rev. Lett. **29**, 266 (1972).

[120] W. Press and A. Hüller, Phys. Rev. Lett **30**, 1207 (1973).

[121] R. J. Meyer, Phys. Rev. **B14**, 4094 (1976).

[122] A. J. Nijman and A. J. Berlinsky, Can. J. Phys. **58**, 1049 (1980).

[123] R. P. Wolf, F. A. Stahl and J. A. Watrous, J. Chem. Phys. **59**, 115 (1973).

[124] V. V. Goldman, G. K. Horton and M. L. Klein, Phys. Rev. **B4**, 567 (1971).

[125] N. G. Parsonage and L. A. K. Staveley, *Disorder in Crystals*, (Clarendon Press, Oxford 1978).

[126] W. Press, *Single Particle Rotations in Molecular Crystals*, (Springer-Verlag, New York 1981).

[127] W. Press, B. Dorner and H. Stiller, Solid State Commun. **9**, 1113 (1971).

[128] P. A. Bezuglyi, N. G. Burma and R. Kh. Minyafaev, Sov. Phys. Solid State **8**, 596 (1966).

[129] L. M. Tarasenko, Sov. J. Low Temp. Phys. **1**, 688 (1975).

[130] R. P. Wolf, F. A. Stahl and J. J. Folkins, J. Phys. Chem. Solids **39**, 719 (1978).

[131] R. W. Hill, Proc. Phys. Soc. (London) **A65**, 349 (1952).

[132] *Rare Gas Solids Vol II*, M. L. Klein and J. A. Venables Ed. (Academic, London 1976).

[133] M. L. Klein, G. K. Horton and V. V. Goldman, Phys. Rev. **B2**, 4995 (1970).

[134] C. Feldman, M. L. Klein andG. K. Horton, Phys. Rev. **184**,910 (1969).

[135] Y. Fujii, N. A. Lurie, R. Pynn and G. Shirane, Phys. Rev. **B10**, 3647 (1974).